

THE HENRYK NIEWODNICZAŃSKI
INSTITUTE OF NUCLEAR PHYSICS
POLISH ACADEMY OF SCIENCES
UL. RADZIKOWSKIEGO, 31-342 KRAKÓW, POLAND
WWW.IFJ.EDU.PL/PUBL/REPORTS/2008/
KRAKÓW, DECEMBER 2008

REPORT No. 2019/PL

Experimental search for superheavy elements

Andrzej Wieloch*

Habilitation thesis

(prepared in March 2008)

*M. Smoluchowski Institute of Physics, Jagiellonian University, Reymonta 4,
30-059 Kraków. e-mail: ufwieloc@cyf-kr.edu.pl

Abstract

This work reports on the experimental search for superheavy elements (SHE). Two types of approaches for SHE production are studied i.e.: “cold” fusion mechanism and massive transfer mechanism. First mechanism was studied, in normal and inverse kinematics, by using Wien filter at the GANIL facility. The production of elements with $Z=106$ and 108 is reported while negative result on the synthesis of SHE elements with $Z=114$ and 118 was received. The other approach i.e. reactions induced by heavy ion projectiles (e.g.: ^{172}Yb , ^{197}Au) on fissile target nuclei (e.g.: ^{238}U , ^{232}Th) at near Coulomb barrier incident energies was studied by using superconducting solenoid installed in Texas A&M University. Preliminary results for the reaction $^{197}\text{Au}(7.5\text{MeV}/u) + ^{232}\text{Th}$ are presented where three cases of the possible candidates for SHE elements were found. A dedicated detection setup for such studies is discussed and the detailed data analysis is presented. Detection of alpha and spontaneous fission radioactive decays is used to unambiguously identify the atomic number of SHE. Special statistical analysis for a very low detected number of α decays is applied to check consistency of the α radioactive chains.

Contents

1. Introduction	7
2. Overview of the past and present status of SHE ...	11
2.1. Stability of superheavy nuclei - role of nuclear shells	13
2.2. Reaction of synthesis	14
2.2.1. Cold fusion of massive nuclei	15
2.2.2. Experimental approach and detection setup	19
3. Superheavy elements production at GANIL	23
3.1. GANIL experimental setup	23
3.1.1. Reaction chamber	23
3.1.2. Wien filter	24
3.1.3. Detection setup	25
3.1.4. Data acquisition system	26
3.1.5. Fast analysis software for on-line SHE identification	27
3.2. Experimental results	30
3.2.1. Energy calibration of the implantation detector	30
3.2.2. Analysis of the reaction $^{54}\text{Cr} + ^{165}\text{Ho}$, 4.698 MeV/u	34
3.2.3. Analysis of the reaction $^{54}\text{Cr} + ^{\text{nat}}\text{Gd}$, 4.698 MeV/u	38
3.2.4. Seaborgium, element Z=106. Analysis of the reaction $^{54}\text{Cr} + ^{208}\text{Pb}$	39
3.2.4.1. Beam energy 4.698 MeV/u	40
3.2.4.2. Beam energy 4.750 MeV/u.	40
3.2.5. Search for element Z=118	41
3.2.6. Synthesis of hassium (Z=108) isotopes	42
3.2.7. Search for element Z=114	47
3.2.7.1. Transmission efficiency of the Wien filter	47
3.2.7.2. Cross section of pico barn region	48
3.2.7.3. Results	48
3.2.8. Inverse kinematics experiments	48
3.3. Gas-scintillation detector for SHE studies	51
3.4. Summary and future of the FULIS collaboration experiments	53
4. Radioactive decays, low statistics case	55
4.1. Calculation of statistical errors for measured half-life times	55
4.2. Consistency of α -radioactive decays	58
4.2.1. Test procedure	60

5. Superheavy elements studies at TAMU	65
5.1. Fusion of projectile with target fission fragment - a new path to SHE production	65
5.2. Experimental test of the method	67
5.3. 2006 experiment - most recent results	70
5.3.1. Detection setup	70
5.4. Detectors calibration	73
5.4.1. Energy loss and time of flight calibration of the experimental setup	73
5.4.2. Flash ADC pulse shape analysis. Direct <i>Au</i> beam at 7.5 <i>A.MeV</i>	76
5.4.3. Pileup rejection - electronic unit and FADC pulse shape analysis	78
5.4.4. Position sensitive detectors	81
5.5. Search for superheavies in the <i>Au + Th</i> reaction	85
5.6. Further analysis and future of the Texas A&M experiments	91
6. Summary and discussion	93
6.1. Acknowledgements	94
A. Appendix	101

1. Introduction

The heaviest known natural element is Uranium (U) with the number of protons $Z=92$ ¹. All elements above U have been produced artificially in heavy ion laboratories across the world and are more or less unstable. The history of the formation of heavy artificial elements begins in the 40s of the last century. In 1934 Enrico Fermi proposed a method to produce such elements. By bombarding a nucleus (Z, N), where N denotes neutron number, with neutrons one obtains a new isotope ($Z, N+1$) which can β^- decay thus forming a new element ($Z+1, N$). The first elements created in a laboratory were neptunium ($Np, Z=93$) and plutonium ($Pu, Z=94$). They were produced at the University of California in Berkeley in 1940-41. Neptunium was fabricated by McMillan et al. [1] bombarding U nuclei with neutrons. Seaborg et al. [2] discovered plutonium-238 (^{238}U) through the β^- decay of neptunium-238 (^{238}Np) which in turn were produced by bombarding uranium with deuterons². Elements $Z=99$ and 100 were first identified in the debris of the hydrogen bomb test in 1952 (the process reconstructed was the many neutron capture by uranium which then decayed quickly by beta emission to more stable isotopes of elements einsteinium and fermium). To synthesize elements $Z=95, 96, 97, 98$ and 101 it was sufficient to irradiate previously produced heavy nuclei ($Z=93, 94, 99$) with neutrons or alpha particles (see tab. A.1). In the late-50s newly constructed accelerators were capable to accelerate heavier nuclei than helium atoms. These new accelerators opened the door for the creation of even heavier elements known as superheavy elements (SHE).

Along with the growing number of protons in nucleus, Coulomb repulsion forces cause the decreasing of the fission barrier. When this number becomes large enough, $Z \simeq 114$, the barrier should completely vanish, and an instantaneous break up of a nucleus appears. However, Myers and Świątecki [3] showed in 1966 that closed shells created by quantum effects ensure the existence of the barrier even for nuclei with $Z > 114$. Further theoretical elaborations, based on the shell model, predicted more precisely that the next closed shells should emerge for spherical nuclei at $Z=114$ and $N=184$. Such nuclei would be located in the center of the island of stability of superheavy elements. Their half-life times, with respect to the spontaneous fission were estimated from a few years to many thousands of years. The calculations also revealed, that alpha radioactivity is the main decay mode of those nuclei [4] and one should expect an increase of their half-life times for this mode of decay. Experiments targeted on reaching this hypothetical island of stability were initiated.

Production of the superheavy elements, $Z > 104$, was accomplished by complete fusion reactions in nuclear collisions by laboratories operating heavy ion accelerators: Joint Institute for Nuclear Research (JINR), Gesellschaft für Schwerionenforschung (GSI) and Lawrence Berkeley National Laboratory (LBNL). Such studies were pos-

¹ One can find also in natural uranium ores trace quantities of Neptunium ($Z=93$) and Plutonium ($Z=94$).

² For the discovery of Np and Pu elements Edwin McMillan and Glen Seaborg were awarded Nobel Prize in chemistry in 1951.

1. Introduction

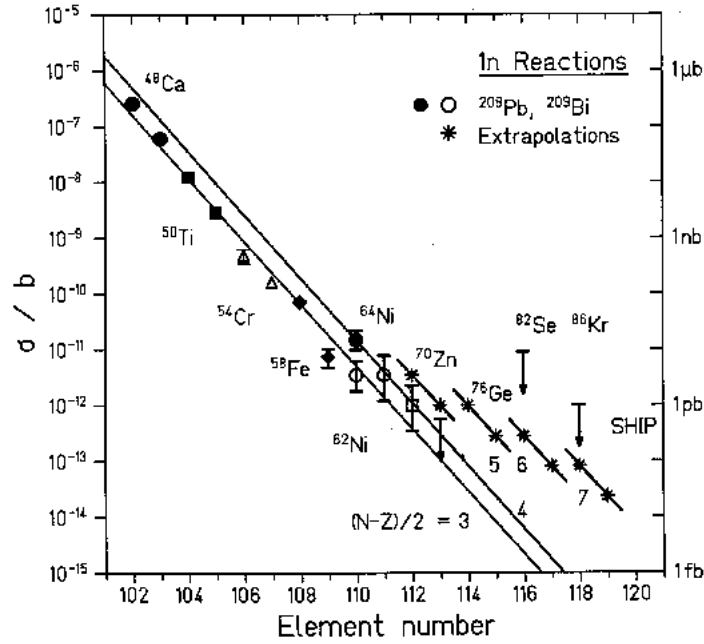


Figure 1.1.: Cross section data and extrapolated values for “cold” fusion reactions (1n-evaporation channel) [5].

sible because of the impressive progress made in accelerator technology, and new, highly efficient heavy ion sources. Until the year 1988, elements with Z up to 112 were discovered in this way [6, 7, 8, 9]. Unfortunately, during those studies it turned out that the cross section for superheavy nuclei production in fusion reactions is decreasing quite rapidly: with every next Z more or less by factor 4 (see fig. 1.1), reaching for element with $Z=112$ about 1 pb . This was a very serious limitation in the synthesis of the next elements. Moreover, half-life times of the most heaviest ones were becoming as short as a few tens of μs . Such small values of half-lives has shaken the belief in the existence of the island of stability for SHE. One of possible explanations for these results was that the newly produced elements were highly neutron deficient isotopes, and they should in fact live quite short. Simply, available combinations of projectiles and targets could not be used to produce more neutron rich nuclei. At present, the periodic table contains elements with the atomic number (Z) up to 118.

The most recent discoveries (1998-2005) made by the Dubna-Livermore collaboration, a synthesis of elements $Z=114$ in reaction $^{48}\text{Ca}+^{242,244}\text{Pu}$, $Z=116$ (year 2000) in reaction $^{48}\text{Ca}+^{248}\text{Cm}$ [10], and $Z=118$ (year 2002) in reaction $^{48}\text{Ca}+^{249}\text{Cf}$ [11, 12, 13], which still need to be confirmed by other laboratories, delivered a new impulse to search for the next heavy elements, and to synthesize new isotopes of already known elements. In the case of above reactions the half-life times of produced nuclei, e.g. for $Z=114$ is a few seconds, indicate the increase of their stability. This brings new hope for the existence the island of stability in the region predicted by the theory: $Z=114$, $N=184$.

In fact all artificial elements beyond fermium were created by complete fusion of

heavy ions. Two types of approaches have been used in this case: the “cold” fusion with bismuth or lead targets and projectiles of most neutron rich isotopes like ^{64}Ni or ^{70}Zn to produce elements 110 and 112 and “hot” fusion of actinide targets such as Pu , Cm or Cf with ^{48}Ca projectiles to reach elements with $Z=114, 116, 118^3$ [14].

In the case of “cold” fusion reactions, the created superheavy nuclei possess low excitation energy $E^* = 10 - 15 \text{ MeV}$ while for “hot” reactions excitation energy is $E^* = 30 - 40 \text{ MeV}$. In both cases only some of them can survive as a residue and reach their ground state or isometric states by 1-2, or 3-4 neutrons emission depending if the reaction studied is “cold” or “hot”. Most disintegrate immediately because the fission barrier is nearly equal, or even lower than the neutron binding energy. As a result, cross section for residue creation is a product of a cross section for fusion reaction and probability, that in a cooling phase, fission will not occur.

Besides trying to reach the island of stability, studies of superheavy elements production is important for testing theories, ones that describe reaction dynamics in the entrance channel (e.g. [15], [16]), and others that deal with a structure and decay modes of the SHEs (e.g. [17]). In the first case, the more accurate dynamical theory could propose an optimal energy and projectile-target combination for a synthesis experiment. In the second case, the exploration of decay modes allows to obtain better knowledge of shell model parameters and from that a structure of such heavy nuclei.

In this thesis I concentrate mainly on the experimental aspects of searching and the production of superheavy elements. The description of SHE experiments is set forth and the results are presented. The search for SHE was performed by the Krakow group in collaboration with two leading heavy ion laboratories, i.e. Grand Accélérateur National d’Ions Lourds (GANIL) in France and the Cyclotron Institute of Texas A&M University (TAMU) in USA.

The thesis is divided into six parts. Part no. 3 describes SHE campaigns at GANIL from the period 1999-2003 while part no. 5 is devoted to the experiments performed at TAMU cyclotron between 2003-2006. For each collaboration a short summary is made and in the last part of the thesis a common summary and perspectives for SHE production is presented. A separate part of the work, part no. 4, was devoted to the statistical analysis that can be used to test reliability of the data collected in the SHE experiments. The following part (no. 2) presents an overview of the present knowledge in the field of superheavy elements investigation.

³The “cold” and “hot” fusion reactions are wider discussed in the section 2.2 ”Reaction of synthesis”.

1. Introduction

2. Overview of the past and present status of SHE and Island of Stability quest

Heavy element research explores the borderline of the upper part of the nuclides chart where the repulsive Coulomb forces between the many protons start to dominate the nuclear stability and in some place of the chart of nuclides terminate the number of elements due to instability against fission.

However during the past 50 years, many theoretical approaches suggested that the microscopic stabilization through shell effect will still ensure the existence of heavy stabilized nuclei. These superheavy elements are predicted for the next doubly closed shell above lead at $Z=114$, $N=184$ according to one calculations and $Z=120$ or 124 , $N=184$ for other predictions. In fact the first evidence for increased stability was the discovery of the elements seaborgium and hassium [18, 19] which are a part of the microscopic stabilized region of deformed nuclei centered at $Z=108$, $N=162$. Further proofs of an enhanced stability in the region of superheavy nuclei have been validated also by the results of recent experiments of Dubna group. Decay energies and life times of ≈ 30 new nuclides with $Z=104-118$ and $N=162-176$ that have been synthesized in the complete fusion reactions of ^{238}U , $^{242,244}\text{Pu}$, ^{243}Am , $^{245,248}\text{Cm}$, and ^{249}Cf targets with ^{48}Ca beams indicate a considerable increase of the stability of superheavy nuclei with an increasing number of neutrons.

After Hahn and Strassman had discovered the induced fission of uranium, the liquid drop model of the fissioning nucleus was proposed by Bohr and Wheeler [20] to describe this phenomena. This essentially, classical theory assumes that nuclear matter is a macroscopically structureless body, similar to a drop of charged liquid. The deformation of the drop is induced by the Coulomb forces, which finally lead to its fission into two parts (fragments) of \approx equal masses when the potential barrier is overcome by the fragments. For the nucleus ^{238}U the fission barrier amounts to approximately $B_f \sim 6 \text{ MeV}$. According to this model the height of the fission barrier decreases rapidly with increasing the element number (Z) and at a definite critical atomic number the nucleus becomes unstable against the spontaneous fission (SF) which undergoes typically after the time $T_{SF} \sim 10^{-19} \text{ s}$ where T_{SF} denotes mean life time of the SHE element with respect to the SF process. This critical situation should be reached already for values of $Z=104-106$. Subsequent discoveries of the first transuranium elements, which were mainly synthesized with high-flux neutron reactors, qualitatively confirmed the analogy between the liquid drop and nuclear matter e.g. the probability of spontaneous fission for nuclei from ^{238}U ($Z=92$) to ^{257}Fm ($Z=100$) increased by more than a factor of 10^{13} .

Situation has changed when the discovery of spontaneously-fissioning isomers was announced. The shape isomerism in several tens, at that time already known, nuclei - isotopes of U to Bk , was in contradiction to the liquid drop model of fission.

2. Overview of the past and present status of SHE ...

Now, it is well established that the existence of isomers is a result of the complex structure of the potential energy surface of the nucleus, in particular, a result of the two-humped shape of the fission barrier (see review of Bjornholm and Lynn [21]). Another contradiction with the liquid drop model was found in the significant variations of the partial life times of spontaneous fission, best pronounced for the isotopes of *Cf*, *Fm* and the transfermium elements, which have been synthesized in heavy-ion induced reactions [22].

Actually, the classical liquid drop model describes only the mean changes in the binding energies of the nucleus with the growth of its mass. For the nucleus, as a quantum object composed of few to several hundreds of nucleons, a strong local variations of the energy levels occupied by the different nucleons can emerge. These states are far from homogeneous. The individual neutrons and protons can populate energy levels located in such a way that unequal gaps appear in the discrete energy spectrum. Such localized concentrations of the energy levels below the gaps cause a noticeable increase in the total binding energy, and therefore, in the stability of a nucleus. The number of protons and neutrons in nuclei with maximum binding energy are called closed proton and neutron shells - by analogy with atomic physics. Most strongly the effect of nuclear shells is manifested in the "doubly magic" nuclei, such as ^{208}Pb ($Z=82$, $N=126$), for which the value of the shell correction $E_{shell} = 14$ MeV. In mass formula, the shell effect has usually been accounted for by means of corrections. In the works of Świątecki and Myers a phenomenological description was given for the shell anomalies in the nuclear masses [3].

In 1966, Strutinsky suggested an original method for calculating the shell corrections to the liquid drop nuclear energy [23, 24]. In this approach, the shell correction is determined as the difference between the sum of the single particle energies in the case of a real quantum nucleon distribution and some "homogeneous" distribution of levels in the mean nuclear potential, which characterizes the liquid drop. The total energy of the nucleus can be presented by the sum: $E_{tot} = E_{ld} + E_{shell}$, i.e. the sum of the macroscopic (liquid drop) energy E_{ld} , and the microscopic part E_{shell} , which is connected with the nuclear shell structure and the pairing correlations of the nucleons. The calculations of this macro-microscopic model have revealed regularities in the shells of deformed nuclei. This led to higher precision in defining their mass and shape in the ground state. Contrary to the common opinion that shell effects are smeared out with the increase of the deformation of the nucleus, it was observed that in highly deformed nuclei a substantial re-distribution of the nucleons takes place. With the increase of deformation shell effects do not vanish, but simply change, still bringing on to a significant correction to the potential energy of the nucleus [25]. Thus the calculations performed within the macro-microscopic theory explained quite a large number of experimental findings: the shape isomerism of actinide nuclei, the constant height of their fission barriers, the abrupt changes in the fission probability for nuclei with a neutron number close to $N = 152$ and other observables, which had no interpretation in the framework of the classical liquid drop model.

2.1. Stability of superheavy nuclei - role of nuclear shells

Similarly to any other theory, the macro-microscopic model had a definite predictive power, what concerned, in particular, the masses and radioactive properties of very heavy, hitherto unknown nuclei. Such predictions were made in a series of works. One can mention here the results obtained by Patyk, Smolańczuk and Sobiczewski [26], [27], who calculated masses and fission barriers of even-even nuclei with $Z=104-120$ and $N=140-190$. For the nucleus $^{254}102$, the liquid drop fission barrier amounts to about $B_{f,ld} \sim 1 \text{ MeV}$, while for the heavier nucleus $^{270}108$ it is practically equal to zero. At the same time, the amplitude of the shell correction for these nuclei amounts to about 5 and 7 MeV , respectively.

In calculations of the nuclear potential energy, when the shell correction is taken into account, a fission barrier is revealed and its height is about 6-8 MeV . The occurrence of a fission barrier, when the heavy nucleus is deformed, should cause significant hindrance to spontaneous fission. Indeed, according to refs. [26], [27], the partial half-lives for spontaneous fission depend strongly on the amplitude of the shell correction. The significant rise in $T_{SF}(N)$ when moving away from the $N=152$ shell, which manifests itself noticeably in the radioactive properties of the actinide nuclei, is due to the influence of another neutron shell at $N=162$. What is important, these two shells are related to deformed nuclei contrary to the case of the doubly magic nuclei such as ^{208}Pb , which are spherical in their ground state. The maximum stability with respect to spontaneous fission is expected for the nucleus $^{270}108$ ($N=162$) for which the predicted T_{SF} value can amount to several hours. Further increase of the neutron number results in the decrease of the ground-state deformation of the nucleus due to the moving away from the deformed shell $N=162$. At $N>170$ a significant rise of T_{SF} is expected for nuclei up to $^{292}108$ ($N=184$), whose partial half-life with respect to spontaneous fission can be as long as $T_{SF} \sim 3 \cdot 10^4$ years.

At this point we come to an interesting situation. If superheavy nuclei possess high stability with respect to spontaneous fission, the other modes of decay become possible: α -decay and, eventually, β -decay. The probability for these modes of decay, hence the life times, will be determined by the nuclear masses in the ground state. The latter can be calculated by different models, which are based on different assumptions of the fundamental properties of nuclear matter. Hence, any experimental result becomes extremely informative as far as the verification of the theoretical models is concerned. Following the calculations, performed within the macroscopic-microscopic model, the deformed nucleus $^{268}106$ ($N=162$) should undergo α -decay with a half-life of $T_{1/2} \sim 2 \text{ h}$ (according to a different calculation by Möller et al. [28] - a few days). For the heavier, more spherical nucleus $^{294}110$ ($N=184$), $T_{1/2}$ increases to several hundred, or even thousand, years. Let us note that in the absence of a nuclear structure, as it is in the classical liquid drop model case, this nucleus should fission spontaneously with $T_{SF} \sim 10^{-19} \text{ s}$. The difference in half-life time is about 30 orders of magnitude! Calculations of the energy of the nucleus as a many-body system, carried out in the Hartree-Fock-Bogoliubov (HFB) model, as well as calculations in the relativistic mean field model also indicate a significant increase in the binding energy of the nucleus when approaching the closed neutron shell $N=184$. For a spherical doubly magic nucleus a maximum value of the binding

2. Overview of the past and present status of SHE ...

energy is expected. However, the theoreticians have not yet come to a consensus what concerns the magic proton number, while the closed neutron shell is claimed to be $N=184$. For instance, in the macro-microscopic model, independent of the variations in the parameters used in the calculations, the amplitude of the shell correction reaches maximum for the nucleus $^{298}114$ ($N=184$) [4]. On the contrary, in the HFB calculations together with $Z=114$ there are other possible candidates: $Z=120, 122, 126$ and even 138 , depending on the chosen set of parameters [29]. For even larger atomic numbers theory predicts very exotic configurations of nuclei that have gross non-uniformities of nuclear matter density [17]. The main conclusion, however, is the following: in the region of very heavy nuclei there may exist an “island of enhanced stability”, consisting of many β -stable neutron-rich isotopes of superheavy elements.

2.2. Reaction of synthesis

It is well known that the first artificial elements heavier than uranium were synthesized in reactions of sequential capture of neutrons ((n, γ) -type) during long exposures at high-flux neutron reactors. The long life time of the new nuclides made possible their separation by radiochemical methods followed by the measurement of their radioactive decay properties. This pioneering work, which was performed by Seaborg and colleagues in the period of 1940-1952, led to the synthesis of 8 artificial elements with $Z=93-100$, for references see tab. A.1. The heaviest nucleus was ^{257}Fm ($T_{1/2} \sim 100 d$). The further progress in study of the region of heavier nuclei was blocked by the extremely short life time of ^{258}Fm ($T_{SF} \sim 0.3 ms$). Transfermium elements with mass $A > 257$ were produced in heavy-ion induced reactions. In this method, unlike the method of sequential neutron capture, in the fusion process the total mass of the projectile is imported into the target-nucleus. The excitation energy of the compound nucleus is determined by the simple relation:

$$E^* = E_p - [M_{CN} - (M_p + M_T)] = E_p - Q \quad (2.1)$$

where E_p is the projectile energy; M_{CN} , M_T and M_p - the masses of the compound nucleus, the target and the projectile, respectively. The minimum excitation energy, E_{min}^* , is realized at the threshold energy of the fusion reaction, corresponding in first approximation to the Coulomb barrier: $E_{min}^* = B_C - Q$. For heavy target nuclei, $B_C \sim 5 MeV/A$. Contrary to (n, γ) -reactions, where the excitation energy of the nucleus amounts to about $6-8 MeV$, in fusion reactions induced even by an ion as light as 4He , $E_{min}^* \simeq 20 MeV$. This increase of excitation energy of the compound nucleus is due to the increase of the Coulomb barrier with the projectile atomic number. The transition of the excited nucleus to the ground state ($E^* = 0$), formation of evaporation residue (ER), will take place mainly by the emission of neutrons and γ -rays. The production cross section of any evaporation residues can be written as:

$$\sigma_{ER}(E^*) = \sigma_{CN}(E^*) \cdot P_{surv} \quad (2.2)$$

where $\sigma_{CN}(E^*)$ is the cross section for producing the compound nucleus, P_{surv} - survival probability of the compound nucleus against fission. For the ERs cooled by

xn channel, production cross section is:

$$\sigma_{ER}^{xn}(E^*) = \sigma_{CN}(E^*) \cdot P_{xn} \quad (2.3)$$

where P_{xn} - the probability of its deexcitation (cooling) via x neutrons emissions. From eqs. 2.2 and 2.3 one can easily state that P_{surv} is mainly determined by probabilities of neutron emissions from all open xn channels. P_{xn} itself can be expressed as:

$$P_{xn} = \prod_{i=1}^x \frac{\Gamma_n}{\Gamma_{tot}}(< E_i^* >) \quad (2.4)$$

here Γ_n/Γ_{tot} - the ratio of the widths of neutron emission and the total width of decay along the cascade of sequential emission of x neutrons at a mean excitation energy $< E_i^* >$ after each neutron emission. The ratio Γ_n/Γ_{tot} can be calculated in the framework of the statistical theory with some assumptions about the thermodynamical properties of the heated nucleus. The quantity σ_{ER}^{xn} sharply decreases with the increase of E^* (which is equivalent to the increase of the number x of the neutron evaporation steps). Besides, the amplitude of the shell correction, which hinders the fission of the nucleus, quickly diminishes with the increase of the compound-nucleus excitation energy. For these two reasons, the ER production cross section of heavy nuclei becomes extremely small. This cross sections are of the order of $10^{-6} - 10^{-4}$ barn and exponentially fall with the beginning of the region of heavier nuclei, approximately Md isotopes, see fig. 1.1. The cross sections $\sigma_{ER}(E^*)$ are very small when compared to the cross sections of tens and hundreds barn, obtained in (n, γ) - reactions, which lead to the production of actinide elements. This is a very serious limitation for using heavy ion induced fusion reactions, however they appear so far to be one of a few, if not the only means of synthesis of transfermium elements ($Z > 100$). Another approach to produce SHE elements will be presented in chapter 5.

The lower the excitation energy (E^*), the higher the cross section ($\sigma_{ER}(E^*)$). For this reason, preferable are the most asymmetric reactions, having as low as possible values of the Coulomb barrier. This factor has been decisive in the synthesis and investigation of new elements since 1955 for the next 25 years. The main efforts were directed to produce in high-flux reactors enough quantities of the heavy isotopes of transuranium elements from Pu to Es . They were used as target material in the synthesis of new elements at heavy-ion accelerators. This approach led to the discovery of 6 new elements with $Z=101-106$ mainly at the LBNL and in the Flerov Laboratory of Nuclear Reactions (FLNR). Unfortunately, not only the low survival probability of highly excited heavy nuclei, but also difficulties, connected with the production of target materials in high-flux reactors, strongly limited the possibilities to use such reactions for the synthesis of elements with $Z > 106$.

2.2.1. Cold fusion of massive nuclei

The minimum excitation energy of a compound nucleus $E_{min}^* = B_C - Q$ grows up to a certain value when increasing the projectile mass (fig. 2.1a). Any further increase of the ion mass (and the corresponding decrease of the mass of the target nucleus) will reduce E^* since Q -value noticeably increases for more symmetric reactions. The

2. Overview of the past and present status of SHE ...

optimum result is achieved when a doubly magic nucleus such as ^{208}Pb is used as the target. In this case the mass excess, and therefore the Q -value, is highest. Such an effect should be observed already in the synthesis of Fm isotopes in the $^{40}\text{Ar} + ^{208}\text{Pb}$ reaction, in case fusion of such heavy nuclei is possible. This reaction was chosen by Dubna group in 1973 in order to check the idea [30]. The cross sections for the production of Fm isotopes in the reaction $^{40}\text{Ar} + ^{208}\text{Pb}$ as well as the results of experiments, carried out by A.Ghiorso et al. [31] for the same nuclei, but formed in the more asymmetric reaction $^{16}\text{O} + ^{233}\text{U}$, are shown in fig. 2.1b. From the experimental data it follows that the maximum yield of Fm isotopes in the reaction $^{40}\text{Ar} + ^{208}\text{Pb}$ corresponds to the emission of two or three neutrons from the compound nucleus ^{248}Fm ($E_{min}^* = 30 \text{ MeV}$).

In the case of the lighter projectile in the reaction $^{16}\text{O} + ^{233}\text{U}$ the residual nuclei are the result of 4- or 5-neutron emission from the compound nucleus ^{249}Fm ($E_{min}^* = 45 \text{ MeV}$). It may seem strange that the ER cross sections, obtained in reactions of the type $HI + ^{233}\text{U}$, should rise with increasing the projectile mass, while the reaction mechanism and, in particular, the fusion probability of such complex nuclei remain unchanged. The highest cross section corresponds to the case when both nuclei, of the projectile and of the target, are magic. Actually, in the reaction $^{48}\text{Ca} + ^{208}\text{Pb}$ ($E_{min}^* = 20 \text{ MeV}$) the production cross section of evaporation residues - the isotopes of No ($Z=102$) - turned out to be 2 orders of magnitude higher than the cross sections for producing the Fm isotopes, fig. 2.1c. Here the channel with emission of only one neutron is observed with a noticeable cross section. In the experiments, performed later in GSI Darmstadt, it was shown that in reactions using heavier projectiles up to ^{70}Zn , as was expected, the excitation energy of the compound nucleus diminishes and the $1n$ -evaporation channel dominates in the process of formation of very heavy nuclei [33]. As a result, similar to the case of thermal-neutron capture by the ^{235}U nucleus, when the excitation energy imparted into the compound system is $E^* \sim 6 \text{ MeV}$, in the fusion reactions of the ^{208}Pb target-nucleus and the ions, whose mass is 50-70 a.m.u., a compound nucleus can be formed, which has an excitation energy amounting to only 10-15 MeV ! Reactions of this type were called "cold" fusion reactions while the formerly used asymmetric reactions, which led to more heated nuclei, are known as a "hot" fusion reactions.

The "cold" fusion reactions considerably changed the state of art in the issue of the synthesis of new elements. Since in such reactions as target material the stable isotopes of ^{208}Pb or ^{209}Bi were used, the experimental investigations aimed at the synthesis of heavy nuclei became accessible to a wide group of researchers. In this situation the effort was put for the development of accelerator facilities which can deliver intense beams of heavier ions ($A > 50$) what determined the sensitivity of the performed experiments. On the other hand, in fusion reactions of ^{208}Pb even with nuclei of the heaviest stable isotopes, used as projectiles, the obtained compound nuclei are neutron deficient. The evaporation residues are usually far away from the β -stability line, which leads to a significant decrease in their half-lives. These two factors, which lie in the basis of "cold" fusion, i.e. the production of intense beams of ions with $A > 50$ and the necessity to use fast methods of separation and detecting of new nuclei ($T_{1/2} > 1 \mu\text{s}$), significantly changed the experimental approach to the synthesis of new elements. A successful solution of the problem was found in 1975 in GSI by building a heavy ion accelerator, the UNILAC, and the SHIP experimental

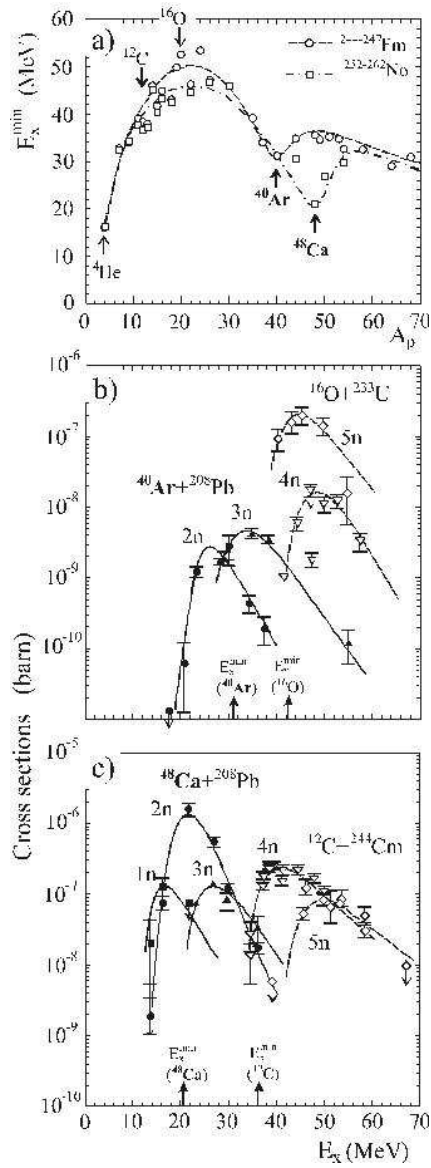


Figure 2.1.: a) Minimum excitation energy of compound Fm and No nuclei, produced in fusion reactions with ions of different mass. b) Formation cross sections of Fm isotopes as a function of the excitation energy of the compound nucleus, obtained in reactions induced by ^{16}O (open symbols) and ^{40}Ar (black symbols). c) Formation cross sections of No isotopes as a function of the excitation energy of the compound nucleus, obtained in fusion reactions induced by ^{12}C and ^{48}Ca . The excitation energy at the Coulomb barrier is shown by vertical arrows. Ref. [32].

2. Overview of the past and present status of SHE ...

setup. This made it possible to separate in flight ($t \sim 10 \mu s$) atoms of new elements among the enormous amount of background products of incomplete fusion reactions. In cold fusion reactions of ^{208}Pb and ^{209}Bi targets with ions ranging from ^{54}Cr to ^{70}Zn were synthesized the 6 heaviest elements with $Z=107-112$ (see tab. A.2). A detailed description of the experiments and the data analysis can be found in the review articles of Armbruster [34], Münzenberg [35] and Hofmann [6].

In cold fusion reactions with ^{208}Pb or ^{209}Bi targets, the increase of the atomic number and the mass of the evaporation residues of the compound nucleus are totally determined by the charge and mass of the projectile. However, the cross section for producing nuclei of the new elements, as it follows from the experimental data, considerably decreases with increasing the element number (fig. 1.1).

Such a tendency has been analyzed for the first time by Świątecki [36] and Błocki [37]. They concluded it is the result of dynamical limitations on fusion due to the increase of the Coulomb repulsion when using more symmetric combinations of mass and charge of the interacting nuclei. The two factors, which determine the cross section for producing the evaporation residues, work here one against the other: when the projectile mass increases, the survival probability increases since E_{min}^* decreases, at the same time the probability of formation of the compound nuclei themselves abruptly decreases. From above experimental facts the following conclusions can be drawn. The reactions of sequential slow-neutron capture, in which β -stable and neutron-rich nuclei are produced, are limited by mass $A=257$. In principle, such limitations do not exist in heavy ion reactions. However, in both cold and hot fusion reactions the cross sections for producing new elements exponentially decrease with increasing the atomic number Z . The reasons for this are different. While in hot fusion reactions the losses are connected with the low survival probability of the evaporation residues, in reactions of cold fusion this is due to the small probability of fusion leading to the formation of the compound nucleus.

In such a situation one have to look for a compromise, having in mind that the ERs will have maximum neutron excess. We should note that no combination of stable or even long-lived isotopes can bring us to nuclei in the center of the "island of stability" with $Z=114$ and $N=184$. One of the possibility is to use radioactive ion beams to produce superheavy elements. However, in order to synthesize nuclei close to the peak of the "island of stability" it is necessary to accelerate still unknown neutron-super rich isotopes, such as ^{54}Ar or ^{90}Ge . The yield of these extremely exotic nuclei in the production target is negligibly small. Nonetheless, one can expect to approach the boundaries of this unknown region so close as to come into the region of influence of the spherical shell $N=184$.

As follows from the discussion presented so far, in the transition region between deformed and spherical shells the stability of nuclei rapidly diminishes. This is connected first of all with changes in the mass and shape of the nuclei in the ground state and with the changes in the structure of their fission barriers. The stable spherical configuration appears only when $N>170$, where according to the macro-microscopic calculations the stabilizing effect of the spherical shell $N=184$ should manifest itself. Such neutron-rich nuclides can, in principle, be produced if as target material and as projectiles heavy isotopes of the actinides with $Z=94-98$ and ions of the very rare isotope ^{48}Ca are used, respectively. The compromise implies that although we sacrifice the magicity of the target-nucleus by the transition from ^{208}Pb

to the neutron-rich isotopes of the actinide elements, we acquire it again in the projectile nucleus. Because of the significant mass excess of the doubly magic nucleus ^{48}Ca , the excitation energy of the compound nucleus at the Coulomb barrier amounts to about 30 MeV. The cooling of the nucleus will take place by 3-neutron emission and by the emission of γ -rays. It can be expected that at this excitation energy the shell effects still exist in the heated nucleus, which in turn increases the survival probability of the ERs in comparison with the case of hot fusion reactions ($E^* > 50$ MeV). On the other hand, the mass asymmetry of the nuclei in the entrance channel ($Z_1 \cdot Z_2 < 2000$) should lead to the decrease of the dynamical limitations on nuclear fusion and, therefore, to the increase of the cross section for producing the compound nucleus as compared to the case of cold fusion reactions. What more the recent development of experimental techniques and the possibility to produce intense beams of ^{48}Ca ions have enabled an increase of the sensitivity of experimental studies by a factor of hundreds. This way of research was chosen by the Dubna which succeeded to discover (synthesize) elements of atomic number $Z=114, 116, 118$.

As mentioned earlier, the properties of the new nuclides and new SHE elements considerably changed our views about the stability of heavy nuclei and also led to the development of the theoretical concepts concerning the existence of superheavy elements.

2.2.2. Experimental approach and detection setup

The planning of experiments on the synthesis of superheavy elements is determined to a great extent by their radioactive properties and mainly by the life time of the atoms to be synthesized. The life time, as mentioned earlier, can vary in a wide range from few μs up to several hours. Hence the experimental setup should be sufficiently fast. On the other hand, the evaporation residues, whose yield is extremely small, should be quickly separated from the enormous background of incidental reaction products, which are formed with a probability 8-10 orders of magnitude higher. These conditions can be satisfied if the separation of the products is performed in-flight (during $10^{-6} - 10^{-5}$ s), taking into account the kinematic characteristics of the different reaction channels. It should be noted that in fusion reactions, leading to the production of compound nuclei, a total momentum transfer from the projectile to the composite system takes place and as a result the momenta of the recoil atoms are well determined. The aim is now to separate the recoil atoms, emitted in a narrow angular interval ($\vartheta_L = 0^\circ \pm 2^\circ$) with respect to the beam direction, according to their velocities (or energies). Such an operation can be performed by the Wien velocity selectors (the separator SHIP in GSI or LISE3 in GANIL) or the energy selector (the separator VASSILISSA in JINR [38]), where the reaction products are separated in-flight according to the electric rigidity in transverse electric fields.

Essentially, such operations can also be performed by other techniques, such as gas-filled separators, where the separation of the recoil atoms is achieved by the magnetic rigidity in a gaseous hydrogen or helium atmosphere at a pressure of about 1 torr (fig. 2.2¹). The recoil atoms leaving the target and the beam have equal momenta and close charges. This does not allow separating them according to magnetic

¹ Further I discuss the general principle of SHE detection techniques on the example of JINR experimental setup, as presently this is the most successful group in the field.

2. Overview of the past and present status of SHE ...

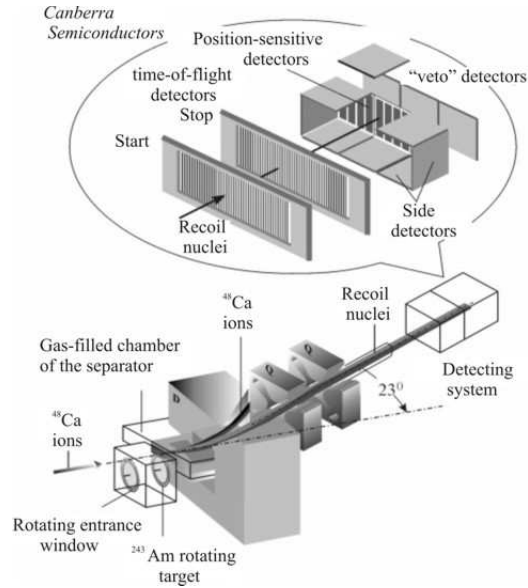


Figure 2.2.: Gas-filled recoil separators (GFRS) used at FLNR in the experiments aimed to synthesize new elements and the detector array used to register the recoil nuclei and their radioactive-decay products. Ref. [32].

rigidity. However, due to the difference of their kinetic energies they have different electric rigidity and can be separated when they pass through a transverse electric field. The picture changes when the atoms move in a gaseous medium. According to Bohr's theory as a result of multiple interactions the moving atom attains an equilibrium charge [31]. Due to the different velocities of the heavy recoil atom and the bombarding ion their equilibrium charges considerably differ from each other. This effect is most strongly seen at small velocities of the recoil atoms, close to the Bohr velocity ($V_B = 2.19 \cdot 10^8 \text{ cm/s}$). Hence the separation of the evaporation residues from the ion beam and other nuclei can be achieved owing to the large magnetic rigidity of the recoil atoms. The efficiency of the kinematic separators depends on the ratio of the masses of the interacting nuclei. For fusion reactions induced by relatively light projectiles ($A_p < 20$) it amounts to only a few percent, but increases to 30-50% when going to ions with mass $A_p > 40$.

Despite high selectivity of a typical experimental setup, in the focal plane practically all the background from the primary beam and from the products of incomplete fusion reactions is suppressed by a factor of $10^8 - 10^{10}$, this is, however, not enough for the identification of the extremely rare events that correspond to the production of atoms of a new element. For this reason the selection of the interesting nuclei is accomplished with a complicated registration equipment, which is schematically presented in fig. 2.2. The recoil atoms, which have reached the focal plane, are implanted into a multi-strip silicon semiconductor detector, which has an active area typically of $30 - 50 \text{ cm}^2$. Each strip has longitudinal position sensitivity. The position resolution depends on the particle type (recoil nucleus, α -particle or spontaneous fission fragments). However, as a rule, more than 95% of all charged particles, accompanying the decay of the implanted atom, are confined in the interval $x \sim 2.5 \text{ mm}$. In this way the whole area of the front detector is split up into about 200-400

individual cells, each one bearing information on the time of arrival of the recoil nuclei, their energies and, next, on the time of the consequent decays with measurement of their energy. The front detector is surrounded by side detectors so that the entire array has the shape of a box with an open front wall. In this way the detection efficiency for particles resulting from the decay of the implanted nucleus (α -particles or fission fragments) is increased to 85-87% (Dubna case).

For distinguishing between the signals of the recoil nucleus and those belonging to the particles from its decay, a time of flight (*ToF*) detector is situated before the front detector. The signals from the *ToF* detector are used also for determining the velocity of the implants. In principle, the velocity and the energy of the implanted nucleus allow to determine its mass. Unfortunately, due to the usually short flight-path of the *ToF* detector and the distortion of the energy signal, caused by the "dead layer" of the strip detector and pulse height defect, the mass of the recoil atom is determined with large uncertainty (~ 50 mass units). This does not exclude, however, the use of other, independent methods of determining the mass of the recoil atom, which will significantly raise the reliability of the evaporation residue identification.

The parent nucleus, implanted into the detector, can be reliably identified if the decay chain of its sequential β - and α -decays leads to nuclei with known properties. This method was successfully used in the experiments on the synthesis of new elements with $Z=107-112$ with neutron excess $N-Z < 53$. Advancing into the region of spherical, more neutron-rich nuclei ($N-Z > 60$) this advantage is lost. Here the decay of the parent nucleus results in the formation of hitherto unknown more neutron-rich nuclei, whose properties can be only predicted with precision allowed by the theoretical calculations. At the same time any decay chain of sequential β - and α -decays the daughter nuclei move more and more away from the closed spherical shells. This should result in a considerable increase of the probability of their spontaneous fission in comparison with other decay modes. Finally the decay chains will be terminated by spontaneously-fissioning nuclei. In principle, such a decay scheme appears to be a reliable sign of the formation of a superheavy nucleus.

2. *Overview of the past and present status of SHE ...*

3. Superheavy elements production at GANIL

In 1999, the program for superheavy elements (SHE) production began in GANIL. The first measured reaction of synthesis was $^{86}\text{Kr}+^{208}\text{Pb}$. We decided to study this reaction as, at that time the Berkeley group announced the discovery of a new element $Z=118$ created in the fusion process of Kr and Pb ions. Our aim, in this study, was to confirm or refute the synthesis of nucleus $Z=118$. Since then several experiments were performed in which we studied fusion reactions in normal kinematics: $^{54}\text{Cr}+^{208}\text{Pb}$, $^{58}\text{Fe}+^{208}\text{Pb}$, $^{76}\text{Ge}+^{208}\text{Pb}$, and in inverse kinematics: $^{208}\text{Pb}+^{12}\text{C}$, $^{208}\text{Pb}+^{18}\text{O}$ [39, 40, 41].

In the next sections I will present in details those experiments. The presentation will start from the description of the experimental setup that was used in the measurements.

3.1. GANIL experimental setup

Experiments were conducted in the GANIL experimental area of LISE3¹. A schematic overview of the experimental setup is presented in fig. 3.1. The main components of the setup are: reaction chamber, Wien filter, magnetic dipole and detection chamber.

3.1.1. Reaction chamber

Due to the high beam intensity of 10^{12} particles/s and the low melting points of the targets (mainly Pb targets) we use, instead of the stationary targets, a rotating target system mounted in the reaction chamber - zoomed lower left part of fig. 3.1. There is a wheel of 670 mm in diameter which bears 35 targets. The second wheel of the same diameter is mounted behind the target wheel. This wheel supports carbon stripper foils in order to re-equilibrate the charge state of the evaporation residues. Rotation of the wheels, 2000 rpm, is synchronized with the time structure of the beam in such a manner that the target holders are never hit by the beam particles.

Operation of the system, synchronization and the targets condition, is monitored on-line by the hodoscope - silicon detector facing the elastically scattered beam particles. This detector is placed near the target wheel. Because the whole target system operates in a vacuum, the mechanical construction of the system has to be vacuum hermetic. The construction was designed and manufactured in the Daphnia laboratory.

In the chamber a smaller wheel 16 cm in diameter is also mounted with 8 targets for materials with higher melting points. Additionally, small rotating targets 5 cm in diameter are used for the calibration with low intensity beams.

¹ GANIL experimental areas <http://ganinfo.in2p3.fr/user/areas/index.html>

3. Superheavy elements production at GANIL

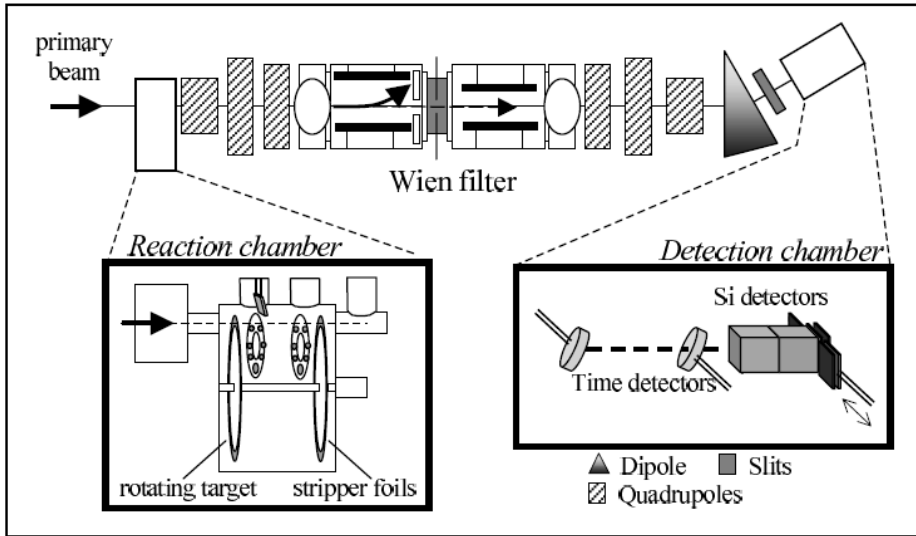


Figure 3.1.: Schematic view of experimental setup for SHE production. From left to right: reaction chamber with two large rotating wheels (one for targets, the other for carbon stripper foils) and two small wheels, two halves of the Wien filter and quadrupoles, a magnetic dipole (black triangle) and a detection chamber with two micro channel plates (MCPs) for *ToF* measurements and an array of silicon detectors in the form of a tunnel.

3.1.2. Wien filter

The main tool of SHE research at GANIL is the Wien velocity filter with angular acceptance of 36 msrad , mounted at the LISE3 magnetic spectrometer, with crossed magnetic and electric fields. This filter is divided into two identical halves. The ratio of the electric to magnetic field is set to the velocity of the complete fusion nucleus e.g. $E/B = v_{CN}$, while their values are chosen in the way that the projectiles are deflected in the first half of the Wien filter and stopped in the Faraday plate. For such tuning of the filter, the trajectory of the ERs² is undisturbed (straightforward) and in consequence the ERs leave the filter and enter the detection setup.

To improve suppression of unwanted events (products of transfer reactions, ion pipe scattering projectiles, etc.) two pairs of independently movable slits, horizontal and vertical ones, were installed in the mid filter.

A dipole magnet is located after the Wien filter. With this magnet even more unwanted events can be removed thus the background in the detector is minimized. The transmission of the fusion nuclei from the target through the whole filtering system (quadruples, Wien filter magnetic dipole) was studied by the simulation code ZGOUBY[42].

The first test experiments showed that modifications in the experimental setup are necessary. So the upper electrode of the Wien filter was moved up by 2 cm in order to deflect the beam without hitting the electrode. Additionally a new water-cooled collimator, where the beam is stopped, was installed.

² The mean value of the evaporation residue velocity, v_{ER} , is equal to v_{CN} .

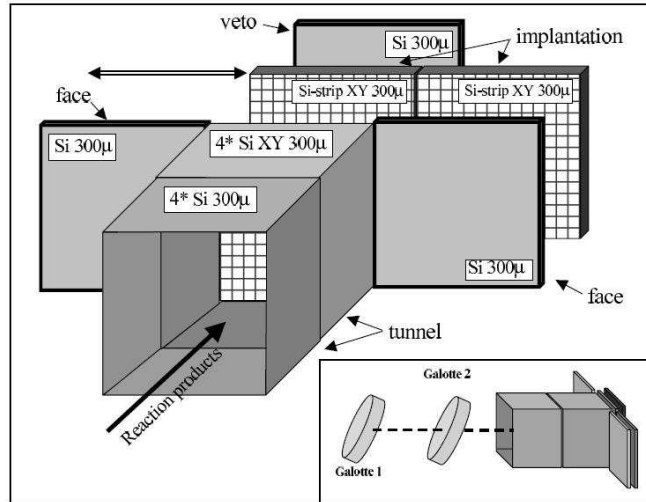


Figure 3.2.: Detection setup situated at the end of LISE3 spectrometer. Main elements: 2 time of flight detectors (Galottes), two movable implantation silicon strip detectors, one veto silicon detector behind the “in-beam” implantation detector and two face silicon detectors to recover the products (α or fission fragments) escaping the “out of beam” implantation detector and 8 tunnel detector to increase detection efficiency for the products (again α or fission fragments) of the decay of the implanted residues.

3.1.3. Detection setup

The main elements of the detection setup, shown in fig. 3.2, are: two micro channel plates (Galottes) for the time of flight measurements of the heavy ions coming from the beam direction, a tunnel which is composed of 8 silicon position resistive detectors and the silicon strip implantation detector (IMP) of 48 strips for X and Y measurements.

The implantation silicon detector returns signals on energy and position X-Y which corresponds to the implantation of the heavy residue (superheavy nucleus) and the signals for each of the emitted alpha particles (energy, X-Y) by that implanted residue. The time signals from the acquisition (ACQ) clock are also recorded. Between the time tags of the ER detection and its α (or spontaneous fission) radioactive decay, different heavy ions (scattered beam, transfer products) and light particles (mainly protons) are implanted into the detector what gives the background.

As the efficiency of the Galottes for the light particles detection is smaller than 100% two of them are used. Then the implantation events are defined as an energy signal in the Si implantation detector, in coincidence with both Galottes while α or fission fragments are those which produce the energy signal in the Si detector in anti-coincidence with Galottes.

The implantation detector is $300 \mu m$ thick and has dimension $5 \times 5 cm$. The distance between strips is about $45 \mu m$ thus the dead zone of the IMP detector is below 5%. Two such detector are mounted on the movable arm. When the α particle emission is identified by the electronics and by the on-line analysis software, the beam is stopped for a short while, then the detector is moved out of the beam and next, the second detector is put in its place and the beam is switched on. This techniques

3. Superheavy elements production at GANIL

enable us to observe even very long time α chains which are completely free of the background coming from the beam.

The ERs are implanted in the IMP at the depth of the order of 10 μm which is smaller than the range of α particles with energy $> 2.5 \text{ MeV}$ in the silicon material. To measure the full energy of α particles escaping the implantation detector, i.e. when the decaying ER emits alpha particles in the backward direction, a set of 8 Si detectors was mounted in the “tunnel” geometry. With such a geometry of the detection setup efficiency for alpha detection goes up from 55% to 95%.

In front of the out-of beam position of the implantation detector a face silicon detector is situated. This gives almost 100% efficiency for the alpha or fission decay of the ERs implanted in the detector. Behind the implantation detector an additional veto detector is mounted. This detector can be used to diminish the background due to the light particles coming from the direction of the beam. All Si detectors are mounted on a copper support and cooled to reduce electronic noises.

3.1.4. Data acquisition system

The first α starting the α -radioactive chain originating from the decay of ER can be emitted as soon as a few tens of μs after the implantation of the ER. To acquire data we use the VXI system for which the dead time is ca 150 μs .

As the detection of all α particles from the chain is essential for proper identification of the decaying ER (superheavy nucleus) a special approach in the electronics acquisition system was used to reduce the dead time of electronics. A multi-trigger logic with two independent sets of ADC converters was applied while one hard trigger³ was used for both sets. This works in the following way: the trigger generated by electronics enters into two GMT (GANIL master trigger) modules T1 and T2. In the case of low counting rate and long lived ER (time between successive α emission greater than 150 μs) the triggers are treated as the T1 and the events are registered in the first set of converters. At this stage this is the normal method used in many experiments. At the same time detector signals are duplicated into the second set of converters but are not digitized by the acquisition system. When the next trigger occurs during the dead time of the T1 modules it is treated by the T2 master trigger and digitized by the second set of ADCs while the T1 deals with the proceeding event. This way it was possible to reduce dead time of the whole acquisition to 30 μs . The converters are 14-bits ADCs giving the resolution for α particles of the order of 50 KeV and a dynamical range from 300 KeV to 250 MeV (what is necessary for fission fragment energy measurements).

The fast analysis program allows to identify on-line α -decay chains or spontaneous fission and to decide to stop the beam in case of a good candidate for a superheavy element. The analysis performed by this program can be repeated also off-line.

To reach very short decay times of the order of a few μs and a large dynamic range in the energy measurements from 1 MeV to 1 GeV a special fast electronics will be designed in the future. This will be digital electronics placed after the front-end analog electronics with the capability to process events signals without limitation of the recovery time of the preamplifier.

³ Which is detection of a particle in the IMP detector.

3.1.5. Fast analysis software for on-line SHE identification

Experiments aimed at superheavy elements production via nuclear collisions possess their own specificity. Due to very low cross sections for SHE production only 1 to a few cases of synthesis can be registered per accelerator work day. Synthesized SHE nucleus has a low excitation energy and after the emission of 1-2 neutrons (cold fusion, $E^*=10-20 \text{ MeV}$) or several neutrons (hot fusion, $E^*=30-50$) returns to the ground state and then due to its radioactivity emits a sequence of α s or/and decays by spontaneous fission.

The scheme of the radioactive decay is presented in fig. 3.3. As a result of such decays an alpha chain is generated. Each alpha in the chain has characteristic kinetic energy and emission time governed by the half-life ($T_{1/2}$) of the emitter (parent nucleus). Such a decay chain can be used to unambiguously identify Z and A of the produced SHE element.

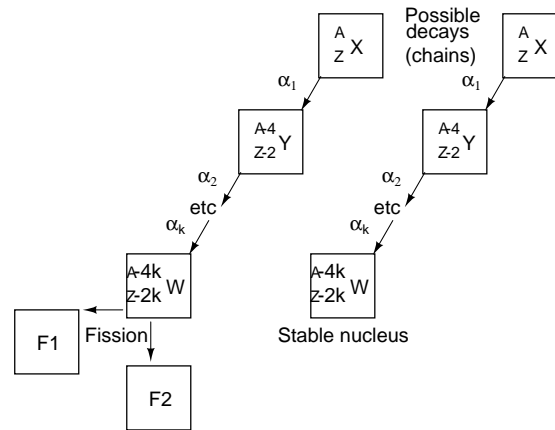


Figure 3.3.: Two possible scenarios of the decay paths (chains) from a ground state of a radioactive nucleus ${}^A_Z X$. Nucleus X emits k alphas and then a fission occurs (left side of the picture) or a stable nucleus is reached (right side of the picture).

The objective of the detection setup is to register the decay chain. For this purpose a silicon position detector is most suitable. SHE implants in this detector. The detector recognizes all subsequent α or fission emissions. In order to identify the chain one has to correlate events which are coming at different times but are from the same position of the detector. Experimentally it is important to identify the chain on-line. There are a few reasons for that:

- minimization of the background. Our detection setup has two implantation detectors, one in-beam position and one off-beam position. If the first alpha occurs and is correlated in position with the implanted residue we shift the in-beam detector outside the beam (now this detector is background free) and place the off-beam detector into the beam. But to do that one needs to know immediately that such a correlation occurred.
- optimization of the beam energy. Excitation functions for compound nuclei are narrow and not very well known even for already discovered superheavy

3. Superheavy elements production at GANIL

elements. To tune the beam energy to the region of maximum cross section it is necessary to identify the decay chains in the on-line mode.

- Wien filter tuning. The velocity window of the filter is set by using pilot reactions which produce several radioactive isotopes, typically in the region of *Th*, *Pa*, *Ra*, *Ac* nuclei. Those nuclei have different velocities. Again, real time recognition of α chains identifies such isotopes and helps to set the proper velocity window of the filter.

Such on-line correlations can not be performed by a standard acquisition system (SAS). SAS, in principle, reads the event buffer and writes it to a storage system. It can produce on-line 1 or 2- dimensional spectra, often with sophisticated cuts, but no time correlation is accessible. For these reasons, we decided to develop the software for fast, on-line identification of α -decay chains. What is more, the study of superheavy element production is a long term program in GANIL thus the software should be useful for quite a long time.

Let us assume that in a given event, the signal from heavy radioactive residue (ER) which implants in the silicon detector is recorded. This residue emits, after that, a sequence of alpha particles (alpha chain) and each alpha of that sequence is registered as a separate event. Heavy residue and its α -decays can be recognized among many other events recorded during the measurements as they are correlated in position (same position) and in time (they emerge in time sequence). To find the chain in the on-line analysis, a program should be able to maintain the characteristics of all events from the time interval minimum 5 to 6 times longer than the decay time of the last daughter nucleus of the decay alpha chain. The next few paragraphs present the implemented program more in detail.

This program makes use of the Global Section (VAX/VMS) or shearing memory (Linux) mechanism. The idea is that the software, when running, can export part of the RAM memory it occupies to the operating system of the computer and then other processes/programs can have access to it. The two different models of a common memory (Global Section/shearing memory) are transparent for the user as we use the CERN library. It is completely independent of the standard acquisition software of GANIL (GANIL software is responsible for collecting the data and recording it to the mass storage media). Initially it was developed under VMS operating system and after that adapted for Linux systems.

The operation of the software is presented in fig. 3.4. A concept of the circular buffer with ntuple structure⁴ is used to maintain events with subsequent time tags. The circular buffer can store physical variables of n recent events. Software is divided into two parts, the first one which we call A takes the raw signals from the acquisition buffer, then it transforms them into physical variables like strip number, energy of the ion, *ToF*, etc. Finally all the calibrated variables are put into the circular buffer of the ntuple-type which is located in the RAM memory of a computer.

The second program B checks that the buffer, using a memory mapping mechanism, periodically, and every time a new alpha arrives, searches the circular buffer to find the α -decay chain: all previous alphas and heavy residue with the same position of the implantation detector as the newly detected alpha. If it finds a chain

⁴ Data representation used by the PAW (Physics Analysis Workstation) software created in CERN laboratory.

it displays its characteristics on the screen monitor and writes it to the file. The set of events is memorized in such a circular ntuple-like buffer from the last one-three hours of the measurements depending on the counting rate of the detector system for a given experimental run.

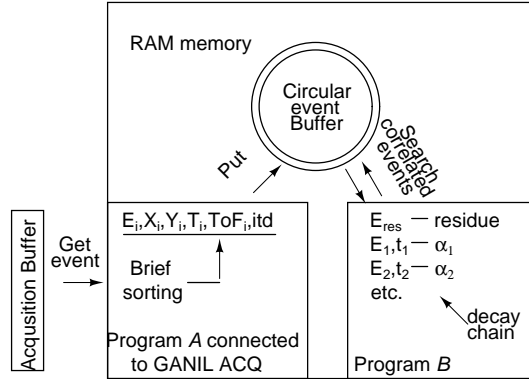


Figure 3.4.: Schematic view of the fast analysis software. Program A reads event acquisition buffer, converts raw data to the calibrated energy, position X and Y, time tag and time of flight (ToF) for each detected particle and sends calibrated event into circular buffer. Program B searches regularly the circular buffer for correlations between alphas and heavy residue, and signals immediately if it finds decay chain.

Both programs are running on the same computer that has access to the acquisition buffer. The first one is completely independent of the program B while B as the input has the circular buffer continuously filled by events sorted by program A. In principle the same work could be performed by one piece of software. The reason we adopted the concept of two independently running programs is the following: whenever alpha is detected and its calibrated parameters are sent into the circular buffer, the software has to check usually several thousands (background is always present) of earlier events to find all previous particles correlated with that alpha - of course it takes time. If this work is performed by just one program a danger exists that such a program will miss events which arrive in the meantime to the acquisition system. By dividing the job between two programs which use a mapped memory mechanism such a threat is minimized (they share the time of the computer processor).

The program was written during my stay at LPC-Caen in 1999. It was checked and tested in two experiments carried out at GANIL, one E369 for production of nuclei $Z=106$ and the other FULIS searching for $Z=118$. Since then, it was exploited in all subsequent SHE production experiments at GANIL. Off-line data analysis made for both experiments confirmed all the results obtained from that fast on-line analysis software.

The software satisfies our specific needs in superheavy experiments but can be, I believe, quite easily adapted for other experiments whenever there is a need for efficient and fast on-line searching for very rare events that are correlated in time.

3.2. Experimental results

3.2.1. Energy calibration of the implantation detector

The heavy residue implanted in the silicon strip detector can be identified unambiguously only if it is radioactive. In that case it emits $\alpha(He)/\beta$ particles or/and decays via spontaneous fission. In many cases, after α emission a daughter nucleus is also radioactive and emits subsequent α particle and so on. Such a multiple process of alpha emission one calls an α -decay chain. The chain stops when the last daughter nucleus is stable or fission spontaneously. Each He particle in the chain is characterized by its unique energy and the tag of an emission time. Thus a chain is like a fingerprint, which unambiguously identifies parent residue. To obtain a clear fingerprint for proper identification of a radioactive nucleus it is thus important to measure energy of the emitted α 's with good accuracy, in many cases with a resolution better than 50 KeV.

In this section I will show the modified procedure of the energy calibration of the implantation detector. The procedure gives more precise energy calibration comparing to the one previously used and can be applied for the silicon strip implantation detectors commonly used in this type of experiments. This procedure will be presented on the example of experiment E369 in which the FULIS collaboration has synthesized element $Z=106$ in the reaction $^{54}Cr + ^{208}Pb$.

In the first step of this experiment two test reactions were used, leading to the fusion of heavy elements in the region of $Z=92-96$. Such reactions are useful to tune the velocity filter (set the proper window velocity) and to test the energy calibration of silicon detectors especially the implantation detector. In our case the piloting reactions are $^{54}Cr + ^{165}Ho, ^{nat}Gd$. If fusion takes place these two reactions lead to the nuclei $Z=91$ (Pa) and $Z=88$ (Ra) respectively.

The first point refers to previous energy calibration of the implantation detector. The calibration with the Am source performed during the experiment is rough and not very useful for further data analysis, e.g. each time we observe alpha decay of radioisotope ^{261}Sg , kinetic energy of emitted α particle is different, see column 4 in table 3.1. Using this calibration it is also difficult to attach α chains that we observe in the pilot reactions $^{54}Cr+^{165}Ho, ^{nat}Gd$ to the proper radioactive isotopes produced in these reactions. I propose here another calibration method to obtain more accurate and reliable energy calibration of the implantation detector.

For each particle (event) detected in the implantation detector we get two energy signals one from horizontal strip and one from vertical strip⁵. In the method, we use both signals to make the energy calibration. At the first step we concentrate on one of the vertical strips e.g. strip no. 10 (one can use, of course, another strip). Each particle that gives signal in that strip gives also signal in one of the 24 horizontal strips. Now we sort on the event-by-event basis all the energy signals from strip vertical no. 10 into 24 2-dimensional histograms. One histogram contains correlation between energy signal from vertical strip 10 and energy signal from horizontal strip number $i = 1, \dots, 24$. Results for the reaction $^{54}Cr+^{165}Ho$ are shown in fig. 3.5. Events which are located on the left side of the principal group of events are due to the incomplete charge collection in the detector and we do not take them into account

⁵ There is 24 horizontal, and 24 vertical active strips. Horizontal strips (Y position) are located in the front face, while vertical strips (X position) are on the back face of the detector.

Table 3.1.: Horizontal and vertical strip numbers (column 1 and 2) as well as raw and calibrated energy signal values received from these strips (columns 2-6) in the case of six alpha particles detected by the IMP detector. The alphas derive from the α -decay of six ^{261}Sg nuclei that were produced in the reaction $^{54}\text{Cr} + ^{208}\text{Pb}$. Details are presented in the text.

Y_{stripH}	X_{stripV}	chY	$E_{\text{old}}(\text{MeV})$	chY1	$E_{\text{new}}(\text{MeV})$
14	20	497	10.03	513.8	9.50
18	20	492	9.86	514.8	9.52
18	3	493	9.88	516.0	9.54
7	3	547	10.21	517.5	9.57
19	16	530	10.32	519.5	9.62
9	17	530	10.21	519.7	9.62

in the next steps of the calibration procedure. Complete signals are localized on the principal line and present correlation between energy signals from strip vertical 10 and energy signals from horizontal strips 1 to 24 i.e.: chE_{h1} vs chE_{v10} , ..., chE_{h24} vs chE_{v10} .

From the figure it is seen that these correlations are not linear and its characteristic changes from panel to panel. At this stage one can say nothing about linearity response of the vertical strip 10 but electronics for this strip is independent from the electronics of horizontal strips. Thus if one observes different behavior of the correlation for each horizontal strip this is because of non-linearity which is present in gain of the signals from the strips of the front face of the detector. In fact non-linearity is the strongest in the range of channels 250-600 (above channel 600 dependence is linear). In this channel region there are located three α peaks of the calibration source Am . This is why calibration based only on the Am source is only approximate. The approach further solves this difficulty.

From the data of fig. 3.5 one can obtain the correlation of energy signals between different horizontal strips. First, the signal value from any horizontal strip can be transformed via the corresponding bin of the vertical strip 10 into the value which corresponds to the signal from another horizontal strip. To do this, 24 profiles - $\langle chE_{hi} \rangle$ vs chE_{v10} ($i=1, \dots, 24$) are generated from 2-dimensional maps of fig. 3.5. Next, horizontal strip 1, the reference strip, was chosen as a strip into which the signal from other horizontal strips will be transformed. Any other horizontal strip can be used as a reference strip. The results of that conversion are shown in fig. 3.6. The conversion was conducted starting from channel no. 250. Next we are fitting data from fig. 3.6 with two types of functions: linear and quadratic:

$$chE_{h1} = a_{hi} * chE_{hi} + b_{hi} \quad (3.1)$$

$$chE_{h1} = A_{hi} * chE_{hi}^2 + B_{hi} * chE_{hi} + C_{hi} \quad (3.2)$$

where hi indicates horizontal strips 2, ..., 24. The results of the fitting for the quadratic formula are presented in the fig. 3.6. The reason why we use these two types of

3. Superheavy elements production at GANIL

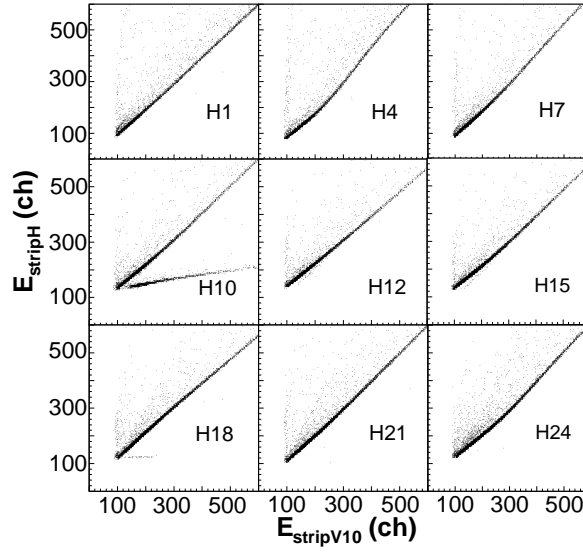


Figure 3.5.: Correlations between energy signals in vertical strip 10 (marked in the text as chE_{v10}) and energy signals in selected horizontal strips (marked in the text as $chE_{h1, \dots, h24}$). Only 9 (of 24) representative horizontal strips are presented. $^{54}\text{Cr} + ^{165}\text{Ho}$ reaction.

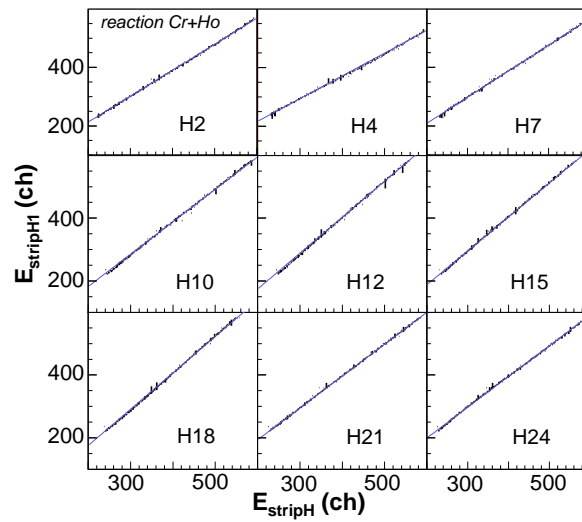


Figure 3.6.: Profiled energy signals from strip horizontal no. 1 versus profiled energy signals from selected, marked on the picture, horizontal strips. Lines are the quadratic formulas fitted to the data points. Reaction $^{54}\text{Cr} + ^{165}\text{Ho}$.

function is that the quadratic formula gives a more precise fit in the channel range [250-600], but is not precise above channel 600, while the linear function gives good results above channel 600 but gives worse results than the quadratic function in the range of channels [250, 600]. In this way all the energy signals from the horizontal strips 2 to 24 can be translated into energy signals of the horizontal strip 1. The set of coefficients a_{hi} , b_{hi} , A_{hi} , B_{hi} and C_{hi} received from fitting is unique for each horizontal strip 2,...,24. This relative calibration is very useful because one has to perform the absolute energy calibration only for strip 1 while the relative calibrations (eqs. 3.1, 3.2) give absolute energy for the rest of the horizontal strips. In case of previous (old) calibration absolute energy calibration was performed separately for each horizontal strip.

Further, to get the absolute energy calibration of the horizontal strip 1 of the IMP detector we choose two known energies of alpha lines. The first line is from Am source. This radioisotope emits alphas with three different energies. Here we took only the lowest energy. The second line is for alphas emitted by the ^{261}Sg . We have discovered six cases where the α emitted by seaborgium has completely deposited its energy in the implantation detector (no escape). These cases were registered by different strips. Using equations 3.1, 3.2 we have translated signal values of each of these events into equivalent signal values of horizontal strip no.1. The result of that transformation is presented in column 5 ($chY1$), table 3.1. Then we obtain the mean translated energy channel value of horizontal strip no. 1, the case of Sg decay, which is equal to 516.8 channels. The same procedure is applied for the lowest energy Am line and the received mean energy channel is equal to 319.5. The values together with known alpha energies of Am (5.70 MeV) and ^{261}Sg (9.54 MeV) were next used to perform energy calibration for horizontal strip no. 1. We have assumed linear dependence for the calibration as we do not know the real functional dependence. It is reasonable because Si detectors and associated electronics in most situations give linear response with the energy of the detected particles. Finally one receives the following energy calibration formulas:

$$E[MeV] = 0.0196 * (A_{hi} * chE_{hi}^2 + B_{hi} * chE_{hi} + C_{hi}) - 0.56 \quad (3.3)$$

$$E[MeV] = 0.0196 * (a_{hi} * chE_{hi} + b_{hi}) - 0.56 \quad (3.4)$$

Here eq. 3.3 is valid for channels [250, 600], while eq. 3.4 applies for channels <250 and >600. This calibration should be very accurate in the energy range [5, 10] MeV and reasonable above 10 MeV. Figure 3.7 presents the difference between this new calibration and the old one on the example of alpha spectra obtained for the reactions $^{54}Cr + ^{165}Ho$, ^{nat}Gd at the beam energy $E=4.689$ MeV/u. Two points can be deduced from the figure: (i) the new calibration gives the position of alpha peaks in agreement with known alpha decay chains, (ii) FWHM for alpha spectra is smaller in the case of modified calibration.

Finally one should mention that our calibration procedure may use any energy signal of the implantation detector (see fig. 3.6), not only known alpha line signals. This can be of special importance in a situation when only a few particles with known energy give energy signals in the IMP as it is for example in the case of α -decay of the Sg element.

3. Superheavy elements production at GANIL

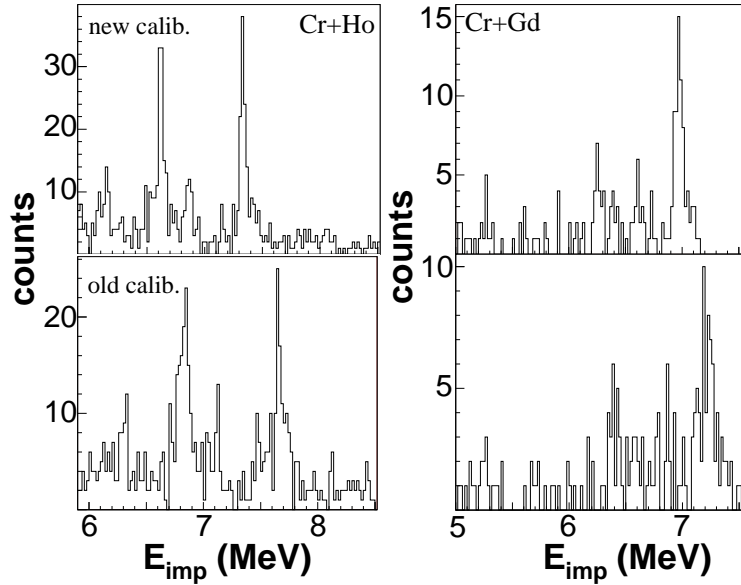


Figure 3.7.: Comparison of new (upper part) and “old” calibration (lower part) for the IMP detector in the case of α energy spectrum collected in two reactions indicated in the figure.

3.2.2. Analysis of the reaction $^{54}\text{Cr} + ^{165}\text{Ho}$, 4.698 MeV/u

In this reaction, fusion leads to the isotope of ^{219}Pa which has excitation energy $E^* = 50 \text{ MeV}$. This nucleus is quite hot and can deexcite by neutron, proton and alpha particles emission. Due to deexcitation, a whole spectrum of the evaporation residues will be produced. The ERs pass through the Wien filter (they have similar velocities which are in the acceptance of the filter velocity window) then they are implanted into the Si detector. Some of these residues are radioactive nuclei. These nuclei after implantation decay by α particle emission. There are several such nuclei in the mass region of $A=210\text{-}216$. The objective of this analysis is to identify such radioactive ERs, isotope par isotope by using the technique of α -decay chains.

The total estimated dose of the beam during irradiation of Ho target ($980 \mu\text{g}/\text{cm}$ of thickness) was $7.28 \cdot 10^6 \text{ nC}$ equivalent of $0.57 \cdot 10^{16}$ ions of Cr .

Based on the example of this reaction we will present in details the analysis which has to be performed to identify radioactive elements by using the technique of α -decay chains. The spectra of α particles received from that measurement were already presented in figure 3.7. Figure 3.8 presents 2-dimensional energy versus time of flight (T_{g1g2}) spectrum of heavy ions implanted in the strip detector. Small values of T_{g1g2} correspond to high velocity of heavy ions while ions in the right part of the map have the smallest velocities. The map shows 4 groups of well separated events. The most intense line marked as Cr -like represents beam-like ions. It is not rejected by the Wien filter because due to a few nucleon transfer reactions part of the Cr -like ions have the velocity in the range of the velocity window set in the filter. Fission-like nuclei can be produced in the target by fission of compound nuclei created in a complete or incomplete fusion process. Kinematics of the fission process shows that part of such fission fragments will have a velocity in the velocity window range

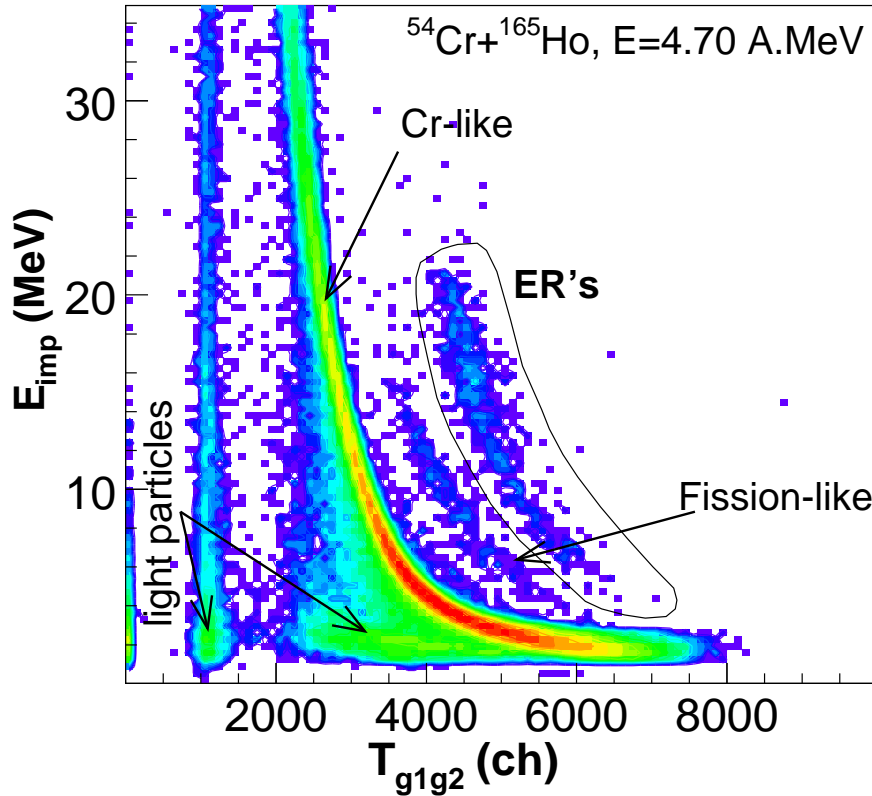


Figure 3.8.: Energy deposited by different reaction products in the implantation detector versus time of flight measured by a pair of Galottes. Velocity window set in Wien filter is in the 4500-5500 channel range. All products with velocity in this range pass through the filter and implants in the IMP. Contour, marked as ER, groups the most heaviest ions produced in the reaction. Between the *Cr*-like line and the ER island there is another clearly visible group which can be attributed to the nuclei originating from the fission process.

of the filter thus will not be rejected by the filter and will implant in the strip detector. Also, during irradiation a whole spectrum of light particles mainly protons is produced which after scattering in the ion pipe pass the velocity restrictions set by the filter and also enter the implantation detector.

For further analysis only the group marked as ER is taken into consideration. This group contains signals from the heaviest nuclei produced in this reaction. The implantation detector registers also subsequent alpha/spontaneous fission decays of implanted heavy residues. The energy spectrum detected by the IMP, marked as “all”, are presented in the upper part of figure 3.9. This spectrum is drawn without any condition set on the energy signals coming from the strip detector. As one can see, it is not possible to distinguish events corresponding to heavy ions from those that represent energy signals of alpha particles emitted by implanted ions. When the energy spectrum of the IMP is collected in anti-coincidence with the time of flight signal produced by the Galottes one obtains the result which in the figure is marked by $!T_{g1g2}$. In this way one should obtain the energy signals from radioactive alpha

3. Superheavy elements production at GANIL

decays of implanted heavy residues. However, this is not the case. The spectrum also contains events generated by light particles coming from the beam direction, due to lower efficiency of time of flight system for light particles, especially protons. Nevertheless we can clearly see the lines which correspond to alpha particles originating from the radioactive decay of the ERs.

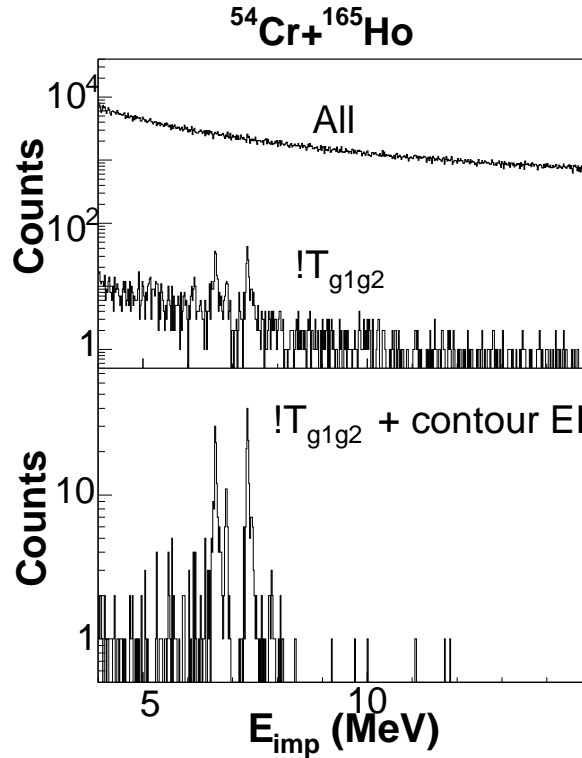


Figure 3.9.: Upper part: “All” - no condition on energy spectrum of strip detector is set, $!T_{g1g2}$ - energy spectrum with the requirement of anti-coincidence with time of light system. Lower part: additionally the same position X-Y as heavy residues (contour “ER” from fig. 3.8) in the strip detector is required (see text for more detailed discussion of that spectra).

In the next step we will construct α particles spectra with the condition that alphas come from the same position as the implanted evaporation residue and are correlated in time with ER within time window equal to 3600 s. Evaporation residues are those which are within contour “ER” of fig. 3.8. Such an alpha energy spectrum is presented in the lower part of fig. 3.9. One sees that now the energy spectrum is cleaner. This is so because the condition of the same position for alpha and heavy ion and time correlation between them eliminates random, coming from beam direction, light (proton) particles which simulate “alpha” decay events. In this spectrum one sees several lines of alphas with well defined energy. This spectrum will be a basis to identified alpha radioactive residues. In order to identify them it is necessary to find all the alpha chains which are associated with radioactive decay of a given evaporation residue. To do this we will analyse the alpha energy spectrum of fig. 3.9 (or upper part in left panel of fig. 3.7) applying a procedure with additional

constrains. The example procedure is the following: one takes the alphas in the peak [6.10, 6.20] *MeV* of fig. 3.9 or 3.7 and reanalysis the data to find all the other alphas that have the same position in the implantation detector as the alpha of peak [6.10, 6.20] *MeV*. Applying this procedure one also finds the characteristics of the residue which is detected in the same position as the alphas. The time window for that procedure is set to 3600 *s*.

Table 3.2.: Alpha chains correlated with residue position, α_2 in the energy range [6.10, 6.20] *MeV* (fig. 3.7, upper left part) was used to locate these chains. Three α -radioactive emitters are identified: ^{211}Ra (No. 1, 2), $^{216}\text{Pa}/^{216}\text{Th}$ (No. 3) and $^{212}\text{Ac}/^{215}\text{Th}$ (No. 4-7). Reaction *Cr + Ho*.

No.	E_{ion} (<i>MeV</i>)	$E_{\alpha 1}$ (<i>MeV</i>)	$E_{\alpha 2}$ (<i>MeV</i>)	$t_{ion} - t_{\alpha 1}$ (<i>s</i>)	$t_{\alpha 1} - t_{\alpha 2}$ (<i>s</i>)
1	20.14	6.83	6.10	21.9257	480.156
2	15.31	6.94	6.12	13.490	751.510
3	17.78	7.89	6.13	0.083	36.6477
4	18.35	7.34	6.14	1.410	1048.3
5	9.04	7.37	6.14	2.0067	795.65
6	17.38	7.32	6.15	0.5116	571.39
7	12.19	7.35	6.16	6.8597	1050.86

The results of the analysis are presented in table 3.2. In this case we have found 7 alpha decay chains coming from three different parent radioisotopes, and each chain is composed of two alphas. From the table one calculates the mean values of alpha energy and the half-life time of the parent and daughter nuclei. The following formula is used for the calculation $T_{\alpha 1} = \langle t_{ion} - t_{\alpha 1} \rangle / 1.44$ and $T_{\alpha 2} = \langle t_{\alpha 1} - t_{\alpha 2} \rangle / 1.44$

Table 3.3.: Characteristics of 9 α -radioactive parent emitters found in the reaction *Cr + Ho*. Characteristics are deduced from experimental data collected in tables: 3.2, A.3-A.8.

\bar{E}_{ion} (<i>MeV</i>)	$\bar{E}_{\alpha 1}$ (<i>MeV</i>)	$\bar{E}_{\alpha 2}$ (<i>MeV</i>)	$T_{\alpha 1}$ (<i>s</i>)	$T_{\alpha 2}$ (<i>s</i>)	AZ	σ (<i>nb</i>)
17.73	6.89	6.11	$12.3^{+33.9}_{-8.1}$	$7.1^{+19.9}_{-4.5} * 60$	^{211}Ra	0.097
17.78	7.89	6.13	$0.06^{+0.41}_{-0.045}$	$25.4^{+175}_{-19.4}$	$^{216}\text{Pa}/^{216}\text{Th}$	0.049
14.24	7.35	6.15	$1.87^{+2.8}_{-1.0}$	$10^{+14.9}_{-5.6} * 60$	$^{212}\text{Ac}/^{215}\text{Th}$	0.195
16.1	7.33	6.61	$0.78^{+0.22}_{-0.18}$	$50.8^{+14.6}_{-12.0}$	^{212}Ac	1.90
16.51	7.43	6.73	$0.41^{+0.31}_{-0.17}$	$13.5^{+10.8}_{-5.6}$	^{211}Ac	0.438
14.3	7.43	6.87	$1.23^{+1.05}_{-0.52}$	$18.3^{+16.4}_{-7.75}$	^{215}Th	0.390
16.7	7.91	6.85	$38^{+66}_{-21} * 10^{-3}$	$16.3^{+32.7}_{-9.2}$	^{216}Th	0.146
17.27	7.81	7.37	$0.16^{+1.26}_{-0.13}$	$0.24^{+1.53}_{-0.21}$	^{216}Pa	0.049
14	8.08	7.43	$2.5^{+7.7}_{-1.7} * 10^{-3}$	$0.17^{+0.49}_{-0.12}$	$^{214}\text{Pa}/^{215}\text{Pa}$	0.097

3. Superheavy elements production at GANIL

for the first and second decay in the chain, correspondingly. Alpha chains are characterized by these values and are subsequently used to identify radioactive nuclei. Such a procedure is applied for other peaks from fig. 3.7/3.9. All the chains we found are presented in tables A.3-A.8. Using the data of those tables we identified 9 different radioactive nuclei produced in the reaction $Cr + Ho$. Alpha decay energies and half-life time of those radionuclides are collected in table 3.3. In a few cases it was difficult to associate the chains to the proper parent nucleus. This is due to the fact that in this region of nuclides chart there are radionuclides which produce alpha decay chains with very similar characteristics. Those cases are marked in table 3.3.

Finally one can calculate the production cross section for the radioactive nuclei we found in the analysis. For that, the following formula was used:

$$\sigma = \frac{N_{ev}}{N_t * N_{beam}} * 10^{23} [nb] \quad (3.5)$$

$$N_{beam} = Q * 1/8 * 6.25 * 10^9 [particles] \quad (3.6)$$

$$N_t = 6.02 * 10^{17} * \rho/n_t [nuclei/cm^2] \quad (3.7)$$

where N_{ev} - number of observed events, N_t - number of target nuclei per cm^2 , N_{beam} - beam dose (number of beam particles that irradiate target), ρ - target density in units of $\mu g/cm^2$, n_t - number of moles for target nuclei and Q - Faraday cup charge expressed as nC . The values of the cross sections for production of different emitters are collected in the tables 3.3. These cross sections do not take into account Wien filter efficiency and geometric efficiency of the implantation detector.

3.2.3. Analysis of the reaction $^{54}Cr + ^{nat}Gd$, 4.698 MeV/u

In this reaction the target is made up of several isotopes of gadolinium. The most abundant are: $^{154}Gd(2\%)$, $^{155}Gd(15\%)$, $^{156}Gd(20\%)$, $^{157}Gd(16\%)$, $^{158}Gd(25\%)$ and $^{160}Gd(22\%)$. Thus there are also several possible compound nuclei as a result of the complete fusion processes with respective Gd isotopes. These nuclei are: ^{208}Ra , ^{209}Ra , ^{210}Ra , ^{211}Ra , ^{212}Ra , ^{214}Ra and they have mean excitation energy $E^* \approx 65$ MeV. As previously our objective is to identify radioactive evaporation residues, coming from the cooling process of compound nucleus, that are next registered by the implantation detector. Also in this analysis we will use the alpha decay chains technique to identify them. For cross section calculations we took the density of the target equal to $1300 \mu g/cm^2$ ($4.98 * 10^{18}$ nuclei/cm²) and the total dose of the beam nuclei $N_{beam} = 0.166 * 10^{16}$.

In the analysis only the alphas that deposited all their energy in the implantation detector were taken into account. The upper part of the right panel of fig. 3.7 presents the alpha energy spectrum for α particles with energy $E_\alpha > 5$ MeV. Those alpha particles are correlated in position, within a time window of 3600 s, with residues defined, similarly as for $Cr + Ho$ reaction, as those heavy ions that are in the contour "ER" on the plane E_{imp} vs T_{g1g2} . With the procedure exactly the same as in the reaction $^{54}Cr + ^{165}Ho$, 4 α -radioactive parent emitters that produce chains composed of two alphas were found. Cases of detected alpha decay chains for all identified emitters are presented in tables 3.4, A.9-A.11. As an example table 3.4

Table 3.4.: To find these chains α_2 was taken in the energy range [6.20, 6.33] MeV (fig. 3.7, upper right part). Chains are identified as a result of α -radioactive decay of $^{209}\text{Ra}/^{210}\text{Ra}$ nuclei. Reaction $\text{Cr} + \text{Gd}$.

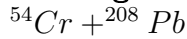
No.	E_{ion} (MeV)	$E_{\alpha 1}$ (MeV)	$E_{\alpha 2}$ (MeV)	$t_{ion} - t_{\alpha 1}$ (s)	$t_{\alpha 1} - t_{\alpha 2}$ (s)
1	18.58	6.94	6.22	2.44	475.98
2	14.82	7.00	6.23	22.12	836.71
3	11.23	7.00	6.25	4.53	279.67
4	13.85	6.98	6.26	0.31	113.46
5	11.40	6.95	6.26	2.82	169.12
6	16.05	7.06	6.29	0.17	59.69
7	17.48	7.01	6.31	0.76	194.35
8	19.07	7.04	6.32	8.47	306.16

presents registered α -decay chains from the decay of $^{209}\text{Ra}/^{210}\text{Ra}$. From those tables characteristics of each emitter were calculated: half-life times T_α and mean emission energy $\langle E_\alpha \rangle$. Next, comparing T_α and $\langle E_\alpha \rangle$ with the corresponding tabulated values of radioactive nuclei given in the nuclear chart, emitters were identified. In most cases two or three possible parent radioactive nuclei were found which can produce such chains: emission energies and life times very similar for different parent nuclei. Table 3.5 presents all the identified radioisotopes.

Table 3.5.: Characteristics of the four α emitters found in the analysis. Reaction $\text{Cr} + \text{Gd}$.

\bar{E}_{ion} (MeV)	$\bar{E}_{\alpha 1}$ (MeV)	$\bar{E}_{\alpha 2}$ (MeV)	$T_{\alpha 1}$ (s)	$T_{\alpha 2}$ (s)	Tab.	$^A Z$	σ (nb)
12.31	6.57	6.13	35_{-27}^{+224}	$15.9_{-12.3}^{+105.0} * 60$	A.9	^{203}Rn	0.12
15.31	7.00	6.27	$3.59_{-1.51}^{+3.09}$	$3.52_{-1.47}^{+2.89} * 60$	3.4	$^{209}\text{Ra}/^{210}\text{Ra}$	0.97
10.71	6.83	6.27	$2.33_{-1.8}^{+17.8}$	$45.6_{-35.3}^{+337.0}$	A.10	$^{206}\text{Fr}/^{205}\text{Fr}$	0.12
14.76	7.07	6.40	$3.04_{-1.4}^{+2.86}$	$51.3_{-23.4}^{+48.0}$	A.11	$^{208}\text{Ra}/^{204}\text{Fr}$	0.85

3.2.4. Seaborgium, element Z=106. Analysis of the reaction



Reaction $^{54}\text{Cr} + ^{208}\text{Pb}$ was measured at two bombarding energies $E_{\text{beam}} = 4.698$ and 4.750 MeV/u. Density of lead targets was $\rho_t = 440$ $\mu\text{g}/\text{cm}^2$ and 600 $\mu\text{g}/\text{cm}^2$ in the case of the last runs of 4.75 MeV/u. In the first case, the total dose of the Cr beam on the target was $N_{\text{beam}} = 2.71 * 10^{16}$ for the case of 4.698 MeV/u and for the second energy the dose was $N_{\text{beam}} = 2.47 * 10^{16}$ of Cr nuclei. Signals from all Si detectors: 8 localization (tunnel) detectors and position implantation detector were analyzed to identify alpha chains of Sg radioactive decay.

3. Superheavy elements production at GANIL

Table 3.6.: Two alpha chains identified as coming from decay of ^{261}Sg . Some of the α particles were also detected by tunnel detectors - these cases are given in parenthesis. Reaction $^{54}\text{Cr} + ^{208}\text{Pb}$, 4.698 MeV/u.

No.	E_{ion} (MeV)	$E_{\alpha 1}$ (MeV)	$E_{\alpha 2}$ (MeV)	$E_{\alpha 3}$ (MeV)	$t_{\text{ion}} - t_{\alpha 1}$ (s)	$t_{\alpha 1} - t_{\alpha 2}$ (s)	$t_{\alpha 2} - t_{\alpha 3}$ (s)
1	13.89	9.62	2.89 (escape)	-	0.169	11.87	-
2	14.41	2.37 (+5674ch)	2.46 (escape)	2.24 (+4113ch)	0.478	4.30	216.50

Table 3.7.: Main characteristics of alpha chain coming from the decay of ^{261}Sg . Some of the α particles were also detected by tunnel detectors - these cases are given in parenthesis. Reaction $^{54}\text{Cr} + ^{208}\text{Pb}$, 4.698 MeV/u. The first row presents measured values in this experiment while the second row cites values, for comparison, from the chart of the nuclides.

$\overline{E}_{\text{ion}}$ (MeV)	$\overline{E}_{\alpha 1}$ (MeV)	$\overline{E}_{\alpha 2}$ (MeV)	$\overline{E}_{\alpha 3}$ (MeV)	$T_{\alpha 1}$ (s)	$T_{\alpha 2}$ (s)	$T_{\alpha 3}$ (min.)	$^A Z$	σ (nb)
14.15	9.62	2.67 (escape)	2.24 (+tunnel)	$0.22^{+0.70}_{-0.15}$	$5.6^{+16.9}_{-3.8}$	$2.5^{+17}_{-1.9}$	^{261}Sg	58
-	9.56	8.77	8.01	0.23	4.3	1.7	^{261}Sg	-

3.2.4.1. Beam energy 4.698 MeV/u

Applying beam energy 4.698 MeV/u we discovered 2 cases of α chains which were identified as coming from the decay of ^{261}Sg . They are cited in table 3.6. For those two cases the mean characteristics were extracted and are given in table 3.7. In the table we also present values cited by the nuclide cart for the decay of A=261 isotope of seaborgium.

3.2.4.2. Beam energy 4.750 MeV/u.

At this energy we found eight cases of alpha chains from the decay of ^{261}Sg and one case of spontaneous fission of ^{260}Sg isotope. All of them are presented in table 3.8. Using data of that table mean values for energy and life times for each decay in the chain were calculated and are collected in table 3.9.

The observed fission especially life time for this decay is in good agreement with the hypothesis that this is spontaneous fission of isotope ^{260}Sg . In the case of alpha chains which were observed they are compatible with the hypothesis that they come from the decay of ^{261}Sg isotope. However there is small difference with the literature data for second α in decay chain. In two cases we observed these alphas with mean emission energy equal to 8.38 MeV (raw 1 and 5 of table 3.8) while ref. [18] shows energies for that second alpha equal to 8.94, 8.88, 8.77 and 8.72 MeV. One of possible explanation of this discrepancy is that we have registered α -decay of ^{257}Rf (Rutherfordium) to the excited collective state of ^{253}No (Nobelium).

Table 3.8.: Eight alpha chains identified as coming from the decay of ^{261}Sg . Some of the α /fission particles were also detected by tunnel detectors - these cases are given in parenthesis. Last row represents spontaneous fission of ^{260}Sg . Reaction $^{54}\text{Cr}+^{208}\text{Pb}$, 4.750 MeV/u.

No.	E_{ion} (MeV)	$E_{\alpha 1}$ (MeV)	$E_{\alpha 2}$ (MeV)	$E_{\alpha 3}$ (MeV)	$t_{\text{ion}}-t_{\alpha 1}$ (s)	$t_{\alpha 1}-t_{\alpha 2}$ (s)	$t_{\alpha 2}-t_{\alpha 3}$ (s)
1	14.74	9.57	8.40	-	0.303	18.14	-
2	14.29	2.01 (+4776ch)	1.67 (+4589ch)	1.89 (+5125ch)	0.290	32.13	4.18
3	13.04	9.62	3.41 (+2221ch)	-	0.009	2.31	-
4	13.90	9.50	8.81	-	0.022	11.61	-
5	14.35	9.52	8.36	-	0.649	3.69	-
6	14.91	9.54	1.59 (+2724ch)	2.51 (escape)	0.130	2.65	69.69
7	14.35	1.86 (+4327ch)	1.52 (+3363ch)	-	0.244	10.32	-
8	12.63	1.99 (+5961ch)	8.78	3.93 (+2200ch)	0.245	4.67	194.65
9	12.06	169.16 (+7558ch)	-	-	0.005	-	-

Table 3.9.: Characteristics of two radioactive emitters. One is α decaying ^{261}Sg nuclide (upper row) and the second is spontaneously fissioning ^{260}Sg (lower part). Some of the α /fission particles were also detected by tunnel detectors - these cases are given in parenthesis. Reaction $^{54}\text{Cr}+^{208}\text{Pb}$, 4.750 MeV/u.

\bar{E}_{ion} (MeV)	$\bar{E}_{\alpha 1/FF}$ (MeV)	$\bar{E}_{\alpha 2}$ (MeV)	$\bar{E}_{\alpha 3}$ (MeV)	$T_{\alpha 1}$ (s)	$T_{\alpha 1}$ (s)	$T_{\alpha 3}$ (s)	$^A Z$	σ (nb)
14.03	9.54	8.80, 8.38	2.78 (+tunnel)	$0.17^{+0.14}_{-0.07}$	$7.4^{+6.3}_{-3.1}$	$1.03^{+1.95}_{-0.6}$ *60	^{261}Sg	255
12.06	169.16 (+7558ch)			$3.5^{+23}_{-3.1}$ * 10^{-3}			^{260}Sg	32

3.2.5. Search for element Z=118

In July 1999 the BGS-Berkeley group [43] had announced the discovery of the new element Z=118. They claimed to observe 3 α -decay chains composed of 6 α 's each and all the characteristics, energies and emission times of alphas, for those events showed that each of those chains should start from the decay of the same element, namely Z=118. The reported cross section, ~ 2 pb, for that synthesis was much larger than expected. The same system studied with the SHIP velocity filter in Darmstadt [44] did not confirm the Berkeley results. As GANIL is able to deliver

3. Superheavy elements production at GANIL

the high intensity beam of ^{86}Kr ions ($15\ \mu\text{A}$ with charge state $10+$ what gives nearly 10^{13} particles/s) we decided, in view of the Darmstadt results, to repeat the same experiment. Our objective was to confirm (or not) the Berkeley's results. In the case of a positive verification of those results we planned to obtain additional information mainly:

- reach shorter decay times, by the use of fast electronics and two mode-trigger, for possible α -decay before the minimum time of $120\ \mu\text{s}$ in the Berkeley experiment,
- wait for very long decay times by the use of movable implantation detectors (see subsection 3.1.3: "Detection setup.") ,
- in order to increase transmission of the Wien filter compared to the GSI experiment the carbon stripper foils were put at a distance from the target three times larger than in the SHIP (GSI) experiment. ERs may be created in an isomeric state which decays via electron capture followed by an electron cascade with unknown half-lives modifying the ionic charge and thus reducing the filter transmission.

With the total accumulated dose of 1.1×10^{18} ions at $5.27\ \text{MeV}/u$ on targets of $300\ \mu\text{g}/\text{cm}^2$ we did not observe any event corresponding to the decay of element $Z=118$ ⁶.

This experiment had convinced us that all the detection setup: target system, Wien filter, time of light and silicon detectors as well as gas chambers are well suited for the study of low cross section heavy ion synthesis reactions with energy near the Coulomb barrier region. The experiment was conducted in collaboration with several French and foreign (Belgium, Brazil, Italy and Poland) laboratories.

3.2.6. Synthesis of hassium (Z=108) isotopes

For the synthesis of $Z=108$ nuclei the reaction $^{58}\text{Fe} + ^{208}\text{Pb}$ was chosen. The $^{58}\text{Fe}^{+8}$ beam with the average intensity of $500\ \text{nAp}$ and three different incident energies: 4.83 , 4.87 and $4.92\ \text{MeV}/u$ has irradiated Pb target of density $\rho = 420\ \mu\text{g}/\text{cm}^2$ sandwiched by 40 and $10\ \mu\text{g}/\text{cm}^2$ carbon support. The irradiation dose on the target was 2×10^{17} , 2.2×10^{17} , and 1.8×10^{17} ions for the mentioned incident energies. The whole experimental setup was very similar to the experiment for seaborgium synthesis.

Excitation energy imported to the compound nucleus in the fusion process is in the range $11-16\ \text{MeV}$ (the cold fusion). The residue nucleus should thus be produced by the emission of $1n$ or $2n$ neutrons. From that we expect to produce ^{265}Hs and/or ^{264}Hs . Identified in the experiment α -decay chains (SF decays) should have characteristics which are compatible with the decay of one of these isotopes. The expected decay chains for both isotopes are shown in fig. 3.10. From this we selected the most probable α/SF decay chains which can be populated by the decay of hassium 265 , 264 . Those chains are presented in tables 3.10, 3.11.

In table 3.12 are presented 8 α -decay chains registered for all three incident energies. All these chains are identified as coming from the decay of ^{265}Hs parent nucleus.

⁶ Recently Berkeley group has retracted [45] their results on the discovery of element $Z=118$.

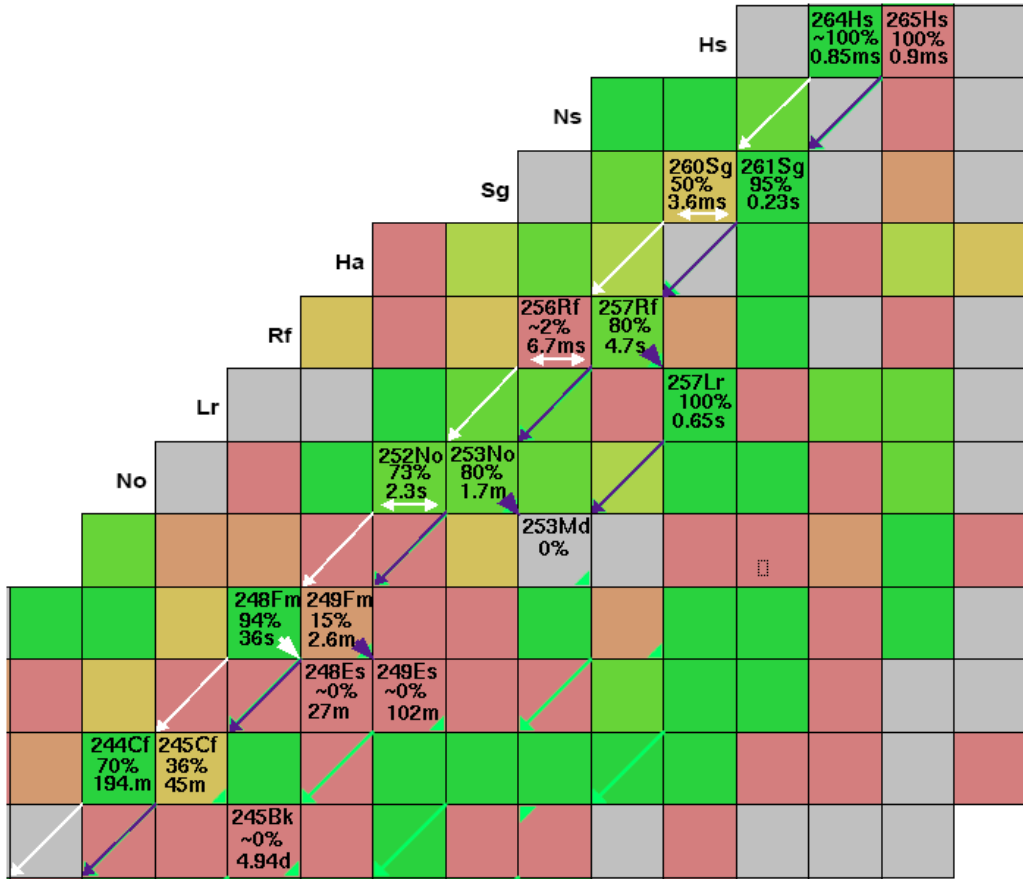


Figure 3.10.: Nuclides chart in the region of hassium isotopes. Here are marked decay paths of isotopes: ^{265}Hs and ^{264}Hs . Blue arrows represent consecutive daughter nuclei populated in the decay of hassium $A=265$, while white arrows indicate those nuclei that are produced by a decaying Hs of $A=264$. Long arrows represent α -decays, arrow-heads indicate β -decay while two head arrows are for spontaneous fission decays. There are also green arrows that represent decays characterized by the long half-lives ($>1\text{h}$). Based on this figure in table 3.10 the most probable α -decay chains produced by the radioactive decay of those two isotopes are summarized. For each nucleus produced on the decay path, literature branching ratio for α -decay and half-life of a nucleus is given.

3. Superheavy elements production at GANIL

Table 3.10.: The most probable, right part of the table, α -decay chains populated by the decay of the parent ^{265}Hs . Left part presents energies, E_α , of the emitted α 's in each chain and half-lives, $T_{1/2}$, of radioactive daughter-emitters (first column) in a chain. Bottom row shows the calculated, from fig. 3.10, probabilities that a given chain occurs on the decay path. Index m refers to the isomeric state of the hassium isotope. Chart of nuclides.

Emitter	E_α (MeV)	$T_{1/2}$	I	II	III	IV	V
^{265}Hs	10.57; 10.31 ^m	0.9; 1.55 ^m ms	α_1	α_1	α_1	α_1	α_1
^{261}Sg	9.56...9.47	0.23 s	α_2	α_2	α_2	α_2	α_2
^{257}Rf	9.013...8.55	4.7 s	α_3		α_3	α_3	α_3
^{257}Lr	8.86, 8.80	0.646 s		α'_3			
^{253}No	8.01	1.7 m			α_4	α_4	α_4
^{249}Fm	7.53	2.6 m				α_5	α_5
^{245}Cf	7.14, 7.08	45 m					α_6
Branch ratio			0.17	0.20	0.54	0.06	0.03

Table 3.11.: α -chains occurring on the possible decay paths of the radioactive ^{264}Hs . Each of those chains ends with a spontaneous fission (SF) as also marked in fig. 3.10. Chart of nuclides. The convention here is the same as in table 3.10.

Emitter	E_α (MeV)	$T_{1/2}$	1	2
^{264}Hs	10.43	$\cong 0.85$ ms	α_1	α_1
^{260}Sg	9.77, 9.72	3.6 ms	SF	α_2
^{256}Rf		6.7 ms		SF
Branch ratio			0.50	0.48

Table 3.12.: Characteristics of 8 identified cases of α chains coming from the decay of ^{265}Hs formed in the reaction $^{208}\text{Pb}(^{58}\text{Fe}, 1n)^{265}\text{Hs}$. For three incident energies 4.83, 4.87 and 4.92 MeV/u following cases (6) - (8), (1) - (3) and (4), (5) were observed correspondingly. The energy of the implanted residue, E_{res} , is given in italics. The upper indexes: I, II, III identifies appropriate α -decay chains of the table 3.10.

$E_{\text{res}}/E_{\alpha}$ (MeV)	t_{α} (s)	$E_{\text{res}}/E_{\alpha}$ (MeV)	t_{α} (s)	$E_{\text{res}}/E_{\alpha}$ (MeV)	t_{α} (s)	$E_{\text{res}}/E_{\alpha}$ (MeV)	t_{α} (s)
<i>15.49</i> ^(1,I)		<i>17.79</i> ^(2,I/II)		<i>16.14</i> ^(3,II)		<i>18.51</i> ^(4,I)	
10.28	5.55 *10 ⁻³	0.8+9.88	3.13 *10 ⁻³	10.31	5.15 *10 ⁻³	1.2(escape)	3.96 *10 ⁻³
9.03	0.79	0.7(escape)	0.24	missed		9.55	0.24
8.76	6.68	8.74	1.0	8.77	0.49	8.76	10.0
<i>15.26</i> ^(5,III)		<i>17.67</i> ^(6,III)		<i>16.02</i> ^(7,III)		<i>16.03</i> ^(8,I,II)	
10.56	1.48 *10 ⁻³	missed		0.95+9.51	0.80 *10 ⁻³	10.37	0.03 *10 ⁻³
9.52	0.07	9.55	0.18	1.3+7.92	0.18	9.45	0.04
8.49	0.45	8.47	6.18	missed		missed	
7.98	15.7	8.28	76.2	7.98	33.2		

In some cases we have not observed an expected emission of an alpha particle in the chain. They are marked as “missed” in the table. This is so in the case of chains: (3), (6), (7) and (8). There are two reasons that some alphas in the decay chain can be missed by the acquisition and the detector setup. As mentioned earlier, the dead time for the acquisition system was reduced to 30 μs . In the case of very short half-lives of an emitter and this is the case of ^{265}Hs that has a half-life of 0.9 and 1.55 ms it is possible that the α is emitted in the time range shorter than 30 μs and consequently is lost by the acquisition. This is the reason why we may not see the alpha emitted by the parent ^{265}Hs nuclide in the case of chain no (6). It may also happen that the alpha is emitted in the direction perpendicular to the surface of the implantation detector. In such a case the energy deposited by the emitted α particle in the detector is very close or even below the energy threshold for the detector, consequently we do not have an energy signal for such an event and such an alpha is also lost by the detection setup. The solid angle for such a direction of emission is quite large in this experiment, due to some non-functional tunnel detectors. This solid angle is around 10% of the full solid angle. This being considered and taking into account that for the 8 chains we have detected 25 alphas one can expect that on the average 2.5 alpha will be lost by the detector. We conclude that 3 other cases of “missed” alphas (tab. 3.12) can be explained by such an effect.

From the reference table 3.10 it is seen that the isotope of ^{265}Hs can give the origin, taking into account the most probable cases, for three different decay chains mainly I, II, III. To identify each of these chains in our data, one has to analysis the decay details of each of the 8 observed chains. As an example for chain no (1) from table 3.12 it is seen that the first alpha has energy and emission time which

3. Superheavy elements production at GANIL

are in good agreement with the decay of ^{265}Hs as one can see from reference table 3.10. The second and the third alpha of that chain have emission times and energies that are compatible with energies and half-life of the nuclides ^{261}Sg and ^{257}Rf correspondingly. So this chain was identified as chain I from table 3.10. Similarly the other α -chains from table 3.12 were identified and are marked by upper indexes.

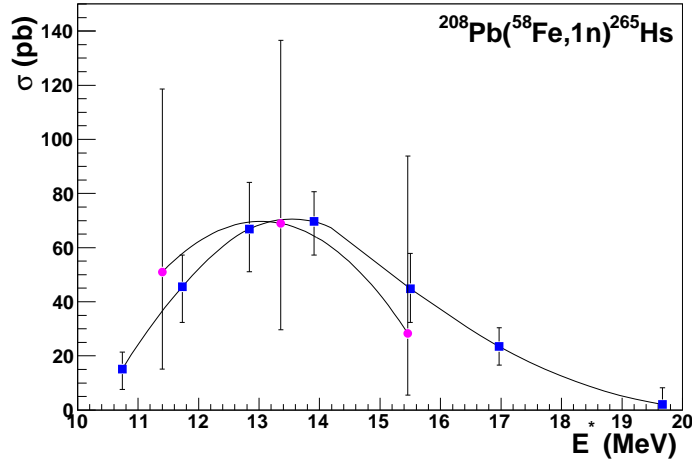


Figure 3.11.: Excitation function for the reaction $^{208}\text{Pb}(^{58}\text{Fe}, 1n)^{265}\text{Hs}$ [46]. Two sets of experimental data are plotted. Full circles represent this experiment and full squares are the data from the GSI for the same reaction and similar range of excitation energies. The error bars represent the statistical uncertainties with 60% of confidence level. Lines are to guide the eye.

Table 3.13.: Kinetic energies of α 's and half-life times of emitters from the α -radioactive decay chain of ^{265}Hs (columns 2 and 3) and ^{261}Sg (columns 4 and 5). Radionuclides: ^{265}Hs and ^{261}Sg were produced in the fusion reactions: $^{58}\text{Fe} + ^{208}\text{Pb}$ and $^{54}\text{Cr} + ^{208}\text{Pb}$, respectively. It is seen that both α -decay chains have common daughter nucleus emitters that have very similar characteristics. Results are deduced from the tables: 3.6, 3.8 and 3.12 of our measurements.

Emitter	E_α (MeV)	$T_{1/2}$	E_α (MeV)	$T_{1/2}$
^{265}Hs	10.56; 10.32 ^m	1.02; 2.48 ^m ms		
^{261}Sg	9.54, 9.45, 9.03	0.17 s	9.56	0.18 s
^{257}Rf	8.76, 8.48	4.0 s	8.80, 8.38	7.0 s
^{257}Lr	8.76	0.52 s		
^{253}No	8.28, 7.98	0.5 m	-	1.4 m

To compare our results with data received previously by the GSI group [47] for the same reaction, in fig. 3.11 we plotted the ER, 1n channel excitation function assuming that the total efficiency for the experimental detection setup⁷ is

⁷this includes: opening of 15 mrad of the Wien filter window, efficiency of the Wien filter trans-

17% and excitation energy of the compound nucleus in the mid-target is equal to $E^* = 11.4, 13.3, 15.5 \text{ MeV}$. From the figure one sees that both experiments are in agreement and there is no reason to suspect a problem with the beam energy calibration (such a problem was reported elsewhere a few times).

It should be also noticed that isotopes: ^{265}Hs and ^{261}Sg produced in two different fusion reactions have common α emitters that have the same characteristics (see tab. 3.13).

3.2.7. Search for element Z=114

In the beginning of the year 2003 the latest element produced and identified unambiguously by the cold fusion method was Z=112. This element was synthesized in the reaction $^{70}\text{Zn} + ^{208}\text{Pb}$ that was studied in the GSI in 1996 [9]. The next step regarding this method was to observe new elements via the reactions $^{209}\text{Bi}(^{70}\text{Zn}, 1n)^{278}113$ or $^{208}\text{Pb}(^{76}\text{Ge}, 1n)^{283}114$. Thanks to the development of high intensity ^{76}Ge beams at GANIL the last reaction was decided to be studied by the FULIS collaboration in autumn 2003. To realize this objective a three step program was undertaken:

- checking the entire setup especially the Wien filter transmission,
- measuring the cross section at the level of tens of pico barns,
- performing the reaction $^{208}\text{Pb}(^{76}\text{Ge}, 1n)^{283}114$.

The experimental setup was the same as described previously except for the targets. Lead targets and carbon strippers were made at GANIL using the evaporation technique developed by the target laboratory of GSI. The rotating wheels were equipped with 18 Pb targets instead of 36 Pb . The targets had a surface area of $11 \times 1.5 \text{ cm}^2$ while strippers foils dimensions were $11 \times 2.5 \text{ cm}^2$.

3.2.7.1. Transmission efficiency of the Wien filter

One of the key parameters of the Wien filter is its transmission efficiency. This parameter decides what percentage of nuclei created in the fusion process will reach the detection system and will be implanted in the position sensitive silicon detector. In order to measure this transmission efficiency a beam of ^{208}Pb nuclei extracted from the first cyclotron CSS1 with the energy corresponding to the energy of residues $^{283}114$, produced in the reaction $^{76}\text{Ge} + ^{208}\text{Pb}$ was directed to the Pb targets, the same which were used in the experiment. Nuclei of the Pb beam were then scattered in the target and part of them entered the Wien filter. The intensity of the scattered beam was measured before and after the Wien filter, in place of detection. From that transmission efficiency was deduced to be equal to 17%. This value is in good agreement with a previously assumed transmission efficiency for the synthesis of Z=106 and 108 experiment. To increase acceptance of the Wien filter it has been decided to move targets as close as possible to the entrance of the filter. Following this modification, the transmission efficiency measured with the same method reached a value of 27%.

mission and geometric efficiency of the BEST (implantation + tunnel) silicon detector.

3. Superheavy elements production at GANIL

3.2.7.2. Cross section of pico barn region

To prove that the cross section sensitivity of the detection system is in the pico barn region and as a second step of the program, the experiment searching for $Z=108$ isotopes was performed. The experiment, described earlier, has shown that the experimental setup can easily reach sensitivity on the level of 30 pb .

3.2.7.3. Results

The search for isotopes of $Z=114$ element began in October 2003. The beam of $^{76}\text{Ge}^{+10}$ with an intensity $0.8 \text{ p}\mu\text{A}$ and an energy 5.02 MeV/u was irradiating ^{208}Pb targets of $420 \text{ }\mu\text{g/cm}^2$ thickness. The energy range in the center of the mass was 274.5 to 278.5 MeV . The rejection factor of the primary beam and the scattered particles was reached at the level of 10^{11} . During three weeks of experiment, the total dose accumulated on the targets was $5 * 10^{18}$ lead ions. No events attributed to the isotope $^{283}114$ was observed what implies cross section for creation of $Z=114$ in this reaction smaller than 1.2 pb .

3.2.8. Inverse kinematics experiments

In 2001, the FULIS collaboration proposed a new experimental approach to the production of superheavy elements. The idea was to use inverse kinematics reactions i.e. reactions for which the projectile nucleus is heavier than the target nucleus, to create new isotopes of very heavy elements. Similarly to the standard method, one of the partners in the synthesis process, due to its double magic structure, is ^{208}Pb element (now it is a beam nucleus) while the other lighter partner (target nucleus) is chosen to match the intended product of the synthesis. The approach was accepted by the GANIL scientific committee and approved as the experiment E339b. To test the method, we decided to synthesize elements $Z=88, 90$ using reactions $^{208}\text{Pb} + ^{12}\text{C}$, ^{18}O and possibly $Z=105, 106$ via $^{208}\text{Pb} + ^{51}\text{V}$, ^{54}Cr reactions. A detailed description of the experiment and the results can be found in ref. [48]. Here I will only present the main aspects concerning the synthesis techniques in inverse kinematics.

Comparing to the normal kinematics reactions, where the same combination of reacting nuclei is used as in the inverse kinematics case, the method has several advantages (assets) and only one drawback.

Drawback:

- The velocity difference between the beam and the evaporation residues is much smaller what implies the necessity to apply much stronger magnetic and electric field in the Wien filter of LISE3.

Assets:

- The ERs have a much larger velocity than the same ERs produced in the synthesis reaction by normal kinematics, and in consequence are strongly focused at forward angles what ensures a much better transmission through the velocity filter, even in the case of α/p emission in the target or its α -decay in flight. What is more, a drastic decrease of the complete fusion cross section with Z_{CN} could be accompanied by the onset of the incomplete fusion or pre-compound

emission of a few nucleons [49]. In that case, corresponding ERs will be emitted from the target with a much broader angular range, but here (inverse kinematics) strong forward focusing ensures, they will be still efficiently transmitted through the Wien filter.

- In normal kinematics the target thickness is limited by multiple scattering: above the thickness of 300-400 $\mu\text{g}/\text{cm}^2$, what corresponds to an excitation energy range $\Delta E^* = 2 - 3 \text{ MeV}$, the angular spread of the ER due to multiple scattering in the target material and stripper foils is approximately the angular acceptance of the LISE3. A thicker target increases only the background in the implantation detector without an increase of the counting rate of ERs. For the same reaction, but in inverse kinematics, the velocity of the ER is larger, the target mass is smaller, thus a much larger thicknesses can be used, what corresponds to the increase of the ΔE^* range, up to 15 MeV . The excitation functions of 1n, 2n evaporation channels are Gaussian in shape with FWHM around 5 MeV . This has two consequences: a) when the excitation function is known, a target thickness ensuring $\Delta E^* = 10 \text{ MeV}$ range allows us to achieve the maximum counting rate of ERs, b) for a synthesis of an unknown nucleus the incident (optimal) beam energy has to be calculated from the theoretical binding energy of Z_{CN} . Several tables present mass values which may differ by several MeV [50]. Therefore, a range of $\Delta E^* \sim 15 \text{ MeV}$ has to be covered. For normal kinematics this implies that several incident energies have to be used, e.g. 6 energies were used in an attempt to produce element $Z=116$ via $^{82}\text{Se} + ^{208}\text{Pb}$ [6]. In inverse kinematics, one can save time by using only one energy and the target thickness corresponding to $\Delta E^* \sim 15 \text{ MeV}$.
- The ionic charge state distributions of superheavy nuclei are estimated by extrapolating measurements made for nuclei up to $Z=92$. Different empirical extrapolations give different values [51, 52, 53, 54], but they differ less for ERs produced in inverse kinematics as the ERs have larger velocities for which more measurements are available and the variation with energy is weaker.
- Energy deposited, in the identification detector system, by an implanted ER is large. This is important to obtain an estimate of the ER mass via E vs. time of flight method. For that, the calibration with the Pb beam of the same velocity as ER has to be performed to take into account the pulse height defect.
- Due to the deeper implantation of the ER in the X-Y silicon detector, the efficiency for the full stopping of α particles from the decay chains is increasing, thus reducing the number of “escaping” α ’s from the silicon detector. Furthermore, in the case of spontaneous fission, both fragments are stopped, depositing all their energy in the implantation (silicon) detector which means that the total kinetic energy (TKE) can be measured with better accuracy and with 100 % efficiency.
- For many systems the light partner material has a much higher melting temperature than the heavy one (especially Pb and Bi) or even the lighter beam is not available. Inverse kinematics enlarges the number of projectile-target combinations, some of them are listed in table 3.14, that can be used in the reaction of synthesis.

3. Superheavy elements production at GANIL

- ER produced in the inverse kinematics synthesis has a high enough kinetic energy (typically 2.5-3 MeV/u , while in normal kinematics energy of ER is only of the order of 0.5 MeV/u) allowing to install additional transmission detectors in the experimental setup and in this way receive more complete physical information on the detected ER. Even if this information is redundant it is still valuable for the unambiguous identification of the ER.

In experiment E339b an important modification was performed in the velocity filter setup. To reduce the background due to scattering of the deflected beam ions on the upper plate of the filter, this plate was moved to the distance of 7 cm (in standard configuration this distance is 5 cm) with respect to the beam axis.

Table 3.14.: Reactions with ^{208}Pb . Above 112 (italic), new isotopes and new elements. First column, atomic number of the compound nucleus; third column, atomic mass of the compound nucleus; fourth column, reaction Q -value; fifth column, Bass barrier; sixth column, excitation energy at the Bass barrier; seventh column, incident energy (MeV/u) which leads to a 13 MeV excitation energy in the compound nucleus [55].

Z_{CN}	Target	A_{CN}	$-Q$ (MeV)	V_{Bass} (MeV)	E^*_{Bass} (MeV)	E_{beam} ($A.MeV$)
104	$^{50}_{22}Ti$	258	169.1	192.1	23.0	4.52
105	$^{51}_{23}V$	259	175.3	200.9	25.6	4.60
106	$^{54}_{24}Cr$	262	186.4	208.4	22.0	4.65
107	$^{55}_{25}Mn$	263	193.2	217.1	23.9	4.74
108	$^{58}_{26}Fe$	266	203.1	224.6	21.3	4.76
109	$^{59}_{27}Co$	267	210.5	233.3	22.8	4.86
110	$^{64}_{28}Ni$	272	221.9	239.4	17.5	4.80
111	$^{65}_{29}Cu$	273	228.5	248.0	19.5	4.88
112	$^{70}_{30}Zn$	278	242.1	254.1	12.0	4.87
<i>113</i>	<i>$^{71}_{31}Ga$</i>	<i>279</i>	<i>249.7</i>	<i>262.7</i>	<i>13.0</i>	<i>4.96</i>
<i>114</i>	<i>$^{76}_{32}Ge$</i>	<i>284</i>	<i>260.0</i>	<i>269.0</i>	<i>9.0</i>	<i>4.90</i>
<i>115</i>	<i>$^{75}_{33}As$</i>	<i>283</i>	<i>265.1</i>	<i>278.5</i>	<i>13.4</i>	<i>5.05</i>
<i>116</i>	<i>$^{82}_{34}Se$</i>	<i>290</i>	<i>280.4</i>	<i>283.0</i>	<i>2.6</i>	<i>4.99</i>
<i>117</i>	<i>$^{81}_{35}Br$</i>	<i>289</i>	<i>286.0</i>	<i>292.9</i>	<i>6.9</i>	<i>5.13</i>

A second modification was applied to the detector setup. An additional detector was installed. Here it was a thin ΔE ionization chamber built in Krakow (see fig. 3.12 for a detailed view of the detector placement in the experimental setup). The analysis of the data acquired by means of this detector allows to conclude that a detector which measures energy loss of heavy ion can be a useful element in the identification process of very heavy ERs (ref. 3.12).

The results of the experiment for fusion reactions $^{208}Pb + ^{12}C$, ^{18}O convinced us that the method (inverse kinematics) could be applied to superheavy element production. Unfortunately due to the technical problems with high voltage on the

Wien filter it was not possible to measure the synthesis of heavier elements, as we earlier planned, namely reactions $^{208}\text{Pb} + ^{51}\text{V}$, ^{54}Cr .

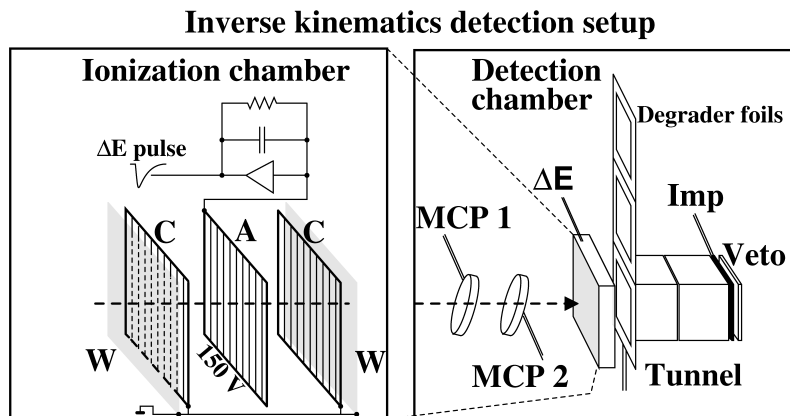


Figure 3.12.: Schematic view (left panel) of the ionization, transmission chamber and its location in the detection setup (right panel). The role of the transmission chamber is to measure energy loss (ΔE) of the heavy residue that next implants in the silicon position detector (Imp) where its radioactivity is detected.

In perspective, this new techniques can be used to receive additional information on superheavy nuclei. For this several points can be studied: new projectile-target combinations (i.e. new paths leading to known isotopes), detailed decay characteristics of isotopes produced with a sufficient cross section, new isotopes of known elements and new elements. Table 3.14 presents, experimentally accessible, target-projectile combinations that can be used in the synthesis study of the SHE nuclei.

3.3. Gas-scintillation detector for SHE studies

The main method of identification of superheavy elements relies on the detection of α/SF decay chains from the SHE implanted in the Si detector. The essential point of that method is the way alpha particles are identified. Usually it is required that the signal in the implantation detector is in anti-coincidence with the time of flight system (ToF). In cases when the background is small the method works well. For larger background, especially when it is composed of other light particles (e.g. protons), such a definition of registered alpha decays can not be sufficient, because background protons can produce a signal in the implantation detector which is also in anti-coincidence with the ToF system. In effect these protons mimic alpha decays.

In order to obtain a more effective identification of SHE elements and a more precise definition of alpha decays we propose to use a new type of gas-scintillation chamber⁸. It detects scintillations produced by the heavy ion passing through a gas medium. It also has tracking capabilities that help to determine the trajectory of the particle entering/escaping the implantation detector. Other main characteristics of that chamber are: 4π geometry (it will be mounted close to the implantation detector), detection of light charged particles and spontaneous fission fragments.

⁸ At address <http://twin.if.uj.edu.pl/gallery/thumbnails/1.html> one can find photos of the chamber.

3. Superheavy elements production at GANIL

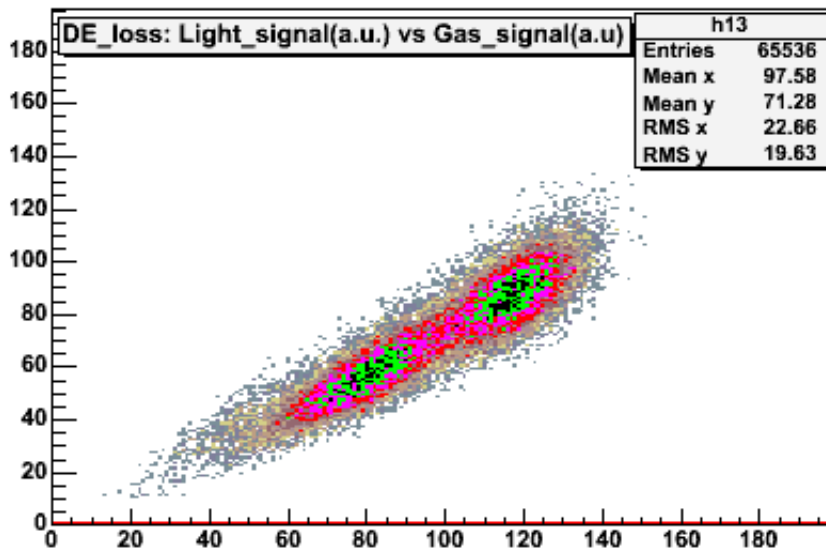


Figure 3.13.: Energy loss (DE_loss) of fission fragments (Cf source) detected in the gas-scintillation counter. Vertical and horizontal axes represent DE_loss given by the scintillation signal and the gas signal, respectively. Two groups of events correspond to the asymmetric fission of the Cf source. Gas pressure in the detector is 50 mbar, the voltage between anode and cathode is 200 V. [56].

Our idea is to have a detection system that will possess good timing and spectroscopic features. Good timing properties are necessary for time of light measurements of an implanted heavy residue while good spectroscopic properties are needed to measure energy and to identify detected particles. Fast pulses we plan to obtain from the scintillations of the gaseous part of the detector. The first tests performed in collaboration with LPC-ISMRA Caen gave promising results (see fig. 3.13). In order to measure energy and trajectory we want to equip this detector with several wire planes. As the gaseous part of the detector will be working in the proportional regime one should also be able to obtain good spectroscopic information for light particles.

Dedicated electronics: preamplifiers, amplifiers and summation logic, required for that detection system is presently built in our laboratory. The prototype modules were already successfully tested in the LPC-ISMRA.

The chamber will be mounted, together with implantation position sensitive detector and tunnel detectors, in the detection setup working in GANIL. An integral part of the system will be the software for on-line alpha chains and fission fragments identification (this part is already working in superheavy experiments in GANIL) and the software for the reconstruction of the heavy and light ions trajectories.

3.4. Summary and future of the *FULIS* collaboration experiments

FULIS collaboration between 1999 to 2003 has accomplished four experiments aimed at the production of superheavy elements. In these campaigns the following main reactions were studied: (1) $Kr + Pb \rightarrow Z = 118$, (2) $Cr + Pb \rightarrow Z = 106$, (3) $Fe + Pb \rightarrow Z = 108$, (4) $Ge + Pb \rightarrow Z = 114$ and inverse kinematics reactions: (1i) $Pb + O$, (2i) $Pb + C$. We received convincing data for the synthesis of elements $Z=106$, and $Z=108$ and negative results for the creation of elements $Z=118$, $Z=114$. Our negative result for $Z=118$ did not confirm the discovery of this element for the same reaction as was announced by another group [43]. Also other laboratories [44] could not confirm the Berkeley group discovery. For the $Z=114$ case we could estimate the upper cross section limit for the creation of such an element. A summary of the results is given in table 3.15.

Table 3.15.: Summary of the reactions studied by the *FULIS* collaboration. In the forth column number of identified α -decay chains are given for beam energies listed in column 2. For isotope ^{260}Sg , created at Pb ions energy $4.75 MeV/u$, one spontaneous fission (*SF*) event was observed.

Reaction	Energy (<i>MeV/u</i>)	<I> ($p\mu A$)	Chains	Rejection	σ (<i>pb</i>)
$^{208}Pb(^{86}Kr, 1n)^{293}118$	5.27	2	0	10^8-10^{10}	<1
$^{208}Pb(^{54}Cr, 1n/SF)^{261/260}Sg$	4.70, 4.75	0.04	2,8	$>1.7*10^{10}$	590
$^{18}O(^{208}Pb, xn)^{226-x}Th$	5.00			10^6-10^8	2400
$^{208}Pb(^{58}Fe, 1n)^{265}Hs$	4.83, 4.87, 4.92	0.5	3,3,2	$>2*10^{10}$	50- 70
$^{208}Pb(^{76}Ge, 1n)^{283}114$	5.02	0.8	0	$>10^{11}$	<1.2

Collaboration *FULIS* plans to study new input reaction channels as a path to the synthesis of SHE. These will be reactions with symmetric systems where the atomic numbers for both partners of reaction are very similar. As a good starting point for such studies we chose $^{136}Xe + ^{122,124}Sn$ reaction at beam energy $4.8 MeV/u$. The experiment was planned for 2007. The Krakow group has constructed a dedicated gas-scintillation detector which will be one of the main detection components of the experimental setup. This detector was described in the previous section and presently is tested in the Hot Matter Department of Physics in the M. Smoluchowski Institute of Physics.

A new approach to the SHE studies is offered by the *SPIRAL2* project started lately at *GANIL*. *SPIRAL2* will provide high intensity neutron reach beams and a unique opportunity to study superheavy elements beyond the presently accessible beam-target combinations. For example beams of $^{88-93}Kr$ and $^{137-141}Xe$ will be available compared to the $^{84-86}Kr$ and ^{136}Xe beams accessible now. Fusion reactions with such neutron reach beams and different targets will allow to study a whole spectrum of new SH isotopes as heavy as *Hs*. In this way an extended systematic of SHE properties can be received. The reactions with *Kr* beams will be quite different

3. Superheavy elements production at GANIL

from the standard fusion reactions based on the lead and actinide targets. One can mention their main features:

- the high mass symmetry for the projectile/target system, equal to first order to the value $Z_p^* Z_t$,

- the number of neutrons in the nuclei is linked to the structure of the nuclei.

These two features are known to play an important role in the formation of heavy evaporation residue but no model can so far predict, in a reasonable way, the cross sections for the formation of SHE. Because such study will not be possible for the heaviest systems due to too low cross sections for their formation the first step will be to study lighter SHE production. One of the possibilities is to study *U* and *Pu* isotopes produced with *Kr* neutron rich beams. The advantage of those symmetric reactions is that one can reach a different isotopes region than in the asymmetric ones. Such study will also give additional information on the influence of the mass asymmetry parameter and the number of neutrons on the formation of the SHE systems.

4. Radioactive decays, low statistics case

The main identification method of newly created SHE elements, as was shown in the previous chapters, is based on the detection of α/SF decay chains produced by the radioactivity of those elements. Particularly, the energy and emission time of alpha particles for each registered set of the decay chain is measured. It is of great importance for the proper identification of the new elements and for models predicting properties of these nuclides, to estimate the precision with which are measured the energy of alphas and mean life times (τ_i) of consecutive daughters nuclei. What concerns the energy precision is mainly restricted by the quality of the implantation silicon detector of the detection setup. On the other hand, the precision of the mean life time measurements is dictated by the statistical nature of the decay process, governed by a well-known exponential decay law, and in principle depends not very much on the experimental setup¹, except for short lived elements that have τ comparable with the dead time of the acquisition systems which is typically in the 30-150 μs range. Thus statistical methods are used to calculate the uncertainties (errors) for measured τ_i . However, in the case of low counting statistics for interesting events, as it is for SHE studies, and the inherent background of the measurement, special statistical methods have to be developed for the mean life time error estimation. What is more, the radioactive decay law can deliver means to cross check discoveries in the field of SHE nuclei. The next two sections present these subjects.

4.1. Calculation of statistical errors for measured half-life times

In the previously analyzed reactions, the mean or half-life ($T_{1/2}$) time for each identified radioactive nucleus was assigned from a small number of registered alpha decay chains. In order for the measured τ to be meaningful and comparable with other data one should estimate an error associated to this mean life time. In our case, standard statistical formulas used to calculate such errors, due to very low statistics can not be applied here, typically a few and sometimes only one or two cases of alpha decay chains are available. The other method, of course based on the known decay law, has to be employed. Here we use the concept of conditional probability distribution.

Suppose one registers N cases of the decay chains initiated by nuclei X . Let each chain have the identical emission pattern, i.e. the same daughter nucleus, grand-daughter nucleus etc. in the decaying sequence, and the pattern is composed of k

¹ Clocks for tagging detection times of particles have often resolution $\sim 10 \mu s$. This is usually much smaller than the mean life time of searched element.

4. Radioactive decays, low statistics case

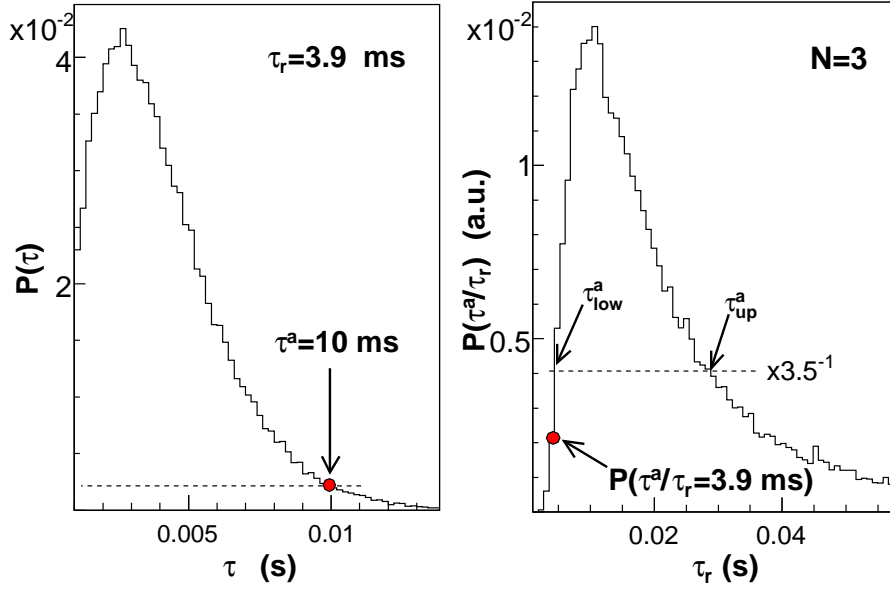


Figure 4.1.: Illustration of the procedure for the statistical error estimate of the measured mean decay time (τ) of a radioactive specie a . One assumes $N = 3$ alpha decay events are registered and the measured mean decay time of those events is $\tau^a = 10$ ms. In the left panel, probability distribution of τ ($P(\tau)$) for a case when the true mean life time of a specie a , $\tau_r = 3.9$ ms is considered. Right panel presents complete conditional probability distribution function $P(\tau^a/\tau_r)$ for occurrence in the measurement $\tau = \tau^a = 10$ ms, when the true τ_r is unknown. For details of that procedure see text.

alphas: $\alpha_1^j, \alpha_2^j, \dots, \alpha_k^j$ ($j = 1, \dots, N$). Having measured time tags for implanted heavy residue, t_0 , and detected alphas, t_i^j ($i = 1, \dots, k$), one can get estimator of half-lives, $T_{1/2}^1, \dots, T_{1/2}^k$, of each of k nuclei in the decay sequence. The formula is straightforward: $\tau_i = \frac{1}{N} \sum_{j=1}^N (t_{i-1}^j - t_i^j)$ and $T_{i,1/2} = \tau_i \ln 2$. Due to the statistical nature of the decay process and the finite number N of alpha events in a sample, τ_i only approximates true mean life time ($\tau_{i,r}$) of the radioactive specie i .

In order for the τ_i to be useful a reasonable estimation of an error associated with the τ_i has to be given. As it will be shown in the next few paragraphs the conditional probability $P(\tau_i/\tau_{i,r})$ i.e. probability one will measure mean life time equal to τ_i for nucleus i if its true value is $\tau_{i,r}$, can be applied to calculate reasonably such a (statistical) error. The main difficulty is to calculate the form of this conditional probability, here we use the Monte Carlo method.

The main idea is presented in fig. 4.1. To simplify considerations and to omit index i from the previous formulas, let us concentrate on the first alpha decay in the chain. Further, as in the figure, we will consider the specific measurement: the decay of nuclei a for which $N = 3$ alpha decay events were registered and the mean decay time calculated of those three events is $\tau^a = 10$ ms. Suppose, left panel of the figure, that the decaying nucleus has true $\tau_r = 3.9$ ms.

Now, one may question what is the probability, $P(\tau^a)$, that in other experiments with the same decaying specie and $N = 3$ observed α -decay events one gets $\tau = \tau^a =$

4.1. Calculation of statistical errors for measured half-life times

Table 4.1.: Coefficients for statistical error estimation of the half-life times of radioactive nuclides in a case when N decays are detected. Confidence levels for corresponding errors of $T_{1/2}$ marked in the table as “Prob.” are also presented. Errors of half-life times are calculated as: $T_{1/2}^{+K_{up}T_{1/2}-K_{low}T_{1/2}}$.

N	1	2	3	4	5	6	7	8	9	10	20
K_{up}	6.25	2.81	1.85	1.41	1.08	0.90	0.88	0.86	0.80	0.72	0.45
K_{low}	0.72	0.64	0.56	0.51	0.47	0.46	0.45	0.44	0.42	0.41	0.30
Prob.	$\simeq 0.5$	0.65	0.75	0.78	0.82	0.83	0.84	0.84	0.85	0.85	0.87

10 *ms*. The question is easy to answer with the aid of the Monte Carlo method.

We know that the decay of the specie is governed by exponential law and its true mean life time is $\tau_r = 3.9$ *ms*. Using this information one can simulate $N = 3$ decays of the nucleus and from those decay events the mean life time τ is calculated. The procedure is repeated many (10^5) times, in consequence the complete probability distribution function $P(\tau)$ is received. The function is shown in the left panel of the figure while the arrow marks $P(\tau^a)$ i.e. probability that from the measurement we get $\tau^a = 10$ *ms*. Such an algorithm should be repeated for all τ_r from 0 to infinity. In practice it is enough to repeat the calculations for $\tau_r = 0.1\tau^a - 20\tau^a$. Finally, we obtain the conditional density probability $P(\tau^a/\tau_r)$ as shown in the right part of the figure. We marked, here, also the value of the conditional probability assigned from the case when $\tau_r = 3.9$ *ms*, red circles on both panels. The maximum of $P(\tau^a/\tau_r)$ function is for $\tau_r = \tau^a$. Setting the level of the accepted range of true mean life times τ_r at a value 3.5 times (little arbitrary choice) smaller than the maximum value of $P(\tau^a/\tau_r)$ one gets the upper limit and lower limit error estimation of τ^a as $+(\tau_{up} - \tau^a)$ and $-(\tau^a - \tau_{low})$, respectively. Finally, for the above example one gets $\tau^a = 10_{-8.1}^{+26.7}$ *ms*. The confidence level can also be given for that error, here it is 0.75.

Although the example was given for $\tau^a = 10$ *ms*, it is easy to show that the conditional distribution function and the upper, lower errors can be rescaled to the universal form for all values of measured τ^a . The scaling factor is $+(\tau_{up} - \tau^a)/\tau^a$ for the upper limit error and $-(\tau^a - \tau_{low})/\tau^a$ for the lower limit error. Generally, for the case $N = 3$ one can write $\tau_{-0.81\tau}^{+2.67\tau}$.

Exactly the same procedure was applied for other numbers (N) of registered decays. When N is decreasing the $P(\tau^a/\tau_r)$ function (fig. 4.1) becomes more asymmetric and its shape broadens while for increasing N , function becomes narrower and approaches the Gaussian distribution as is expected from the Central Limit Theorem. The rescaled, upper and lower limit errors together with the confidence level in the case of $N = 1 - 10, 20$ are collected in table 4.1. Because literature cites half-life time of radioactive nuclei rather than their mean life times our table also presents errors for the $T_{1/2}$. It is interesting to note that even in the case of one detected α -decay it is possible to estimate an error of the measured half-life time of a nuclide. From the table it is also seen that (statistical) errors of measured $T_{1/2}$ strongly depend on the number (N) of detected alpha decays especially when $N = 1 - 4$. When N reaches large values, $N > 20$, usually variance is taken for statistical error estimation of mean life times of nuclides. In our estimation method of accepted ranges

4. Radioactive decays, low statistics case

of τ , the confidence level varies with N . This is the inconvenience of the proposed procedure, but on the other hand the number of N 's is small and it is relatively easy to remember the value of the confidence level for each N especially if one needs to know the value of the confidence level with a few percents accuracy.

4.2. Consistency of α -radioactive decays

When one observes radioactive decays of new superheavy elements it is of primary importance whether the data are compatible with the assumption that the measured time decay values originate from the decay of a single species - the same nuclide. A new method to check/validate such a compatibility was proposed in reference [57] and it is especially useful in the case of low counting statistics which is the case in the area of SHE studies. The method is based on the second moment of the logarithmic decay-time distribution. In the next paragraphs I will describe it in more details.

The decay of a radioactive nucleus is governed by the constant probability per unit time $dP/dt = \lambda$. Starting from the specific number of initial nuclei n_0 and assuming that each nucleus decays independently, one arrives at the conclusion that the number of remaining nuclei, $n(t)$, decreases gradually in time, t , according to the formula:

$$\frac{dn}{dt} = \lambda n(t), \quad (4.1)$$

from which one receives the well-known exponential law for the radioactive decay of one species of nuclei:

$$n(t) = n_0 \exp(-\lambda t). \quad (4.2)$$

Thus the number of decay events per unit time is given by:

$$\left| \frac{dn}{dt} \right| = \lambda n_0 \exp(-\lambda t). \quad (4.3)$$

In an experiment the times t_1, t_2, \dots, t_n of individual radioactive decays represent a sample of the density distribution given by eq. 4.3. The sample is subjected to statistical fluctuations. Standard statistical analysis tools have means to estimate the decay constant λ . However this task can be complicated by several factors:

- radioactive decay can only be observed in the limited time range, above the lower threshold t_{min} and below the upper threshold t_{max} ,
- events of another species which decay, usually with different time constant or background events appearing with a constant rate can be mixed in,
- additionally the situation can be complicated by the fact that a daughter nucleus, produced in the decay, may also be radioactive.

The first moment of the density distribution 4.3 is $\langle t \rangle = 1/\lambda$. The average of the measured decay times is thus an estimator of that quantity:

$$\langle t_{exp} \rangle = \frac{\sum_{i=1}^n t_i}{n} \quad (4.4)$$

However, the following conditions has to be fulfilled in order if eq. 4.4 is to be a good estimator of the inverse of λ :

1. the full time range has to be covered by the measurement e.g. t_{min} should be very small and t_{max} should be very large compared to $1/\lambda$,
2. a contribution form other radioactive species and a background has to be excluded.

With these conditions satisfied $\langle t_{exp} \rangle$ gives a good estimation of the decay constant also in the case of low statistics.

In principle the second moment of the density distribution function can be used to test the compatibility of the data with a radioactive decay of a single species. However the second moment strongly depends on the decay constant which can be only roughly evaluated in the case of low statistics.

In the conventional analysis of the radioactive decay the individual decay times are sorted into spectrum with time intervals of the constant width: Δt . This means that the channel m contains the number of events observed in the time interval: t_m and $t_m + \Delta t$. The shape of such a distribution is equal to the density distribution function from eq. 4.3:

$$\frac{\Delta n}{\Delta t} \approx \frac{dn}{dt} \quad (4.5)$$

Of course this spectrum has an exponential shape and when plotted in the logarithmic scale in t , it will follow the straight line. Using the fitting procedure (e.g. least square method), decay constant λ can be determined and also contributions of events from other species and a background can be recognized and extracted when the fit uses a more complex function than a single straight line.

One of the disadvantages of this method is that one needs many time bins in order to represent a mixture of events originated from decays of species which differ significantly in the decay constant. The other, more serious problem emerges in the case of a low statistics. When the statistics is low many time bins may contain no events and in consequence the shape of the distribution function strongly fluctuates. In such a situation it is difficult to judge if the decay events come from the decay of single species.

An unconventional way to represent radioactive decay data, first proposed in ref. [58], is to sort events into time intervals of widths proportional to the time: $dt/t = const$. Such sorting enables to represent decay events over a very wide range of times but still using a reasonable number of bins. In this representation the shape of the decay spectrum (density distribution function) is given by:

$$\begin{aligned} \frac{dn}{d(\ln t)} &= \frac{dn}{dt} \frac{dt}{d(\ln t)} = -n_0 \lambda t \exp(-\lambda t) = \\ &= -n_0 \exp(\ln(\lambda t)) \exp(-\exp(\ln(\lambda t))) = \\ &= n_0 \exp(\ln t + \ln \lambda) \exp(-\exp(\ln t + \ln \lambda)) \end{aligned} \quad (4.6)$$

The curve of eq. 4.6 is a slightly asymmetric bell-shaped one. It is also obvious that this shape does not depend on the decay constant λ . It is only shifted by the

4. Radioactive decays, low statistics case

value $\ln \lambda$, while the height of the curve scales with the number, n_0 , of initial nuclei. The integral of this function is equal n_0 . Introducing the new variable $\Theta = \ln t$ one obtains:

$$\frac{dn}{d\Theta} = n_0 \exp(\Theta + \ln \lambda) \exp(-\exp(\Theta + \ln \lambda)). \quad (4.7)$$

The maximum of this function is at Θ_{max} given by the formula:

$$\frac{d^2n}{d\Theta^2} = 0 \rightarrow \Theta_{max} = \ln\left(\frac{1}{\lambda}\right), \quad (4.8)$$

while the second moment (standard deviation) of the curve 4.7 is equal to:

$$\sigma_{\Theta} = \sqrt{\frac{\int_{-\infty}^{\infty} (\Theta - \langle \Theta \rangle)^2 \left| \frac{dn}{d\Theta} \right| d\Theta}{n}}, \quad (4.9)$$

where $\langle \Theta \rangle$:

$$\langle \Theta \rangle = \frac{\int_{-\infty}^{\infty} \Theta \left| \frac{dn}{d\Theta} \right| d\Theta}{n}. \quad (4.10)$$

It can be shown that the σ_{Θ} has a value of 1.28. From the fact that the radioactive decay curve has a universal standard shape one obtains a tool to detect if the second radioactive species contribute to the spectrum. In such a case the measured standard deviation of the logarithm of the decay times

$$\sigma_{\Theta_{exp}} = \sqrt{\frac{\sum_{i=1}^n (\Theta_i - \langle \Theta_{exp} \rangle)^2}{n}}, \quad (4.11)$$

with

$$\langle \Theta_{exp} \rangle = \frac{\sum_{i=1}^n \Theta_i}{n} \quad (4.12)$$

has a larger value. On the other hand, if the standard deviation of the $\sigma_{\Theta_{exp}}$ is significantly smaller then this may imply that the measured spectrum is incomplete as the measurement was not sensitive for the whole range of the possible decay times. But if this can be excluded then this might be a strong indication that at least part of the observed events do not originate from the radioactive decays but from some other sources.

4.2.1. Test procedure

Like the time values, t_i , of individual radioactive decay events, also the standard deviation, $\sigma_{\Theta_{exp}}$, of the logarithmic decay time distribution from a specific experiment evaluated with the equation 4.11 is subjected to the statistical fluctuations. One can, however, estimate the expected magnitude of this fluctuation. This gives a measure for the expected deviation of the width of the measured logarithmic decay time distribution from the expected value.

To illustrate the basic idea of the test proposed here, the authors of ref. [57] consider a case of two decay events. In one measurement their decay time differs by a factor of two or three. Considering the spread of an exponential decay, such a difference in decay times seems to be quite normal. Next, one may assume that in

another sample (experiment) these two decay events differ in decay times by several orders of magnitude. This does not seem, to us, as a “normal” behaviour, rather one is tempted to assign these two events as originating from two different species with very different decay times. In the third example these two events have decay times that are very similar or even equal to each other. Also this case does not seem “normal”. It is very improbable that decays governed by the exponential distribution may give two events of the same decay times. The objective of the test is to give a quantitative measure to judge which one of those three cases is compatible with the hypothesis that decay events originate from a single species.

A closer view on the problem reveals that the expected value of the distribution of $\sigma_{\Theta exp}$ is systematically smaller than the value σ_{Θ} from equation 4.9 and this is especially true in the case of a small number of events. The reason for this difference is that $\langle \Theta \rangle$ in the equation 4.9 is a true mean value of the logarithmic distribution, while $\langle \Theta_{exp} \rangle$ is an estimate of the mean value deduced from the observed events. The expected characteristics of the distribution of $\sigma_{\Theta exp}$ can be calculated with the Monte Carlo method. A number n of the decay events with decay times randomly chosen from a given exponential distribution are analyzed according to the formulas 4.11, 4.12 to determine the statistical sample of $\sigma_{\Theta exp}$. Such a procedure is repeated many times. In the following, these samples of $\sigma_{\Theta exp}$ are denoted by $x_j(n)$, $j = 1 \dots k$, where $k \rightarrow \infty$ is an ideal simulation but practically should be large. From a large number of samples, k , for different values of number of decay events, n , one gets: the expectation value, E_n , the standard deviation, σ_n , and the relative skewness, γ_n , of the quantity $\sigma_{\Theta exp}$ as a function of n calculated according to the relations cited below:

$$E_n = \lim_{k \rightarrow \infty} \left\{ \frac{\sum_{j=1}^k x_j(n)}{k} \right\}, \quad (4.13)$$

$$\sigma_n = \sqrt{\lim_{k \rightarrow \infty} \frac{\sum_{j=1}^k (x_j(n) - E_n)^2}{k}} \quad (4.14)$$

and

$$\gamma_n = \lim_{k \rightarrow \infty} \frac{\sum_{j=1}^k (x_j(n) - E_n)^3}{k} / \sigma_n^{3/2}. \quad (4.15)$$

The results of such a simulation are given, after the authors of ref. [57], in table 4.2. Normalizing the distribution obtained for $\sigma_{\Theta exp}$ from the simulation samples and integrating this distribution up to the levels of 5% and 95% of confidence one obtains the limits which comprise the range of $\sigma_{\Theta exp}$ values that with a 90% confidence level belong to the decay of a single radioactive species. Experimental values of $\sigma_{\Theta exp}$ falling below the lower limit can be rejected with an error chance below 5% to originate from radioactive decay. If the experiment was sensitive to the whole range of decay times then at least part of the events originates from another source, e.g. a periodic noise. On the other hand, experimental values of $\sigma_{\Theta exp}$ which are above the upper limit can be rejected with a 5% error probability as belonging to the decay of a single radioactive species. If any background can be excluded, there is probably another radioactive species with different decay time which contribute to

4. Radioactive decays, low statistics case

the observed events.

Now we will use the test procedure to check compatibility of the alpha decay events observed in the fusion reactions $^{54}\text{Cr} + ^{208}\text{Pb}$, $^{58}\text{Fe} + ^{208}\text{Pb}$ and attributed, from the analysis made in the previous chapter, to the radioactive decay of nuclei ^{261}Sg and ^{265}Hs , respectively. In the case of reaction $^{58}\text{Fe} + ^{208}\text{Pb}$ we identified 8 alpha decay chains coming from the decay of ^{265}Hs isotope. In one detected chain, alpha emitted by the parent nucleus ^{265}Hs was missed by the detection setup. Thus we apply the procedure to the 7 cases of identified alphas that come from the decay of ^{265}Hs . They have the following emission times: 5.55, 3.13, 5.15, 3.96, 1.48, 0.80 and 0.03 *ms*. As ^{265}Hs has two decay modes with slightly different half-lives (0.9 and 1.55 *ms*)² one should expect a larger range of the experimental decay times and thus the experimental standard deviation $\sigma_{\Theta_{exp}}$ should be higher than this given in table 4.2 for the case when $n = 7$. The analysis of those events results in a value of 1.70 for $\sigma_{\Theta_{exp}}$ which is indeed larger than the table value 4.2 but still falls into the accepted interval [0.52, 1.87]. Thus at the 90% confidence level those 7 events are compatible with the assumption that they originate from the decay of a single species - ^{265}Hs .

In the case of ^{261}Sg , tables 3.6 and 3.8, identified alphas have emission times: 0.169, 0.478, 0.303, 0.290, 0.009, 0.022, 0.649, 0.130, 0.244 and 0.245 *s*. The value of the experimental standard deviation of the logarithmic time distribution, $\sigma_{\theta_{exp}}$ is equal 1.43 while the accepted range for the hypothesis of emission by single species is [0.65, 1.82].

Thus again the test confirms that the observed α -decay chains originate from the decay of single species what was previously identified as ^{261}Sg isotope.

Finally one can apply this procedure to check the consistency of alpha decay chains originated from the decay of the last discovered element $^{284}118$ in the hot fusion reaction $^{48}\text{Ca} + ^{249}\text{Cf}$. Alpha chains identified as coming from the decay of that element are characterized with the following emission times: 2.549, 0.465, 0.847 *ms* for decay of $^{284}118$, and 42.1, 1.012, 0.098 *ms* for decay of the daughter $^{280}116$ element, ref. [59]. Calculating $\sigma_{\theta_{exp}}$ in the case of the first source ($^{284}118$) of alphas one obtains 0.70 which falls well in the range of [0.19, 1.91] what supports the assumption regarding the single decaying specie as the source of those alphas. In the second case where the assumed source is $^{280}116$ one gets $\sigma_{\theta_{exp}} = 2.50$ what is well beyond the upper limit 1.91 given by 90% confidence level. The last result may suggest that the daughter radioactive emitter identified as $^{280}116$ can decay from two different states with different half-lives. One should however stress that the rejection of the hypothesis of emission from one state (one specie) with the probability of error less than 5% does not give robust evidence for the interpretation of that data. The additional analysis of that case combined with other information available should help to answer the question.

² We have not applied the test for those two decay modes separately because in three of those seven events, table 3.12, energy of the first emitted alpha was measured incompletely and it was not possible to determine which of the decay mode of ^{265}Hs was the source of the first emitted alpha in these three cases.

Table 4.2.: Expected properties of the distribution of the standard deviation $\sigma_{\Theta exp}$ defined by eqs. 4.11, 4.12 for a given number n of observed events. Experimental values below the lower limit (5th column) can be rejected with an error chance smaller than 5% to originate from radioactive decays. On the other hand experimental values above the upper limit (6th column) can be rejected with an error chance smaller than 5% to belong to the decay of a single radioactive species (ref. [57]).

Number of events n	Expectation value E_n of $\sigma_{\Theta exp}$	Expected standard deviation σ_n of $\sigma_{\Theta exp}$	Expected relative skewness γ_n	lower limit of $\sigma_{\Theta exp}$	upper limit of $\sigma_{\Theta exp}$
1	0	0	0.	-	-
2	0.69	0.58	1.42	0.04	1.83
3	0.89	0.55	1.24	0.19	1.91
4	0.98	0.50	1.13	0.31	1.92
5	1.04	0.47	1.12	0.41	1.90
6	1.08	0.44	1.10	0.48	1.89
7	1.11	0.42	0.99	0.52	1.87
8	1.13	0.40	0.96	0.58	1.85
9	1.15	0.38	0.95	0.62	1.84
10	1.16	0.37	0.90	0.65	1.82
11	1.17	0.35	0.84	0.67	1.81
12	1.18	0.34	0.84	0.70	1.79
13	1.19	0.33	0.82	0.72	1.77
14	1.19	0.32	0.78	0.73	1.77
15	1.20	0.31	0.78	0.75	1.76
16	1.20	0.30	0.76	0.77	1.75
17	1.21	0.30	0.74	0.78	1.74
18	1.22	0.29	0.72	0.79	1.73
19	1.22	0.28	0.69	0.80	1.72
20	1.22	0.28	0.68	0.81	1.71
$n \rightarrow \infty$	1.28	$1.3\sqrt{n}$	$n \rightarrow 0$	1.28- $2.15/\sqrt{n}$	1.28+ $2.15/\sqrt{n}$

4. *Radioactive decays, low statistics case*

5. Superheavy elements studies at TAMU

In this chapter I will present a new experimental approach to explore the region of SHE elements. The experiments described here were performed at the superconducting cyclotron (K500) of the Cyclotron Institute, Texas A&M University (TAMU, USA) between 2003-2006. In the first section, basic idea of that approach is presented. A brief outline of the measurements is given in section 5.2. Preliminary results from the most recent experiment (Autumn 2006) and its detailed description are reported in a later part of the chapter.

5.1. Fusion of projectile with target fission fragment - a new path to SHE production

The classical experimental method (chapter 3) applied to the synthesis of superheavy nuclei gives evaporation residue cross section (σ_{ER}) on the level of 1 *pb* and 0.5 *pb* to synthesize element $Z=112$ and $Z=118$, respectively. For even heavier nuclei one can expect that σ_{ER} is dropping into the region of tens of *fb*. This creates a serious limitation for the technique being used so far. Especially, a completely new generation of heavy ion sources is needed to supply the intensity of ion beams as high as 10^{14-15} particles/sec. Furthermore, more powerful heavy ion velocity filters have to be constructed with a rejection ratio on the level of 10^{14} . It seems that until such instruments will be built we are not be able to reach the region of *fb* cross sections.

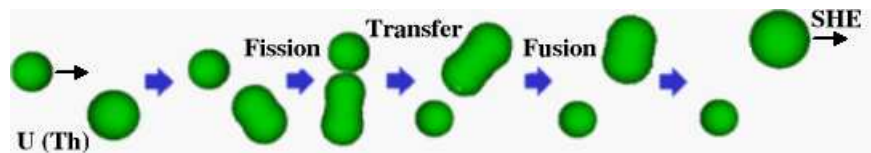


Figure 5.1.: Schematic view of the possible reaction between the fissile target nucleus U (Th) and a heavy projectile (e.g. Yb , Au).

In this context, a new approach to the SHE production was proposed five years ago by the Texas A&M University group in collaboration with groups from the Institute of Physics of the Jagiellonian University and Instituto Nazionale di Fisica Nucleare di Legnaro (INFN, Italy) [60]. It is there suggested to investigate nuclear reactions at low incident energies induced by heavy ion projectiles (e.g. ^{172}Yb , ^{197}Au) on fissile target nuclei (e.g. ^{238}U , ^{232}Th). One possible scenario for such reactions is depicted in fig. 5.1. In the initial stage of the collision, a heavy projectile approaches the target nucleus inducing the fission of the later one (two first snapshots in the figure). Next, a fission fragment is transferred to the projectile nucleus (middle part in the

figure) and, finally if the fusion conditions are met during the transfer process, an excited very heavy system can be formed (last two snapshots in the figure)¹. Does the system survive as a ground state SHE nucleus (residue evaporation)? This depends on the excitation energy and angular momentum brought into this system during the fusion process. The lower its excitation energy and its angular momentum the bigger the chance that the system will end up as an evaporation residue.

Certainly, the probability of that scenario is very small but there are several assets in this hypothesis and they should be mentioned. It is well known that nuclear products originating from low-energy nuclear fission are characterized by a broad spectrum of mass and atomic numbers and majority of them are neutron-rich species (fission fragments). If such a species is transferred to the projectile nucleus, as in the proposed collision scenario, the fusion probability can be strongly enhanced due to its neutron excess. On the other hand, in a situation when the fragment brought to the projectile is not neutron-rich, but has a proton/neutron number near the closed shells, then the survival probability of the formed superheavy nucleus will increase as the fission barrier of the resulting SHE nucleus is high. Besides, if the transfer process of the fission fragment takes place at the peripheral collision the resulting system should be formed with small excitation energy, in consequence its survival probability again increases. Both factors: fusion probability and survival probability, play a decisive role in the production of the SHE elements because they determine the evaporation residue cross section (σ_{ER}).

Although, for this method, there are no model calculations that estimate the value of the σ_{ER} , we know that the fissile nuclei have a very high fission cross section thus one can expect that the SHE elements can be produced here with competitive probabilities comparing to the classical hot or cold fusion reactions. What is more, the fission of target nuclei is this kind of “ion source” that delivers wide spectrum of different heavy ions, therefore, “nature itself can choose” the most appropriate one that will fuse with the projectile ion in order to produce superheavy nucleus. Using for example heavy ion projectile $Z=79$ (*Au*) and the target nucleus $Z=90$ (*Th*) we are supposed to explore properties of superheavy and possibly hyperheavy nuclear systems in the regions of atomic numbers $Z \approx 112$ and $Z \approx 136$. Keeping in mind that the low-energy fission of thorium produces a two humped atomic number spectrum of fission fragments, one hump is peaked at $Z=33$ and the other at $Z=57$.

There is also a drawback of the method. In the proposed reactions a relatively long interaction time is needed to transfer the fission fragment to the projectile. This implies that the deep inelastic collisions will also be involved in the transfer process. As a result, quite high excitation energy of the reaction partners can be generated and consequently the survival chance of the produced superheavy nucleus can decrease dramatically. On the other hand, the second fission fragment can be considered the heat and the angular momentum reservoir with respect to the rest of the system. If it hopefully absorbs the main part of the dissipated kinetic energy of the collision, the superheavy species will leave the reaction region not excited and its survival probability will be high.

Experimental instruments that are located in the Cyclotron Institute of TAMU seem to be well suited for our studies. The cyclotron K500 delivers high intensity beams of heavy ions up to Uranium. The energy of beams are in the range of interest:

¹ In short I will call this scenario fission-fusion .

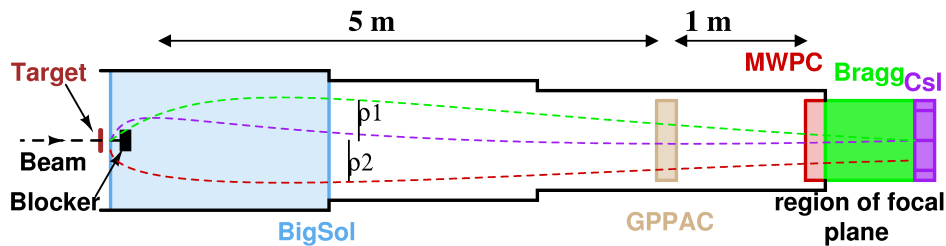


Figure 5.2.: Momentum and charge filter (BigSol) and the detection system used in the first experimental test at the TAMU University (see text for details). Blocker stops the beam nuclei and diminishes projectile-like fragments (PLFs) emitted at small angles. It is also shown how the BigSol magnetic field separates trajectories of different heavy ions - at the exit of the BigSol, trajectories have different distances from the beam axis (three dashed lines).

from a few to several $A.MeV$. Finally, efficient magnetic velocity filter is working on one of the beam lines. This filter, superconducting solenoid (BigSol) constructed at the Michigan State University [61], is characterized by a strong magnetic field and a large entrance angular acceptance. Because interesting reaction products will be emitted at angles greater than ~ 1 degree and we want to use the velocity filter technique to separate those products from other heavy ions produced in different reaction channels, the BigSol solenoid well corresponds to our requirements.

The objective of the research was to verify experimentally the idea presented in this section, especially to estimate the cross section for the SHE production to give answer if the method can be competitive to the standard complete fusion approach.

5.2. Experimental test of the method

The first experimental test was conducted in July 2003 with ^{238}U , ^{198}Pt , ^{172}Yb , targets and ^{172}Yb , ^{198}Pt , ^{238}U beams at energies from 12 to 15 MeV/u . The filtering and detection system (see fig. 5.2) includes: previously mentioned superconducting solenoid (BigSol) and multi-element detector system [62] which is composed of a position sensitive parallel plate avalanche counter (GPPAC in the figure), a multi-wire proportional counter (MWPC), a Bragg chamber and CsI scintillators where expected SHE nuclei are supposed to be implanted. After the target, a blocker was placed in order to stop the beam and to select reaction products emitted in the angular range 1-6 degrees. Those heavy ions subsequently entered the superconducting solenoid.

The magnetic field (B) of BigSol is axially symmetrical and parallel to the beam direction (Z -axis). Such a configuration of the field enables to separate spatially different charged heavy ions in a case when they have the velocity component perpendicular to the Z axis. Depending on the value of the velocity component, the mass and the charge, the heavy ions exit the filter at the different distances ρ from the beam axis, ρ_1 and ρ_2 in the figure. The ρ is given by the well known formula $p/q = B\rho$, where p is a momentum and q is a charge state of the heavy ion. The heavy ions can be identified subsequently using software circular aperture. The value of the magnetic field has to be carefully adjusted in order to achieve a good separa-

5. Superheavy elements studies at TAMU

tion of the reaction products and to focus them in the region marked in the figure as a focal plane. The focal plane is located approximately 4 meters beyond the BigSol where the Bragg and CsI detectors are situated.

The MWPC detector returns X and Y coordinates (plane perpendicular to the beam) of the detected heavy ion. Its entrance active area is $7 \times 7 \text{ cm}^2$. With the help of this detector one can define software selection for the circular aperture. Besides, together with the GPPAC counter it is used for the time of flight (*ToF*) measurements. The Bragg detector registers energy loss (ΔE) via the total collected charge generated by the heavy ion passing through the detector. After the Bragg, a couple of large area CsI scintillators (5 mm thick) for measurements of residual energy (E) of implanted reaction products are mounted. The CsI instead of Si detectors were chosen in order to avoid severe radiation damages caused by stopping beam-like and PLF ions.

Under the constrain imposed by the $B\rho$ of the solenoid and by measuring ΔE and E of the heavy ion it is possible to determine its Z and A (atomic and mass number), using the well known Bethe-Bloch formula $\Delta E = kAZ^2/E$ and magnetic selection criteria $B\rho = \sqrt{2AE/q^2}$.

The objective of that test experiment was to check the usefulness of the experimental setup and to find the optimal values of the BigSol magnetic field for the selected beams and targets that would ensure the best conditions to select heavy reaction products. It was found that the selection of reaction products with $Z \geq 70$ is achieved for the $B \cong 2$ Tesla. This conclusive result convinced us that the experimental setup is reliable and the group should continue this research.

In the next run (March-April 2004), the experimental setup was further modified. The measurement itself was performed with the target of ^{232}Th (5.9 mg/cm^2 thick) and the beam of ^{238}U (12 A.MeV). The implantation CsI crystals (fig. 5.2) situated after the Bragg chamber were replaced by the Yttrium Aluminum Pervoskite inorganic scintillators (YAP) [63]. This relatively new scintillator was chosen because it has higher radiation hardness than the CsI and one can also expect improved linearity of the pulse height with the energy deposited by a heavy ion. The array of YAPs consisted of 14 scintillators, each having 13.5 mm diameter and 3 mm thickness. When the reaction product associated with large ΔE signal in the Bragg chamber was implanted in the YAP, the beam was turned off and the signal in the scintillator was recorded by the flash ADC during 1.3 ms to register the possible subsequent decays (α or spontaneous fission) of the expected superheavy nucleus.

It turned out that the serious problem, in this type of experiment, is the background associated with the high reaction cross-section for elastics, deep-inelastics and few nucleon transfers. Products of such reactions appear to be difficult to get rid of using only the selection on the magnetic rigidity $B\rho$. The problem is connected with the fact that even if the products have different momenta p , they have distribution of the charge state q on the exit of the target and in consequence some fraction of the products will have very similar $B\rho = p/q$ to that expected for the superheavy nuclei. The cross-section for those reactions is orders of magnitude higher than the production cross-section of the SHE elements and even a small fraction of these products give a large background in the detector system. To improve in flight selection of interesting fragments several modifications of the detection setup were realized for the next experimental run.

In order to equilibrate the charge state, what ensures a more precise selection in $B\rho$, of reaction products entering the BigSol filter two possibilities were taken into account. The first solution was to fill up the filter with a noble gas at low pressure. This way the trajectories of heavy ions traversing gas medium should be close to the paths corresponding to their mean charge state. An alternative possibility was to mount several stripper foils (e.g. mylar) inside the BigSol what will also equilibrate the charge of the ions. Although charge state dispersion of the products should decrease after applying one of those solutions, enabling a better separation of a different class of products, there is also a drawback. Energy loss in the gas or in the foils has the effect of defocusing of all the products passing the filter. A simulation of heavy ion trajectories made for both variants showed similar results. However, a common problem in all gas-type systems is a gas leak, therefore, filling up the BigSol with a gas medium may cause difficulties with keeping the high vacuum in the rest of the beam line what is essential to control the beam ions. For this reason, we decided to mount, inside the filter, 9 equally spaced $0.9 \mu\text{m}$ thick mylar foils.

The next modification of the experimental setup consisted of mounting two, position sensitive transmission detectors. They are Italian and Krakow made PPAC counters: IPPAC, KPPAC respectively. The first detector is situated after the blocker and it is able to work in the intense magnetic field and handle a high counting rate. It is segmented radially into 16 sectors. The second detector was inserted about 2 meters after the solenoid and 1.8 meter before the GPPAC. This detector is not segmented. Both detectors are used to measure the positions of heavy ions and their time of flights over the path to the MWPC counter. In the case of the IPPAC the path is equal to 5 meters while for the KPPAC it is equal to 2.86 meters. The ToF measurements are used for the mass identification of the detected reaction products while the measured positions serve to reconstruct heavy product trajectories inside the BigSol solenoid.

The work of Colin et al. [64] indicates that interaction of heavy projectile and heavy target nuclei at higher impact parameters favors asymmetric divisions of separating systems in the exit reaction channel. This is reported for many reactions and the example is $^{238}\text{U} + ^{238}\text{U}$ at 24 $A.MeV$. Therefore, the impact parameter selection may allow to tailor the mass distribution of emerging projectile-like (PLF) and target-like (TLF) entities to favour particular asymmetries, especially those which lead to the superheavy PLFs. For that, significant mass rearrangement has to occur during the reaction. In consequence, the incident energy is to be high enough to overcome the Coulomb forces, especially the Coulomb barrier, so the partners can interact a longer time to ensure large mass exchange between them. Unfortunately, this can lead to the large excitation energy of the PLF and the survival probability of that entity can drastically decrease. In conclusion, the collision energy has to be a compromise between the requirement of the low excitation of the PLF and the long interaction time of reaction partners.

The new detection system was used in the experimental run conducted in August 2004 where we have studied reactions with following projectiles-targets combinations: ^{172}Yb (7.5, 10 and 15 $A.MeV$), ^{197}Au (7.5 $A.MeV$), ^{136}Xe (7.5 $A.MeV$) and ^{84}Kr (7.5, 15 and 25 $A.MeV$) on a ^{232}Th target and with ^{238}U (7.5 $A.MeV$) projectiles on ^{nat}Ti , ^{64}Zn , ^{90}Zr and ^{232}Th targets.

The objective of this run, besides testing the modified detection setup, was to find

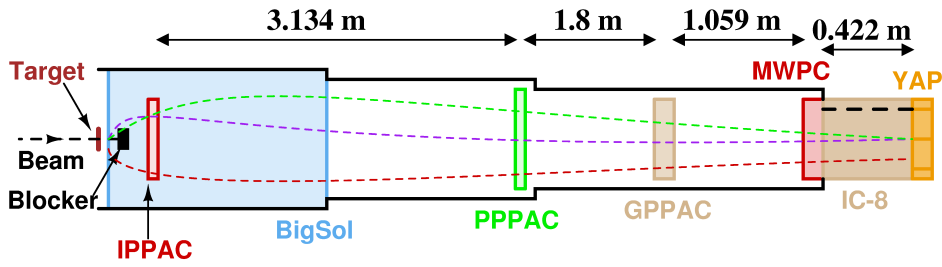


Figure 5.3.: Modified detection system of superheavy elements (experiment August 2006). In place of the Bragg detector a new 8 segments ionization chamber (IC-8) was installed. Instead of previous KPPAC, a new one (also built in Krakow) segmented (4x4) in X and in Y direction was mounted (PPPAC). The Italian PPAC (IPPAC) is situated after the target and the blocker.

the optimal beam energy with respect to the entrance channel Coulomb repulsion and the excitation energy of the projectile-like fragment to further restrict the candidate reactions for the SHE production.

The analysis of the collected data demonstrated a few tens of events which are consistent with the expected signature of superheavy ions. These events have passed all the rejection tests we could implement with our current setup. The SHE candidates appeared mostly in systems at lower incident energy (7.5 *A.MeV*), in the reactions $^{197}\text{Au} + ^{232}\text{Th}$ and $^{238}\text{U} + ^{64}\text{Zn}$. However, it turned out that the setup needs significant improvement before a possible synthesis of superheavy elements can be claimed. In particular, still better separation of the candidates from the high cross-section products (elastics, deep-inelastics) must be achieved. Next, the background should to be further reduced because we plan to use a silicon implantation detector to measure alpha decay chains coming from the implanted nuclei.

5.3. 2006 experiment - most recent results

As a result of the data analysis for the previous experiment (sec. 5.2), our group decided to study the reaction ^{197}Au (7.5 *A.MeV*) + ^{232}Th as most suitable to produce the SHE systems. The run in August 2006 started with the objective to confirm the existence of SHE candidates and eventually to characterize them better than in earlier measurements. To reach this objective the experimental setup, fig. 5.3, was again improved. In the next sections I will describe this modified setup, calibration procedure for the main detectors, and preliminary results obtained from that run.

5.3.1. Detection setup

The experience that we gained so far, convinced us to replace the Bragg detector with an ionization chamber. The chamber (IC-8), fig. 5.4, was built in the INFN laboratory. It can measure several energy losses (ΔE_i , $i = 1, \dots, 8$) of heavy ion along its path in the detector. The ΔE_i measurements are used subsequently to identify more precisely the atomic number (Z) of detected heavy ion. The chamber is composed of 8 independent sections. Each section has 4.65 *cm* length with the anode situated at the left side wall, facing the beam direction, of the box section. This way,

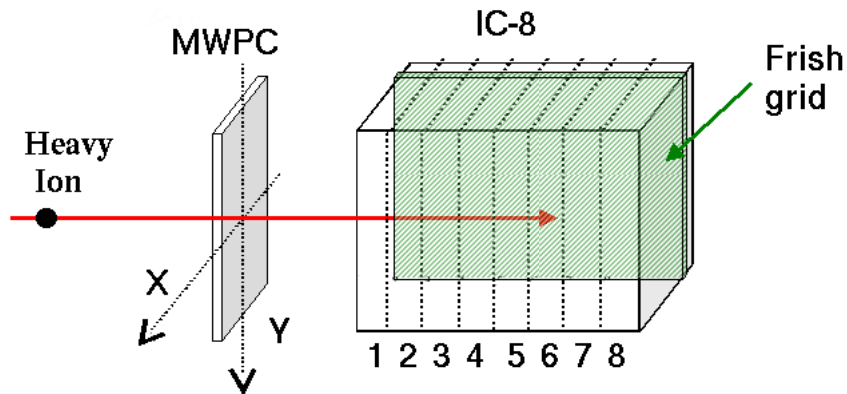


Figure 5.4.: Schematics of the ionization chamber (IC-8). It is segmented into 8 parts. Frish grid (green area), which ensures independence of the collected charge generated by ion passing through the chamber along the position it enters each individual section, is placed on the left side (negative values of X coordinate) in the chamber. In the direct vicinity of the IC-8, a multi-wire position sensitive proportional counter (MWPC) is mounted.

the anodes generate the electric field that is perpendicular to the trajectory of ions passing through the chamber. The charges collected by the anodes are proportional to the energy losses of an ion that goes through individual sections. Additionally, a Frish grid is placed near the anodes to ensure the pulse height (collected charge) independence on the heavy ion trajectory location in consecutive sections. All eight sections are placed in one aluminum cylinder, filled with isobutane under the pressure 30 *mbar*.

The detector is mounted in the region of the BigSol focal plane, between the multi-wire proportional counter (MWPC) and the YAP array. In fact, it also plays the role of a Bragg detector but is much easier in operation than the previous Bragg system.

The next improvement of the experimental setup was made by installing the transmission parallel plate avalanche counter (PPAC). This detector is used for the time of flight measurements and for the reconstruction of heavy ion trajectories, photo in fig. 5.5. It was built in Krakow and has replaced the KPPAC chamber. The PPAC counter can sustain higher counting rates and easier distinguish double hit events. It consists of two parallel planes of wires with 96 wires on a plane. The wires are soldered to a rectangular board on which delay lines are placed. The distance between wires in a plane is of 1/10th inch (U.S. customary units) while the planes are 6.5 *mm* apart. Wires from one plane are perpendicular to the wires on the other one. Between the planes an anode in the form of thin (1.5 μm) two sides aluminized mylar foil is mounted. Both planes and anode are tightly screwed and placed inside a duraluminum plate-like construction composed of two parts. Both of them have a circular window opening, which defines the active area of the detector, with a diameter of 240 *mm*. These windows are closed by an aluminized mylar foil of 1.5 μm thickness. This whole arrangement is fitted into the ion pipe, 2.63 meters from the BigSol center in such a way that the wire planes are perpendicular to the trajectories

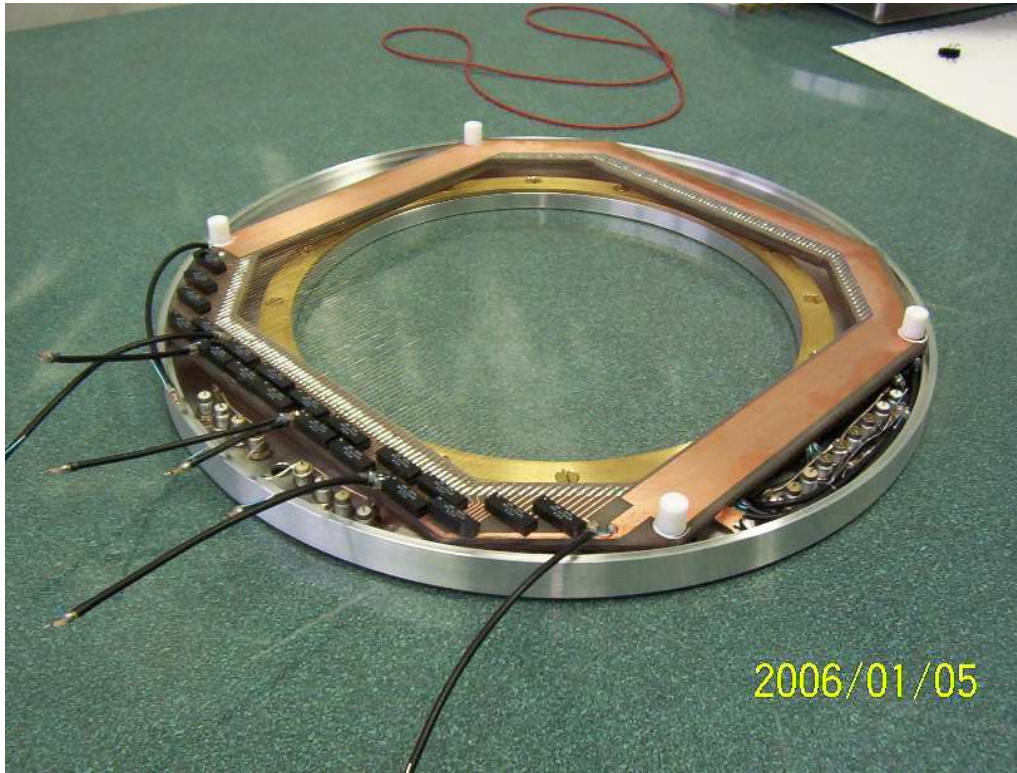


Figure 5.5.: Photo of the final stage of construction of the parallel plate avalanche counter (PPAC) that was built in Krakow. Inside duraluminum plate (silver color) with a circular opening, two boards (the lower one is shadowed by the upper one) covered by copper and wires soldered to it are placed. The delay lines (black cubes) mounted on the board can also be seen. To better see the construction of the detector, anode aluminized mylar foil is dismounted. In the operational mode this anode foil is placed between the boards. The detector is opened - the other duraluminum plate is removed.

of incoming ions. The detector is filled with isobutane of 4.3 *mbar* pressure and a high voltage of -450 *V* is applied between anode and cathodes (wires). This ensures avalanche regime of the detector work.

Because the detector has to sustain high counting rates, wires on each plane are grouped into four segments. Each of the segments is operated by a delay line with 2 *ns* delay per wire. Both ends of the delay line for a given segment are connected to the electronics. A voltage pulse from a wire, generated by the collected charge from the ion passing through the gas, is directed to the delay line to which the wire belongs and splits to the both ends of the delay segment. The electronics measure the arrival time of the split pulse from the ends of the segment and from that the position (wire number) in one direction can be determined. The position for the other direction is returned by the wire which fired from the second plane. Both positions *X* and *Y*, together with positions from other detectors, are used to reconstruct the ion trajectory after the BigSol. To measure time of flight of heavy ions a common signal from the detector anode is taken. Because of segmentation, this modified version of the PPAC is in fact composed from 16 independently working avalanche counters.

Table 5.1.: Beams from superconducting K500 cyclotron of TAMU to calibrate detection setup. Calibration runs were performed with the BigSol magnet switched off, no target was placed in the target holder and beam blocker was removed. Those beams (direct beams) were delivered directly to the multi-detector system.

Beam	^{40}Ar	^{84}Kr	^{129}Xe	^{172}Yb	^{197}Au	^{238}U
Energy (<i>A.MeV</i>)	15.0	15.0	15.0	7.5	7.5, 15.0	7.5

5.4. Detectors calibration

5.4.1. Energy loss and time of flight calibration of the experimental setup

There are two important sets of quantities, delivered by the detection setup, which need to be calibrated. One set is for tracking ions trajectory through the BigSol filter. To determine these trajectories we use the following detectors: Italian PPAC, PPPAC, GPPAC and MWPC. The other set of quantities are the time of flight (*ToF*) and energy losses (ΔE_i , $i = 1..8$) of the ion. This information is obtained from the ionization chamber (IC-8) which measures energy losses, and pairs of detectors for time of flight measurements: PPPAC - MWPC for one ToF_{PM} and GPPAC - MWPC for the other ToF_{GM} . The identification of the atomic number of reaction products is based on two types of signals: ΔE_i from the IC-8 and the ToF_{PM} or ToF_{GM} . In table 5.1, there are listed beams that were used to calibrate time of flight detectors and energy loss signals.

In a first step IC-8 was calibrated. As it is composed of 8 independent ionization sections each of them need separate calibration. In fig. 5.6 measured energy losses by peak sensing ADCs in selected sections are plotted as a function of calculated energy losses for ion beams of table 5.1. Two phenomenological energy loss programs were used for that calculation. It should be stressed however, that the calculations especially for very heavy ions are not very precise. This is due to the fact that in the low energy region (2-10 *A.MeV*) limited experimental data on energy loss of very heavy ions is available. Here we used the SRIM [65, 66] and the Orsay tables based program [67]. As one can see from the figure, these two codes predict similar energy losses in the case of Ar ions but start to deviate for Kr and heavier ones. For the heaviest nuclei like U, the difference in predicted energy losses is as large as 30 %. We will further discuss the predictions of both codes after presenting the time of flight calibration on the example of detectors GPPAC and MWPC. The ToF_{GM} is directly connected to the velocity of ions and to their energies in the case of direct beams.

The distances (the bases) for ToF_{PM} and ToF_{GM} measurements are 285.9 *cm* and 105.9 *cm*, respectively. The time of flight base for the pair Polish PPAC - MWPC detectors is thus larger than for GPPAC - MWPC pair, so the velocity of heavy ions should be more precisely estimated from the measurements of ToF_{PM} .

In the case of the pair of detectors GPPAC - MWPC, three different procedures were applied to accomplish *ToF* calibration. As a result, one receives three calibration equations of the type: $ToF[ns] = A[ns/ch] \cdot Ch[ch] + B[ns]$, where *ToF* is a calibrated time of flight expressed in *ns*, *A* is a conversion factor in units *ns/ch* while *ch* is a measured electronics channel value corresponding to the time of flight of an

5. Superheavy elements studies at TAMU

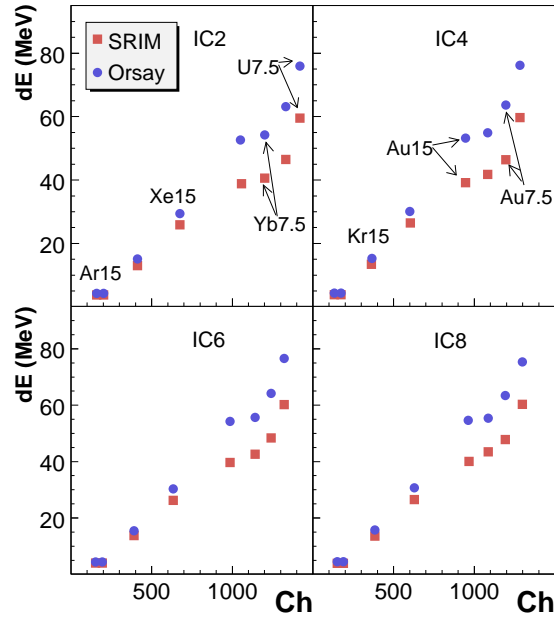


Figure 5.6.: Calculated energy losses ΔE (MeV) versus measured ΔE (channels) for sections 2, 4, 6 and 8 of the IC. Beams are specified in table 5.1.

ion and B is the offset value introduced by the electronics. In the procedure, coefficients A and B have to be assigned. These calibration procedures will be discussed in more details further on. We used data from runs measured for direct beams, listed in table 5.1, except in the case of ^{238}U ions where the ToF electronics was not yet set. For each direct beam a position of the TDC channel peak of time of flight was assigned. Using different delay lines the conversion factor (A) from the TDC channel to ns , $A = 0.11 ns/ch$ was measured. Both energy loss codes (SRIM and Orsay) deliver very similar energy losses in each IC-8 segment in the case of ^{40}Ar (15 A.MeV) direct beam, see fig. 5.6. They predict also the same energy of argon ions at the exit of GPPAC. Taking this in mind we applied the first calibration procedure (I): we took for a conversion factor value of $0.11 ns/ch$ while the offset B was determined using the calculated energy and hence the ToF of ^{40}Ar ions at exit of GPPAC. The second calibration (II) was performed using calculated values by SRIM code of all direct beam energies on the path between GPPAC and MWPC. Then by applying linear fit to the calculated ToF and measured channel position of the TDC peaks for each beam, we assigned A and B in the calibration equation. Finally, the third calibration (III) was performed applying a similar procedure as in II, but Orsay energies of direct beams were taken into account. The results are presented in table 5.2.

Based on these results figure 5.7 presents $Rd = (E_{calc} - E_{ToF})/E_{ToF}$ that is a relative difference between calculated energies at the exit of GPPAC, E_{calc} , from both codes (SRIM, Orsay) and energies, E_{ToF} , determined by using the ToF calibration of each of the three methods (I, II and III). The overall Rd is not larger than 5%. The uppermost panel of the figure presents Rd for calibration I. As one can see the agreement between SRIM and Orsay code calculation is good in the case of Ar , Kr ,

Table 5.2.: Three different calibrations of the ToF_{GM} for GPPAC - MWPC detectors. A is a conversion factor from the TDC channels to ns while B is an offset introduced by the applied electronics. See text for details of procedures for obtaining calibrations I, II and III.

Method	I	II	III
A (ns/ch)	0.110	0.112	0.116
B (ns)	238.440	242.220	250.137

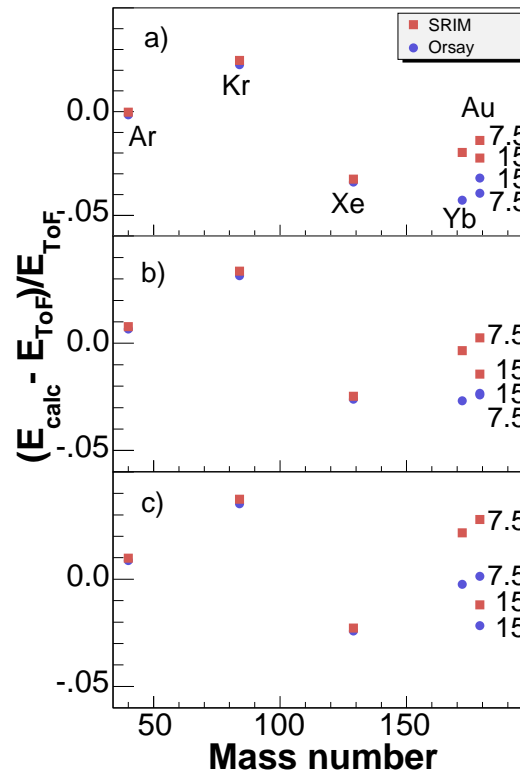


Figure 5.7.: Comparison of SRIM and Orsay energy loss code predictions for direct beams marked in the picture, in the case of three different time of flight calibrations accomplished for the detectors GPPAC - MWPC. E_{calc} - energy at the exit of GPPAC predicted by energy loss programs, SRIM or Orsay. E_{ToF} - energy at the exit of GPPAC obtained from the ToF calibration. a), b) and c) corresponds respectively to the calibration I, II and III of table 5.2.

Xe ions but SRIM gives a smaller difference Rd for *Yb* and *Au* ions. The same behavior of Rd one observes also for calibration II, middle panel of the figure. For procedure III, bottom panel, Orsay and SRIM deliver similar predictions of energy loss for *Yb* and *Au* (7.5 *A.MeV*) ions on the exit of GPPAC except for *Au* (15 *A.MeV*) where SRIM is more exact. What is more if one compares calibration coefficients values A and B for those three procedures (table 5.2) it is seen that these values are quite similar in the case of the SRIM (II) and the Orsay (III) calibration. From this, one can only conclude that the prediction of the SRIM code should be treated as a more exact estimation of the energy loss of heavy ions in the IC-8 ionization chamber while predictions of the Orsay code can be used as an upper estimation of those energy losses.

In what follows we will use the SRIM calculation to calibrate IC-8 energy loss signals and time of flight TDC signals. In principle for the calibration of ToF one should use for a value of conversion factor A , the value obtained from the measurements with delay lines and this was performed in the case of calibration (I). However, calibration (I) uses only one data point (^{40}Ar , 15 *A.MeV*) to assign coefficient B and this can introduce some systematic deviation in ToF for ions much heavier than argon ions. Calibration (III) (Orsay based), delivers a very similar value of A , and takes into account all direct beams data points, thus ToF , assigned from it, should be more reliable for the heaviest detected ions.

In further analysis the Orsay program will be used to obtain the upper estimate of the maximal energy loss of reaction products in different parts of the detection system.

5.4.2. Flash ADC pulse shape analysis. Direct *Au* beam at 7.5 *A.MeV*

The ΔE_i signals generated in the segments of the ionization chamber (IC-8) by a heavy ion that passes through the chamber are also recorded by Flash ADCs (FADC). Each segment is connected to one FADC. The FADCs are opened by a period of 10 μs and use sampling bin equal to 80 *ns*. The duration of a typical signal is around 1-2 μs what gives about 15-20 useful points for pulse shape analysis. One of the objectives of such an analysis was to eliminate double hit events, further discussed in the next section.

First of all, for each signal, we evaluated the FWHM² (full width at half maximum), the maximum value of the signal (V_{max}) and the time at which the signal reaches half of its maximum (T_{W1}), fig. 5.8. This analysis was performed for the beam of *Au* ions at energy 7.5 *A.MeV*. Looking at the FWHM and the V_{max} of the pulse, for each segment of the IC, as a function of the horizontal entrance position (X_{MWPC}) of *Au* ions in the MWPC counter a strong dependence is noticed as it is seen on the left panel of fig. 5.9. One has to remember that the Frisch grid of the IC is placed at the negative value of X (see fig. 5.4) what corresponds to $X_{MWPC} \equiv X_0 = -420$ channels. Going away from the grid, Width (W) increases while V_{max} decreases. This behaviour can be explained by the straggling of electrons released by the passing *Au* ion. If the trajectory of the ion is far away from the Frisch grid, generated electrons have a longer distance to the detector anode and due to the straggling, the electron cloud is spreading out what is observed in FADC as a pulse that has wider W and

² In the following we will also name it Width (W).

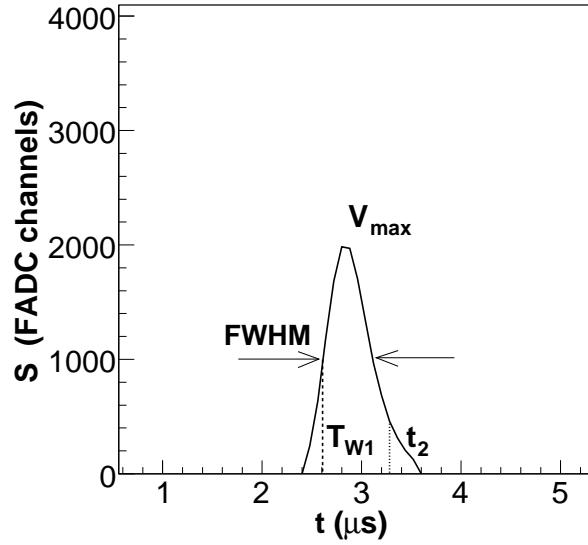


Figure 5.8.: Amplitude (S) as a function of time (t), acquired by FADC, of the pulse produced by heavy ion going through the ionization chamber, in this example it is the first segment of IC. This pulse can be characterized by three quantities: V_{max} , FWHM and time when the pulse is at the half of its maximum - T_{W1} . Arbitrary time, t_2 , is introduced to explain the corrections made to the pulse shape (see text for details).

lower V_{max} .

As a result, for a given energy, the signal produced in the point nearest the grid has higher amplitude and is narrower than the signal produced far from the grid. Consequently, corrections have to be introduced in order to have the same signals in a given segment for the same ions with the same energy independently on the ion trajectory in the IC-8 chamber. This was done on the event by event basis.

As a reference we took the Width (W) for signals produced in the vicinity of the Frish grid (X_0). First, linear dependence was assumed between W and X_{MWPC} as it is illustrated in the figure 5.9 in the case of segment 6 of the IC (the upper right picture of the left panel). Next, for each segment of the IC we determined the slope (m_W) of this linear dependence. The slopes, going through the whole active area of the detector, result to the corrections of about: 6%, 6%, 4%, 4%, 2%, 4%, 4%, 4% in pulse Width for subsequent FADCs.

In order to get the proper shape of the signals with such corrected Width (W^{corr}) the timing of the signal has to be readjusted. For a given pulse, if we consider an arbitrary point with time t_2 (fig. 5.8) the corrected time t_2^{corr} should be:

$$t_2^{corr} = (t_2 - T_{W1}) \cdot (1 - D_W) + T_{W1}, \quad (5.1)$$

where $(1 - D_W)$ is the correction factor, given by the following formula:

$$D_W = [m_W \cdot (X_{MWPC} - X_0)] / W. \quad (5.2)$$

One has to notice that the amount of charge released by the ion passing through the chamber should not depend on its trajectory thus the integral of the Flash ADC signal should be independent of the position in the IC chamber (or on the X_{MWPC}).

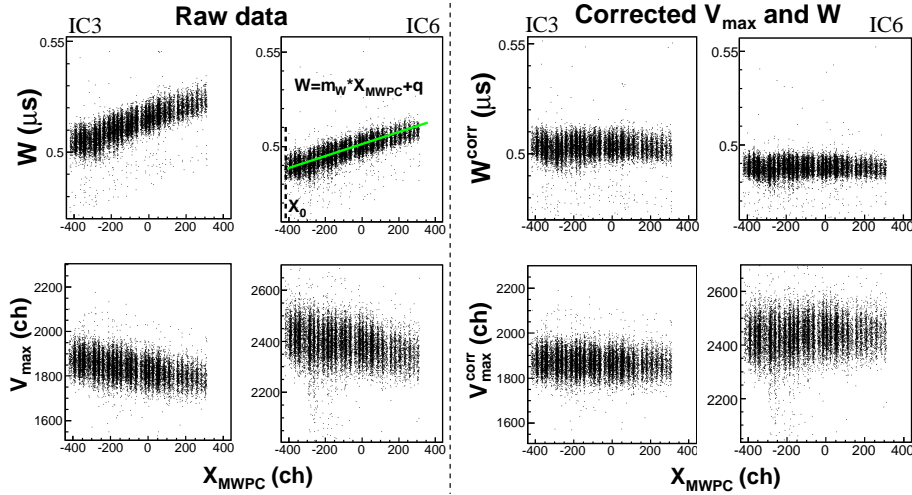


Figure 5.9.: For Au ions ($7.5 A.MeV$, direct beam), left panel presents FWHM (W) and maximum amplitude (V_{max}) of the FADC pulses as a function of the horizontal position in the MWPC. Right panel illustrates the results of the correction procedure applied for recorded FADC pulse in the case of W and V_{max} . In the figure data for segment three (IC3) and six (IC6) of the ionization chamber were analyzed.

Consequently we have to also apply suitable correction to the maximum amplitude (V_{max}):

$$V_{max}^{corr} = V_{max} + (X_{MWPC} - X_0) \cdot D_m, \quad (5.3)$$

where factor D_m is:

$$D_m = m_W \cdot V_{max} / W^{corr}, \quad (5.4)$$

and correction to all points in the pulse S :

$$S^{corr} = S \cdot V_{max}^{corr} / V_{max}. \quad (5.5)$$

After these corrections we obtain the plot shown in the right panel of fig. 5.9.

Finally one can mention that the standard (peak sensing) ADCs connected to the sections of the ionization chamber measure the amplitude of the signal that is integrated for a time long enough to hide the effects observed for the FADC.

5.4.3. Pileup rejection - electronic unit and FADC pulse shape analysis

In the experiment, the acquisition system reads out electric signals produced by all the detectors of the experimental setup when the MWPC detector is fired by the heavy ion. This detector serves as a trigger unit for starting the acquisition. It delivers also the start signal for ToF measurements. With the counting rate at the level of 200-300 counts/s, it may happen that during the time the acquisition needs to process all signals for a given event, another heavy ion enters detection setup and detectors will produce additional pulses which will be mixed up with the pulses of the

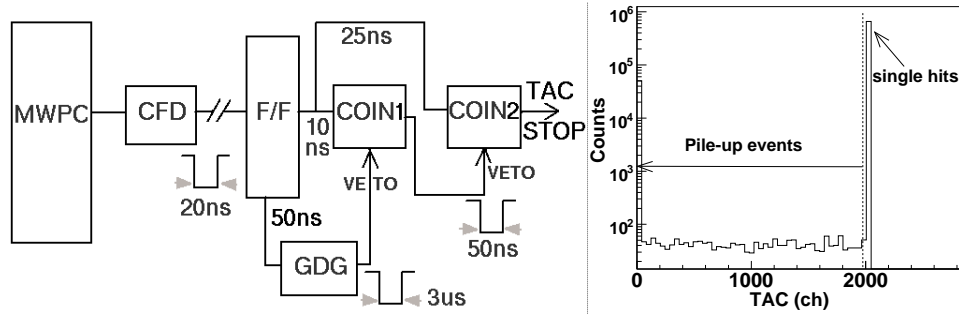


Figure 5.10.: Electronic logic used for the triggering unit - the MWPC counter, to detect pileup events in the TAC module (left panel). Details are given in the text. Right panel presents collected spectrum of the TAC in the case of reaction $^{197}\text{Au} + ^{232}\text{Th}$, 7.5 A.MeV. All events below channel 2005 are pileups.

triggering (primary) ion. The acquisition will record information that not necessary can be attributed to the single ion. This type of events are known as double hits or pileups.

The pileups introduce ghost events, what more pileup events can mimic detection of very heavy nuclei. Due to this undesirable background effect, special attention was given to the detection and electronic setup, in order to minimize the number of such events. Two complementary methods were used to reject double hits.

The first method applied the electronic logic connected to the multi-wire proportional counter. Schematic of that electronics is presented in fig. 5.10. A timing signal from the constant fraction discriminator (CFD) of the MWPC detector was used for this purpose. First of all, the pulse width of the CFD was reduced from 100 ns to 20 ns. Next, MWPC fun-in/fun-out (F/F) output (situated in the acquisition bay) was delayed by 25 ns with the help of a cable and vetoed by itself with 10 ns delayed signal in the second coincidence unit (COIN2). The output of the vetoed signal is further delayed by 50 ns cable and passes to the STOP input of the time amplitude converter (TAC), in order to match up to the start signal. The second output from the F/F is delayed by 50 ns and by using a gate and the delay generator (GDG) produces veto signal of 8 μs wide³ for the first coincidence unit (COIN1). This way the pileup signals from ions coming within 8 μs should be recorded by the TAC. The spectrum of the TAC is shown in the right part of the figure 5.10. Events that produce single hits in MWPC are those which have TAC channel value above 2005. Those events are further considered in the analysis, those which have values below channel 2005 are the pileups and are rejected from the analysis.

The second method is based on the FADC pulse shape analysis. Those flash ADCs are connected to each segment of the IC-8 ionization chamber. The FADC is opened in the time window of approximately 10 μs after MWPC produces the event trigger. In the case of only one heavy ion detection, in that time, by the ionization chamber, its pulse shape is slightly asymmetric, Gaussian like, as shown in fig. 5.8. On the other hand, if during the time of the opening of FADC another heavy or light ion enters the ionization chamber the second pulse is recorded by FADC. Depending on the time interval between the detection of two heavy ions and their trajectories in the

³ At the very beginning of the experiment this signal was 3 μs wide.

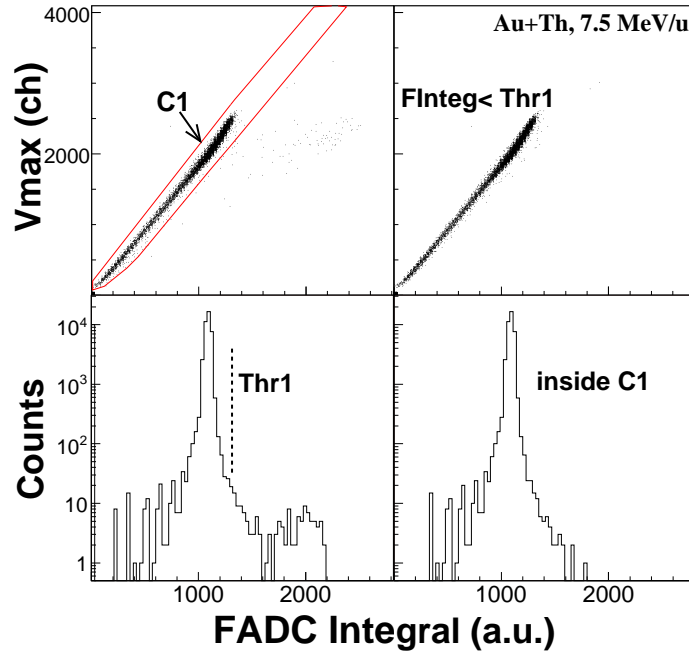


Figure 5.11.: For the first section of the ionization chamber the figure presents in the upper part: maximum amplitude (V_{max}) versus not normalized surface (FADC Integral) of the pulse shapes recorded by FADC, in the lower part: spectrum of normalized surface of the pulse shapes. Two definitions of double hits - pileups are used: outside of contour C_1 or on the right side of the threshold Thr_1 . For further discussion of the figure see text.

ionization chamber recorded pulses can be well separated - two distinct pulses are clearly visible (long time interval between the detection of two ions or quite distinct trajectories of these ions in the chamber) or they can slightly overlap and, in this case, a pulse with two maxims is produced. There is also the special case of double hits. If the ions arrive from the same bunch of the beam - almost the same time of arrival to the ionization chamber, the resulting shape of the pulse is very similar to the pulse produced by a single ion and in this case it is not possible to distinguish one hit from two hits. To find two separated and overlapped pulses two approaches were used.

The shape of the pulse can be characterized by two basic parameters: surface under the pulse (integral over the time duration of the pulse) and its maximum amplitude. As both parameters are proportional to the charge generated by the heavy ion, the dependence between them should be linear, in the case of a single hit, as it is shown in the left upper part of fig. 5.11. For events with double hits, the integral of the two pulses, overlapped or separated, is not proportional to the maximum amplitude of the pulse any more. Such events can be seen outside the contour C_1 in fig. 5.11. Based on this observation one can use contour C_1 drawn for first section of IC-8 chamber and appropriate contours for the rest of the sections of IC-8 to eliminate pileups in the analysis.

For the other approach we re-normalize the amplitude of each pulse produced by a heavy ion to the same value of 2000 channel, correspondingly the full shape is also re-normalized and the FADC integral of such a normalized pulse is calculated. The spectrum of the FADC integrals, for sample of events, is shown in the lower left part of fig. 5.11. The renormalization procedure ensures that in the case of an event with double hits, FADC integral is much larger than the pulse integral of single hit, region of channels ≈ 2000 and ≈ 1000 , respectively. This affect is more pronounced in the case when the double hits produce well separated pulses and less clear when the pulses overlap. For the spectrum of the figure one defines value of Thr_1 equal to 1300 channel as a threshold above which pileups are present. Analyzing pulse shapes, it was verified, that such a value of threshold properly distinguish double hit events from single hit events. The procedure is applied for each section of the ionization chamber.

A comparison of both approaches is presented in the right panel of fig. 5.11. The spectrum of V_{max} versus FADC Integral (upper right part of the figure) is draw with the condition that normalized FADC Integral is smaller than the Thr_1 while the spectrum in the lower right part of the panel is drawn with the condition that events are inside contour C_1 . It is seen that both methods give similar results. When the threshold Thr_1 is used to identify pileups, the spectrum of V_{max} vs FADC Integral is free of double hits and similarly if the contour C_1 is applied to reject pileups, the bump observed in the lower left part of the figure disappears in its lower right part.

It is also of interest to check the effectiveness of the identification of pileups in both TAC and FADC methods. This is done in the fig. 5.12. Here we used the normalized FADC Integral approach. It can be seen that the TAC is more effective for the identification of pileup events. Almost 95% of the double hits identified by FADC Integral is also identified by the TAC, except the region of events in the first quadrant of the crossing lines when the FADC Integral approach is superior. In the third quadrant TAC identifies all events as pileups while the FADC method fails probably because two heavy ions enter the ionization chamber with a very small time difference or the trajectory of those ions passes through the same regions of the chamber. In both cases the pulse shapes of the two ions will completely overlap and will be sampled by the FADC as a pulse coming from the one ion.

In conclusion, TAC and flash ADC methods are complementary and both need to be used in order to properly eliminate double hit events from the analysis.

5.4.4. Position sensitive detectors

After the BigSol filter there were mounted three transmission gaseous detectors that are position sensitive: PPPAC, GPPAC and MWPC (fig. 5.3). The purpose of these detectors was to measure time of flights of heavy ions between corresponding pairs PPPAC-GPPAC (ToF_{PG}), GPPAC-MWPC (ToF_{GM}) and PPPAC-MWPC (ToF_{PM}) as well as to determine the positions in the X-Y planes (they are perpendicular to the beam axis) of detected heavy ions for each counter. This information was used in further analysis to more precisely characterize registered heavy ions and also to reject double hit events.

In this section I will describe the procedure we applied to obtain the calibrated positions of detected heavy ions in the individual detectors. This will be done on the example of the Polish PPAC (PPPAC).

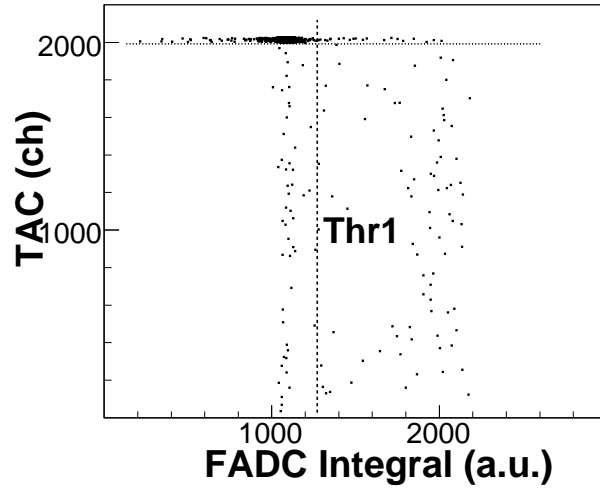


Figure 5.12.: Two dimensional spectrum of TAC versus normalized FADC Integral for first section of the ionization chamber. Non pileup events are in the fourth quadrant of the two crossing lines. The dashed line defines the pileup region on FADC Integral axis while the dotted line divides the region of TAC axis into pileup (below the line) and non pileup (above the line) events. The value of threshold Thr_1 is very similar to that in fig. 5.11.

Among three *ToF* detectors the PPPAC is located as the first one on the heavy ion path. When the ion passes through it, the ionization charge produced by the ion is collected by the wire of X and of Y detector plane. The wire that is the nearest to the ion trajectory is fired. The signal produced by the wire is delivered to the segmented, 2 ns delay per wire, delay line. There, it is split into two signals that pass to the ends of the delay line. The value of the delay of both signals contains the information as to which wire was fired. After the reconstruction procedure this information is retrieved and one can assign the coordinates (X, Y) of the ion trajectory in the detector. The third coordinate, Z, is retrieved from the position of the detector along the beam axis (Z direction). Four delay lines are connected to the wire plane X and to the wire plane Y of the PPPAC.

In the first step of the procedure we constructed two dimensional position spectra x_{1p} vs x_{2p} and y_{1p} vs y_{2p} , upper part of the fig. 5.13. These spectra represent the signals that are produced each time the heavy ion passes through the detector and that arrive to the ends of the delay lines connected to the wires of the X and Y planes. In the case of the event that corresponds to the proper detection of the position of heavy ion, the sum of x_{1p} and x_{2p} should be constant and equal to the total delay of the one segment of the delay line, the similar case is for the Y direction. Points on the spectra inside the contours C_X and C_Y of the presented figure represent such cases. Those events subsequently can be converted to the wire number by taking the difference of $x_{1p}-x_{2p}$ and $y_{1p}-y_{2p}$ for the X and Y directions respectively. The result of that conversion for one section of X and one section of Y direction is presented in the lower part of the figure. This procedure is subsequently applied for all sections of the detector. Next, taking into account the distance of 2.54 mm between wires one gets absolute pistons of detected heavy ions (fig. 5.14).

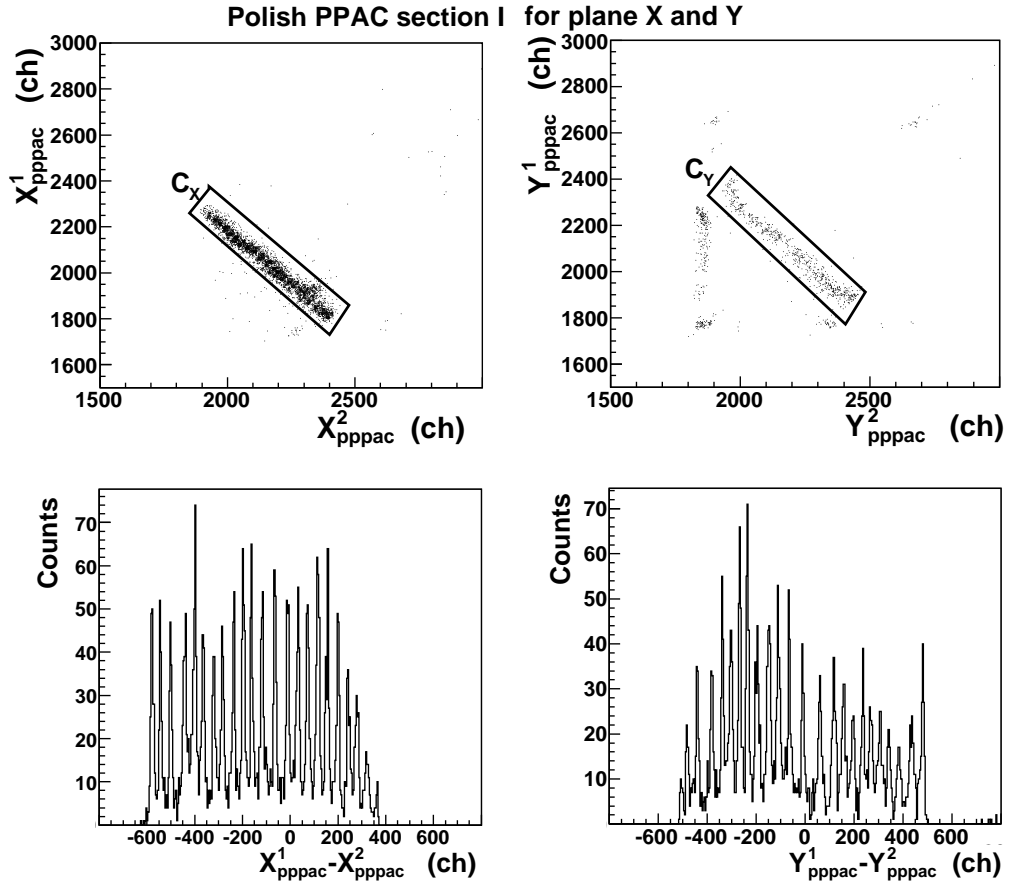


Figure 5.13.: Position spectra of heavy ions collected from the Polish PPAC. Only one section for X and Y direction is shown. In the upper part position gathered from both ends of the delay line for the X (left picture) and Y (right picture) direction are presented. The contours C_X , C_Y give a region of well defined events. The lower part shows counts for individual wires X and Y from the region marked by contours C_X , C_Y . They are received by taking the difference of the value of the signals from both ends of the corresponding (X or Y) delay lines. X_{PPAC}^1 , X_{PPAC}^2 , Y_{PPAC}^1 and Y_{PPAC}^2 are denoted in the text as x_{1p} , x_{2p} , y_{1p} and y_{2p} , respectively.

Events that are located outside the contours C_X and C_Y of the fig. 5.13 correspond mainly to the detection of light particles (they are not interesting for our experiment). Due to the low pressure of the gas (4.3 mbar) in the Polish PPAC, the ionization charge generated by light particles inside the detector is small and it may happen that this charge is not collected properly by the detector wires. The other group of events are double hits. Here two types of pileups could be identified. The first one takes place when two particles pass through the same section of X/Y. For such a double hit the sum of the delays of the signals for X or Y plane is not located in the C_X or C_Y . This sum is usually smaller than the total delay of the given segment. The second type of double hit occurs when two ions enter different sections of X and/or Y plane in the same event. To identify such cases one has to count all fired sections for plane X and Y. Those events should be rejected from the analysis.

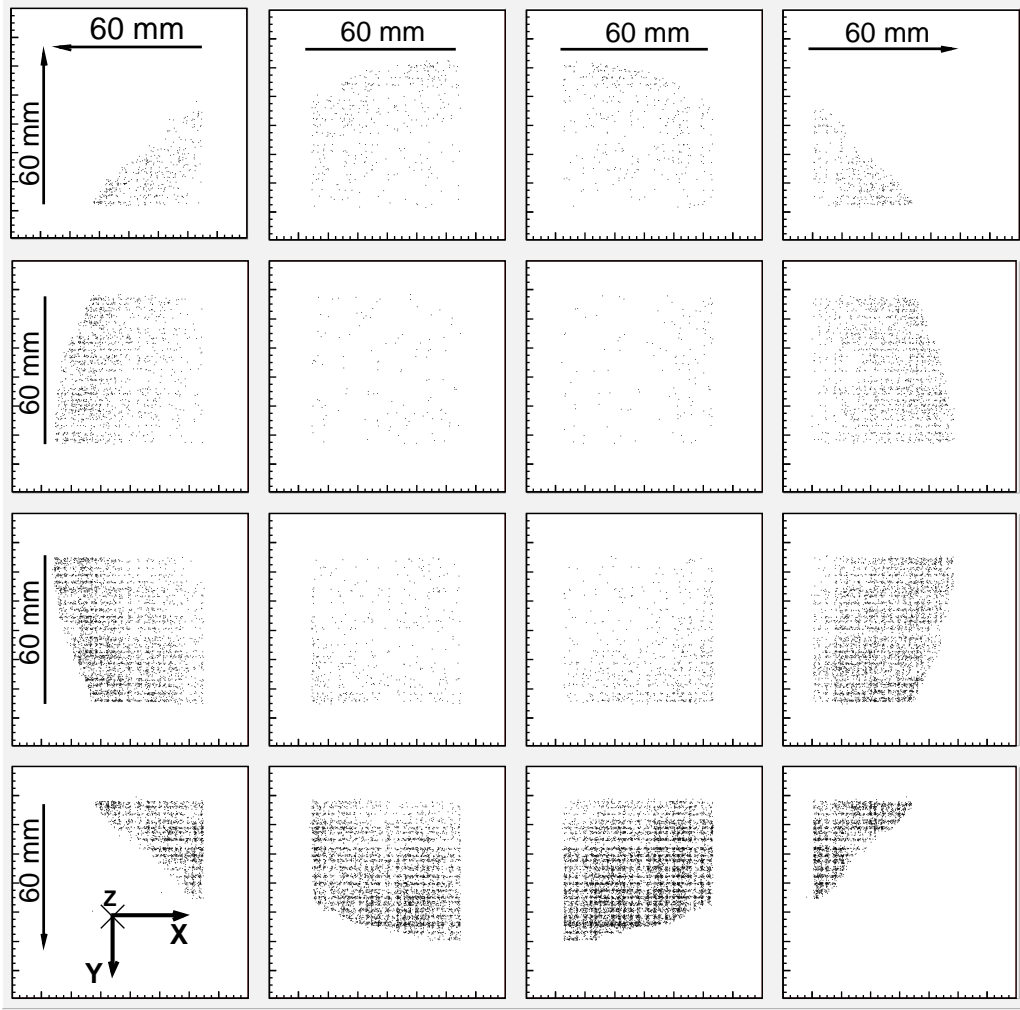


Figure 5.14.: Calibrated positions of heavy ions detected by the PPPAC detector. The figure was obtained by combining four sections of the X direction and four sections of the Y direction. The Z axis is along the beam direction. The lower part of the detector counts more events due to the beam misalignment.

Similarly, to isolate the well defined events for the other two position detectors GPPAC and MWPC we required that $x_{1g} + x_{2g} \simeq const$ and $y_{1g} + y_{2g} \simeq const$ for GPPAC as well as $x_{1m} + x_{2m} \simeq const$ and $y_{1m} + y_{2m} \simeq const$ for MWPC. Here x_{1g} and x_{2g} denote delays of signals for a wire from X plane while y_{1g} and y_{2g} are signal delays for Y wire of the GPPAC detector. The same convention applies for the MWPC counter. The sign \simeq means that the corresponding sums should be in some reasonable interval of delays usually we took around a few ns . After rejecting badly characterized events, the reconstruction of the absolute position of heavy ion in both detectors is similar as in the case of the PPPAC.

The positions of the heavy ions from all these three detectors will be used in the future analysis to reconstruct the trajectory of ions along the whole detection setup.

5.5. Search for superheavies in the $Au + Th$ reaction

In this chapter I will present the main results that were received from the analysis (still in progress) of the reaction with the beam of the $Au(7.5 A.MeV)$ ions. The ions were impinging Th target of $6.3 mg/cm^2$ thickness that was rotated 45 degree in respect to the beam direction. In such a thick target, the energy loss of the gold ions serves to spread the initial beam energy. This is necessary because we only have the approximate estimation (from the results of the previous test runs) of the optimal collision energy that should be used in peripheral reactions with Th nuclei to produce the SHE elements with relatively *low excitation energies*. The beam energy in the target is changing from the initial $7.5 A.MeV$ at the beginning of the target to the $6.3 A.MeV$ at the exit of the target. In absolute values this gives around 240 MeV range of the beam energy.

The first selection of the reaction products is accomplished with the help of 6° blocker situated after the target. The blocker serves also to stop the beam. Products that are emitted at angles greater than 6 degrees pass through the transmission detector (Italian PPAC), enter the BigSol filter and after it, the ions pass through the three ToF detectors and finally enter the IC-8 ionization chamber where they can stop or they continue to stop in one of the wall's of the scintillators.

To obtain the identification of the heavy reaction products we primarily use the velocity/the time of flight from the ToF detectors (e.g. ToF_{GM}) and the energy losses of heavy ions (HI) measured in the segmented ionization chamber IC-8. Depending on the velocity of the heavy ions that enter the IC-8, the chamber works as an E or ΔE detector. For times of flight greater than $\sim 50 ns$ (low velocity) heavy ions are stopped inside the ionization chamber and, in that case, the IC-8 measures the residual energy (E) of the heavy ions while for ToF 's smaller than $50 ns$ (high velocity) heavy ion pass through the IC and the IC becomes a ΔE detector. Even if it works in the ΔE regime the chamber still retains the major part of the residual energy of heavy ions.

Fig. 5.15a presents the sum of energy losses ($\sum \Delta E_i, i = 1, \dots, 8$) of heavy ions in the IC-8 versus time of flight between GPPAC and the MWPC (ToF_{GM}). The data presented in the figure are collected requiring that the heavy ion is properly detected in the GPPAC and MWPC detectors. This means that the positions of the HI are well defined in both detectors (see chapter 5.4.4 for the definition of well defined position). Several groups of events can be identified here. The thick banana-like groups of events correspond to the detection of Au -like ions. Transfer reactions in collision of the Au with the Th nucleus have a large cross section and due to this, the products of such transfers are still abundant at the end of the detection line, despite the selection made by the BigSol filter and the 6° blocker. It is manifested by the events that are located on the left of the banana and they extend to the lowest energies $\sum \Delta E_i$. Of course, those events correspond to the detection of ions lighter ($Z < 79$) than the gold nuclei. Here different kinds of heavy ions should be located. Although it is not possible to identify those products according to their atomic number, nevertheless one can expect here, the fragments of the fission of Th nuclei and also deep inelastic reaction products. The events located at the bottom part are the light charged particles, mainly protons, alphas, etc.

The region of the very heavy ions is on the right of the group of the beam-like

5. Superheavy elements studies at TAMU

ions. Indeed, in this region there are many events but one should be very cautious to assign them to the detection of very heavy ions. In fact, most of those events are pileups. For example, no one can expect that the signals which correspond to $\sum \Delta E_i > 300 \text{ MeV}$ and $ToF_{GM} > 80 \text{ ns}$ (the most right part of the fig. 5.15a) were generated by single ions. They are mainly a mixture of signals that originate from two different heavy ions registered by the acquisition as one event. For example the lighter ion comes earlier and gives a stop signal in the GPPAC while it is missed by the MWPC detector, next the heavier ion (e.g. *Au*-like) that comes late initiates a start signal in the MWPC and is detected in the ionization chamber.

In this scenario one obtains events with high energies in the IC-8 and large time of flights.

Our objective in the data analysis was to find suitable selections to isolate real events that correspond to the detection of ions heavier than the *Au* nuclei. To realize this objective several selections were applied. First, we used the electronic anti-pileup system, described in section 5.10, to eliminate events in which two heavy ions gave signals in the MWPC. This type of pileup is also seen in the IC-8 chamber if one looks at the pulse shape recorded by the FADC. Simply, two pulses that are separated or partially overlapped are seen in such a case. Depending on how fast the two ions lose their energy in the IC-8 these two pulses can be present in all or in some segments of the ionization chamber. The time in the anti-pileup system was set to eliminate double hits in the MWPC if ions enter it in a time interval shorter than $8 \mu\text{s}$ while the FADC time window was set to the $10 \mu\text{s}$. In the case when the second ion enters, in one event, the ionization chamber after the time greater than $8 \mu\text{s}$, this ion is always seen in the FADC as a pulse well separated from the pulse generated by the first ion and the separation distance is at least a few μs . Now, considering that the *ToF* measurements are in the time range of about 250 ns , it is then clear that this double hit can be easily unfolded and proper information can be extracted for the first ion.

By applying the above anti-pileup selections and the condition on the well defined positions in the GPPAC and the MWPC counters the fig. 5.15b is received. As one can see significant reduction of events, as compared with panel a), located in the region where very heavy nuclei are expected is observed, but still not all events from that region can be assigned to the detection of the real superheavy ions. There must be some part of events that contain mixed information from two different heavy ions, e.g. *ToF* is measured for one ion and the energy loss in the IC-8 for the other. To justify this statement one can recall the argument that events with large energy losses ($\sum \Delta E_i > 300 \text{ MeV}$) and large *ToFs* ($ToF_{GM} > 80 \text{ ns}$) are not realistic. At this stage we can not distinguish which one corresponds to the real SHE ions.

Next, to isolate those events that correspond to the detection of very heavy fragments we required that the energy loss of a particle in one of the segments of the ionization chamber should be larger than 75 MeV (using energy calibration of the IC based on the Orsay tables). Such a requirement is a phenomenological one, but from the calculation of the Orsay code (SRIM is not able to calculate energy loss of ions that have $Z > 92$) one can expect that the very heavy ions are losing quite large energy in some segments of the IC, at least 75 MeV . The result that corresponds to this requirement is presented in panel c) of fig. 5.15. It should be mentioned that this selection is strongly restrictive. As we see from the figure now there are

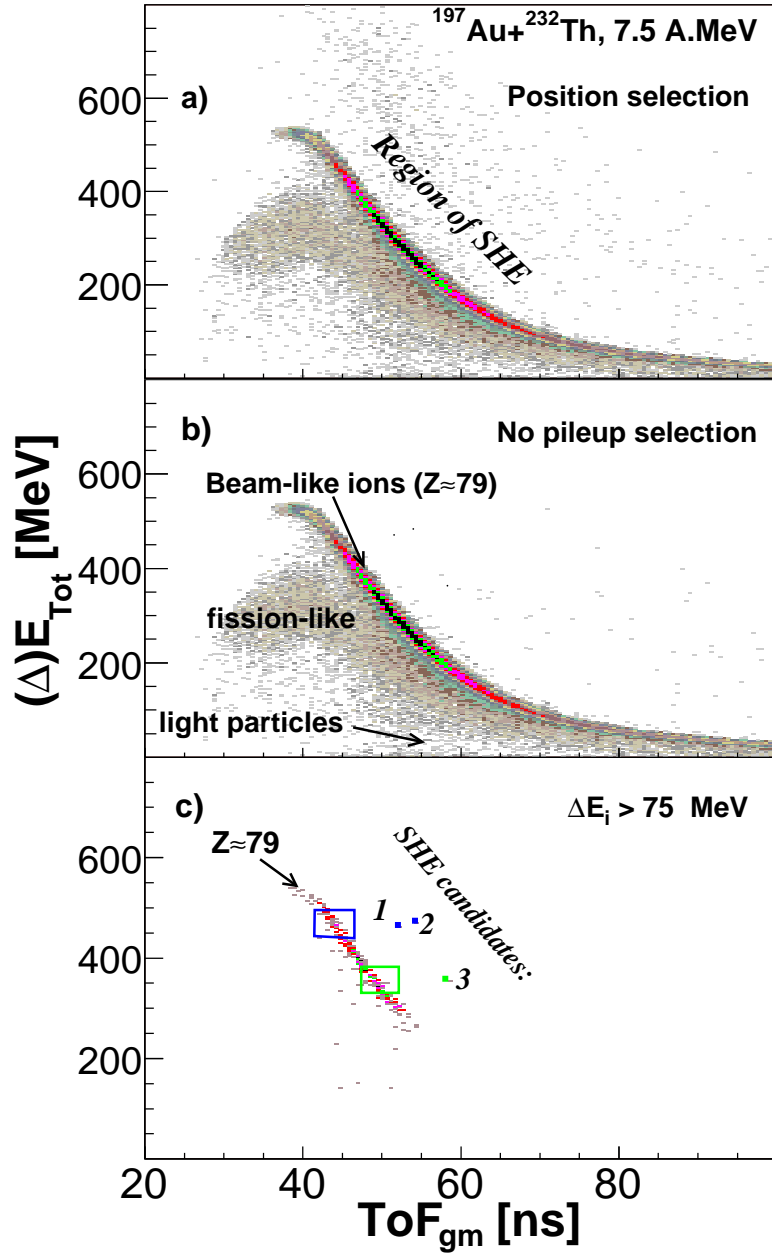


Figure 5.15.: Total energy loss ($\sum \Delta E_i, i = 1, \dots, 8$) in the ionization chamber of detected heavy ions versus their ToF_{GM} (GPPAC - MWPC). a) represents events when the heavy ions deliver proper position signals in the ToF detectors: GPPAC and MWPC, b) requirement that no pileup (see sec. 5.4.3 for pileup rejection) is present was added, c) additionally, we required that the ΔE_i of the detected heavy ion in one of the segments of the IC-8 is greater than $75 MeV$. In c) three events are isolated in the region of the expected SHE nuclei. Characteristic groups of events are marked in panel a) and b). For more detailed discussion of the figure see text.

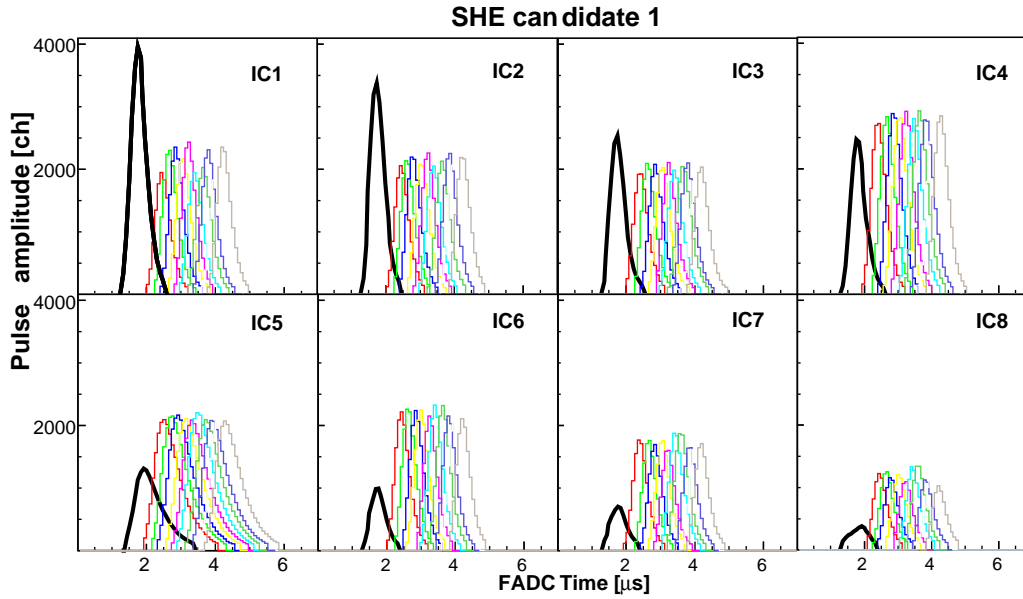


Figure 5.16.: Pulse shapes iCalibrated positions of heavy ions detected by the PPPAC detector. The figure was consecutive segments of the ionization chamber (IC-8). Thick black line represents pulse shape of the **SHE candidate no. 1** from fig. 5.15c. For comparison, pulse shapes of 10 randomly chosen events from the blue contour of fig. 5.15c are shown. They correspond to the beam-like ions (*Au*-like) - one colour marks the pulse shape of one *Au*-like nucleus.

only three events located in the SHE region. From the empirical extrapolation to atomic numbers higher than $Z=92$ [68] (SRIM calculation applied) one can estimate that those three superheavy candidates should have atomic numbers in the range of $Z=100-110$.

Now, the SHE candidates will be analyzed in more details. First of all, one should examine the pulse shapes recorded by flash ADC (FADC) from different segments of the IC-8 for those three cases. These pulses, for all segments of the ionization chamber, are presented in figs. 5.16, 5.17 and 5.18 as thick black lines. The amplitude of the pulses is decreasing in the consecutive sections of the IC chamber to become close to zero in the last segment. These candidates are practically stopped in the chamber. For comparison, the pulse shape behaviour of the beam-like ions is also shown in the figure. I have drawn the pulse shapes of 10 ions that were randomly chosen from two different energy loss regions of the beam-like particles. In the case of candidates 1 and 2 (figs. 5.16, 5.17) the region that was taken to get the pulse shapes of the *Au*-like nuclei is marked as a blue contour in fig. 5.15. In the case of the SHE candidate no. 3 (fig. 5.18) this region was selected by the green contour of that figure. An important observation can be made. We see that the candidates lose their energy in the ionization chamber much faster than the *Au* ions and their pulse shape amplitude in the first segments of the IC-8 is much higher than this of the *Au* ions. It means one can rather exclude the possibility that those candidates are a result of mixed events. Such a mixing could emerge if the beam-like ion, from the corresponding energy loss region (contour blue or green), is detected in the IC-8

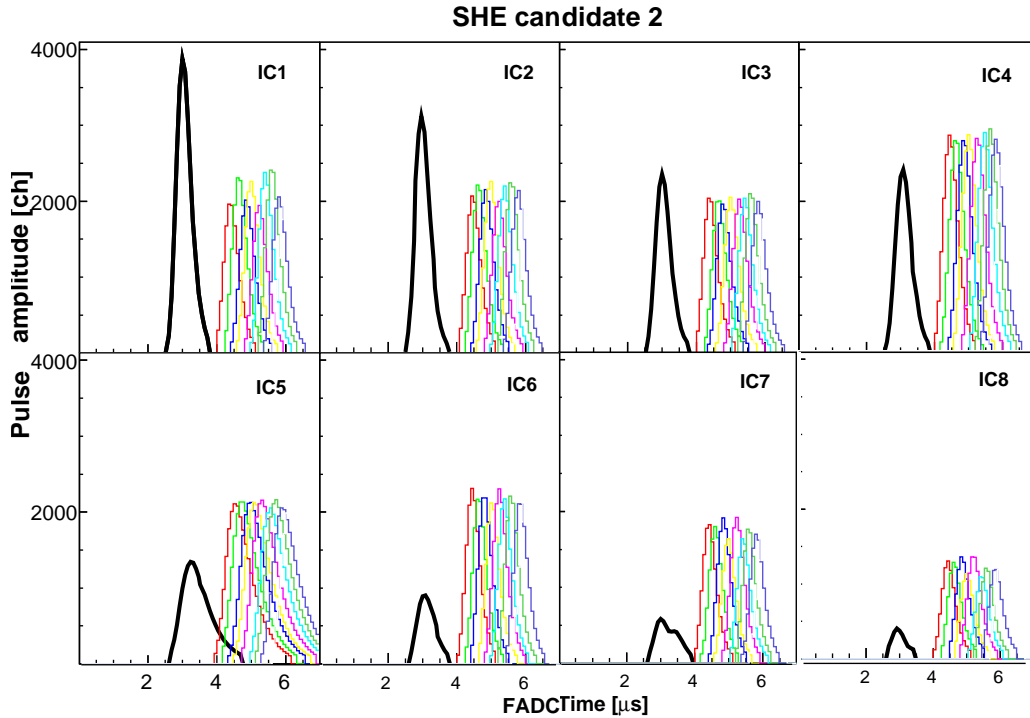


Figure 5.17.: Pulse shapes in consecutive segments of the ionization chamber (IC-8). Thick black line represents pulse shape of the **SHE candidate no. 2** from fig. 5.15c. For comparison, pulse shapes of 10 randomly chosen events from the blue contour of fig. 5.15c are shown. They correspond to the beam-like ions (*Au*-like) - one colour marks the pulse shape of one *Au*-like nucleus.

while the *ToF* is measured for the other, e.g. the light particle that came first but was stopped in the GPPAC.

The next check, the candidates support the hypothesis that they represent SHE/very heavy elements, was performed by comparing the measured velocity between the Polish PPAC (PPPAC) and the GPPAC (v_{PG} is calculated using the ToF_{PG}) and the velocity between the GPPAC and the MWPC (v_{GM} is calculated using the ToF_{GM}). The following values were received: $v_{PG} = 2.26$, $v_{GM} = 2.03$ *cm/ns*; $v_{PG} = 2.18$, $v_{GM} = 1.95$ *cm/ns*; $v_{PG} = 1.96$, $v_{GM} = 1.80$ *cm/ns* for the candidate 1, 2 and 3 respectively. The important observation is, that in all three cases $v_{PG} > v_{GM}$. It should be so if those events correspond to the detection of single ions as the ions lose some energy in the middle *ToF* detector (GPPAC).

One should also consider a possibility that those events are some artifacts, although these candidates passed all the tests we could apply at this stage of analysis.

The following scenario can be imagined to produce such artificial events. Let us assume there are two different particles, A_1 and A_2 . A_1 is, say 55 *ns* (this is the beam burst time distance) earlier than A_2 when it reaches the trigger detector MWPC. Now, suppose that the CFD (Constant Fraction Discriminator) of the MWPC is vetoed by a computer BUSY signal from the previous event and so the CFD does not generate a trigger for particle A_1 , though Polish PPAC and GPPAC CFDs generate signals for that particle. When A_2 arrived at MWPC, BUSY is over and CFD is

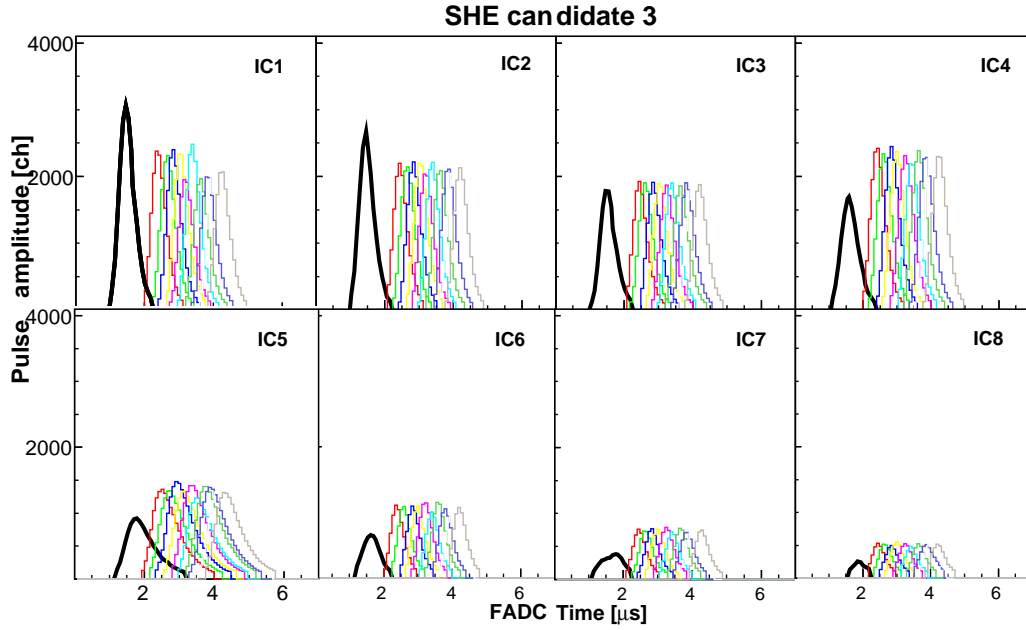


Figure 5.18.: Pulse shapes in consecutive segments of the ionization chamber (IC-8). Thick black line represents pulse shape of the **SHE candidate no. 3** from fig. 5.15c. For comparison, pulse shapes of 10 randomly chosen events from the green contour of fig. 5.15c are shown. They correspond to the beam-like ions (*Au*-like) - one colour marks the pulse shape of one *Au*-like nucleus.

fired and generate a trigger. In this case start for TDC is given by A_2 and stop by A_1 , so both $ToFs$ are wrong. In other words, the BUSY signal produces the time window that the pileup event is sneaked into "real event". Now we can recall figs. 5.16-5.18 that show the pulse height distribution in each segment of the IC-8 for interesting events and beam-like events. The pulse heights for the interesting events (cases 1-3) have much larger values than the beam-like ones and also their decrease rate is larger. This means that if those three candidates are some artifacts, the IC signals of those candidates have to be produced by two particles A_1 and A_2 , (otherwise signals of candidates should be similar to those of beam-like ions). In order to pass through the pulse shape analysis in the IC and the position sum for x and y direction in the GPPAC and the MWPC, the track of A_1 and A_2 has to be very close. As pulse shape check can distinguish more than 100 ns, the vertical position difference of these tracks in the ionization chamber should be less than 1 mm since the electron drift time in the IC is an order of $1\mu s/cm$. In order to pass through the position check, the vertical and horizontal difference should be smaller than 3 mm (less than 3 wires in GPPAC and MWPC). The probability of such events seems to be extremely small. But in fact, it should be even smaller because also the measured velocities v_{PG} , v_{PG} for the interesting events are consistent with the hypothesis of the single ion detection. Our statistics contains 4 million events. In the summary, the following arguments support the hypothesis that we detected three very heavy ions:

- pulse shapes distribution in the IC-8 is very different from that of the beam-like

ions: much higher amplitude in the first segments of the IC and the decrease rate is also much higher than those of beam-like ions,

- measured velocities between PPPAC-GPPAC and between GPPAC-MWPC are consistent with the detection of a single ion in the event ,
- the FWHM of the pulse shape is also consistent with the hypotheses that a single ion was detected in each of those three events because the beam-like particles have very similar FWHM as one can see from figs. 5.16-5.18.

The next section will summarize the present status of that experiment and will give some ideas on the future of that collaboration.

5.6. Further analysis and future of the Texas A&M experiments

It should be stressed that the results presented in the last few sections (experiment $Au + Th$) are preliminary. Data analysis is still in progress, especially as we want to determine with better precision the atomic number (Z) of detected elements that are heavier than Au nuclei. To perform this, new extrapolation method, proposed by one of the member group, [68] will be applied. With this new method one expects to obtain the estimation of Z for detected heavy ions with the accuracy of $\pm 3 Z$.

It has also to be mentioned that only part of the available data were used in the analysis that aimed to find candidates for very heavy elements. This is because the signal gains from some detectors (e.g. IC-8) of the experimental setup were not constant during the whole experiment. In the next step we have to check carefully these gains over all runs and renormalize them to one common gain for each of the IC-8 segments before all data can be used in search for other candidates of superheavy elements.

Another point concerns heavy ions time of flight (ToF_{IM}) calibration for the detector pair: IPPAC and MWPC. The IPPAC is situated just before the BigSol filter. Because of this, part of the heavy ion trajectory along the distance from the IPPAC to the end of BigSol is not straightforward. The heavy ion passes through the magnetic field of the BigSol along a spiral trajectory. To obtain the real distance traveled by the heavy ion from the IPPAC to the MWPC calculations are needed that take into account the geometry of the BigSol magnetic field. With the long base of $\simeq 6$ m, offered by these two detectors, it will be possible to significantly increase the accuracy of the measurements of one of the key variables in this experiment. This is the velocity of the heavy reaction product.

Besides, further data analysis will take into account processing of signals from the FADCs that were connected to the time of flight detectors: MWPC, GPPAC and PPPAC⁴. This analysis may refine the rejection procedure for the pileup events which is one of the main concern in our measurement.

This research is planned to be continued at the Texas A&M University. The emphasis will be placed on a more accurate calibration of heavy ion energy losses

⁴These flash ADCs were applied in the later stage of the experiment, but the statistics collected while they were working is still reasonable - it is several millions of events.

5. Superheavy elements studies at TAMU

in the ionization chamber (IC-8). Therefore, U direct beams with a wider range of energy beams will be used. We will further work to improve the detection setup to eliminate more precisely double hit events. One can also expect to achieve a lower background and to use, instead of YAP detectors, the silicon position detector to eventually observe radioactive decay (α or SF) of the implanted SHE.

We also plan to confront the data with a model that is presently being developed in the HMDF of the M. Smoluchowski Institute of Physics. We expect that the comparison of the present data with the model predictions will help us to optimize the beam energy of Au ions in future measurements. These calculations can also envisage new reactions to produce the SHE elements with the present method (fission of target and subsequent fusion of one of fragments with beam ion).

In summary, we isolated three well documented events that can be assigned to the production of nuclei with the atomic number in the range of $Z=100-110$ with a cross section on the level of nb . This is an important result as it shows that our experimental apparatus is capable to isolate and detect very heavy nuclei when they are produced.

6. Summary and discussion

The objective for the SHE studies is to discover the island of nuclear stability what will confirm the new magic numbers in the structure of the nuclei.

In this work two types of experimental approach in superheavy element search were described and the results of these experiments were presented. In the first approach, the experimental search for SHE uses α -decay chains and/or spontaneous fission from radioactive superheavy residues implanted in the X-Y position Si detectors to unambiguously identify the atomic and mass number of the nucleus. This technique, as was shown in the work, ensures the proper identification of SHE. The drawback of such an approach is the extremely low fusion cross section for the production of superheavy nuclei. The last discovery of $Z=118$ estimates the fusion cross section on the level of 0.2 pb . On the other hand, the TAMU program for SHE production is based on the innovative idea which assumes that one of the fission fragments of a fissile target can be a very attractive partner for the beam nucleus and can both form a super- or hyper-heavy system. Although the cross section for such a process is not known it can turn out that this phenomena can be more probable than the cold/hot fusion processes used to produce SHE elements so far. In such a case this technique can change the experimental progress on SHE discoveries. This technique is a new one and requires further improvements of the detection setup. The analysis of the data from the latest September 2006 experiment is still in progress.

In the first experimental approach to reach the region of more stable (island of stability) superheavy nuclei it is necessary to obtain neutron rich beams or neutron rich targets. What is more, due to a very low cross section for SHE production by fusion, such radioactive beams should have intensities comparable to presently accessible beams of stable nuclei. In the TAMU experiments we do not need radioactive neutron rich beams. One can say that in this method "Nature decides and delivers, in the collision of beam nucleus with target nucleus, the most optimal configuration fission fragment - the beam nucleus to form the SHE".

Presently, several laboratories have begun to build radioactive high intensity beams. One such project is SPIRAL2 at the GANIL center. For this project a new linear accelerator LINAG is being constructed. This accelerator will not only deliver stable beams of light ions for radioactive beams, but also beams of heavy stable ions. These beams will have an extremely high intensity, for certain ions this intensity will be a factor 100 higher than presently accessible. Such high intensities will provide a unique possibility for a more detailed study of presently discovered SHE. The new dedicated, for working with LINAG, Super Separator Spectrometer (S^3) is expected to continue the study of SHE properties. This spectrometer is planned to possess extremely good parameters such as the rejection ratio and focusing of reaction products. The S^3 should start to operate in 2011-12.

6.1. Acknowledgements

I would like to thank all my collaborators with whom I had worked during the realisation of this project. Among them I should mention professor Jean Petér from LPC-ISMRA Caen for his continuous support in all matters concerning the constructed detectors and his hospitality during my stays at LPC-ISMRA. I would also like to extend my gratitude to professor Zbigniew Majka who was one of the first person that appreciated the new experimental approach in the SHE quest and enabled me to take an active part in the experiments based on this method. His support in detector construction is also very much appreciated. My appreciation for the group of professor Joseph B. Natowitz from the Cyclotron Institute of Texas A&M University is especially great. During the SHE experiments, I had an opportunity to work with physicists of this group and they presented the highest level of professionalism and a lot of invention to always find a way (e.g. modifying electronics, detection setup) to improve the quality of the collected data while attacking not easy problem that is the SHE production. To doctor Zbigniew Sosin goes my special thanks for the many years we have worked together and for his creativity and ideas which have always impressed me very much. I also wish to thank the management of the LPC-ISMRA laboratory. Last but not least I would like to thank the engineers, Mr. Marek Adamczyk, and Mr. Tadeusz Barczyk, for their efforts and tremendous work during the construction of the detectors and the electronics which were dedicated to these experiments.

This work was supported, in part, by the Polish State Committee for Scientific Research (KBN), Grant no. PB 3336/H03/2007/32.

Bibliography

- [1] E. M. McMillan, P. H. Abelson, *Phys. Rev.* 57 (1940) 1185.
- [2] G. T. Seaborg, E. M. McMillan, J. W. Kennedy, A. C. Wahl, *Phys. Rev.* 69 (1946) 366.
- [3] W. D. Myers, W. J. Świątecki, *Nucl. Phys.* 81 (1966) 1.
- [4] A. Sobiczewski, F. A. Gareev, B. N. Kalinkin, *Phys. Lett.* 22 (1966) 500.
- [5] S. Hofmann et al., *Eur. Phys. J. A14* (2002) 147.
- [6] S. Hofmann, G. Münzenberg, *Rev. Mod. Phys.* 75 (2000) 733.
- [7] H. Hofmann, R. Samhammer, G. Ockenfuss, *Nucl. Phys.* A496 (1989) 269.
- [8] S. Hofmann, V. Ninov, F. P. Heßberger, P. Armbruster, H. Fogler, G. Münzenberg, H.-J. Schött, A. G. Popeko, A. V. Yeremin, A. N. Andreev, S. Saro, R. Janik, M. E. Leino, *Z. Phys.* A350 (1995) 281.
- [9] S. Hofmann, V. Ninov, F. P. Heßberger, P. Armbruster, H. Fogler, G. Münzenberg, H.-J. Schött, A. G. Popeko, A. V. Yeremin, S. Saro, R. Janik, M. E. Leino, *Z. Phys.* A354 (1996) 229.
- [10] Y. Oganessian, *Jour. Nucl. Rad. Sci.* 3 (2002) 5.
- [11] Y. Oganessian et al., *JINR Preprints and Communications*, Dubna, D7-2002-287, 2002.
- [12] Y. Oganessian et al., *LNL Report*, Berkeley, UCRL-ID-151619, 2003.
- [13] Y. Oganessian et al., *Phys. Rev.* C74 (2006) 044602.
- [14] Y. Oganessian et al., *Phys. Rev.* C63 (2001) 011301R.
- [15] J. Błocki, Y. Boneh, J. R. Nix, J. Randrup, M. Robel, A. J. Sierk, W. J. Świątecki, *Ann. Phys.* 113 (1978) 330.
- [16] N. V. Antonenko, E. A. Cherepanov, A. K. Nasirov, V. P. Permjakov, V. V. Volkov, *Phys. Lett.* B319 (1993) 425.
- [17] A. Sobiczewski, K. Pomorski, *Prog. Part. Nucl. Phys.* 58 (2007) 292.
- [18] G. Münzenberg, S. Hofmann, H. Folger, F. P. Heßberger, J. Keller, K. Poppensieker, B. Quint, W. Reisdorf, K. H. Schmidt, H. J. Schött, P. Armbruster, M. E. Leino, R. Hingmann, *Z. Phys.* A322 (1985) 227.

Bibliography

- [19] G. Münzenberg, P. Armbruster, G. Berthes, H. Folger, F. P. Heßberger, S. Hofmann, J. Keller, K. Poppensieker, B. Quint, W. Reisdorf, K. H. Schmidt, H. J. Schött, K. Summerer, I. Zychor, M. E. Leino, R. Hingmann, U. Gollerthan, E. Hanelt, *Z. Phys.* A328 (1987) 49.
- [20] N. Bohr, J. Wheeler, *Phys. Rev.* 56 (1939) 426.
- [21] S. Bjornholm, J. Linn, *Rev. Mod. Phys.* 62 (1980) 725.
- [22] Y. T. Oganessian, A. G. Demin, A. S. Iljinov, S. P. Tretyakova, A. A. Pleve, Y. E. Penionzhkevich, V. P. Ivanov, Y. P. Tretyakov, *Nucl. Phys.* A239 (1975) 157.
- [23] V. M. Strutinsky, *Nucl. Phys.* A95 (1967) 420.
- [24] V. M. Strutinsky, *Nucl. Phys.* A122 (1968) 1.
- [25] M. Brack, J. Damgaard, A. S. Jensen, H. C. Pauli, V. M. Strutinsky, C. Y. Wong, *Rev. Mod. Phys.* 44 (1972) 320.
- [26] Z. Patyk, A. Sobiczewski, *Nucl. Phys.* A533 (1991) 132.
- [27] R. Smolańczuk, *Phys. Rev.* C56 (1997) 812.
- [28] P. Möller, J. R. Nix, *J. Phys.* G20 (1994) 1681.
- [29] in: W. Greiner, R. K. Gupta (Eds.), *Heavy Elements and Related New Phenomena*, World Scientific, Singapore, 1999, p. 1 Part I.
- [30] Y. T. Oganessian, *Lecture Notes in Physics* 33 (1974) 221, Springer, Heidelberg.
- [31] M. Nurmia, I. Sikkeland, R. Silva, A. Ghiorso, *Phys. Lett.* B26 (1967) 78.
- [32] Y. Oganessian, Manne Siegbahn Memorial Lecture given on 12 October 1999 in Stockholm .
- [33] F. P. Heßberger, G. Münzenberg, S. Hofmann, W. Reisdorf, K. H. Schmidt, H. J. Schött, P. Armbruster, R. Hingmann, B. Thuma, D. Vermeulen, *Z. Phys.* A321 (1985) 317.
- [34] P. Armbruster, *Ann. Rev. Nucl. Part. Sci.* 35 (1985) 135.
- [35] G. Münzenberg, *Rep. Progr. Phys.* 51 (1988) 57.
- [36] W. J. Świątecki, *Nucl. Phys.* A376 (1982) 275.
- [37] J. Błocki, H. Feldmayer, W. J. Świątecki, *Nucl. Phys.* A459 (1986) 145.
- [38] A. V. Yeremin, A. N. Andreyev, D. D. Bogdanov, V. I. Chepigin, V. A. Gorschkov, A. I. Ivanenko, A. P. Kabachenko, L. A. Rubinskaya, E. M. Smirnova, S. V. Stepantsov, E. N. Voronkov, M. Terakopian, *Nucl. Instrum. Meth.* A274 (1989) 528.
- [39] J. Péter, *Eur. Phys. J. A* 22 (2004) 271.

- [40] S. Grévy, for FULIS collaboration: N. Alamanos, N. Amar, J. C. Angélique, R. Anne, G. Auger, F. Becker, R. Dayras, A. Drouart, J. M. Fontbonne, A. Gillibert, D. Guerreau, F. Hanappe, R. Hue, A. S. Lalleman, T. Legou, R. Lichtenthäler, E. Liénard, W. Mittig, F. D. Oliveira, N. Orr, G. Politi, Z. Sosin, M. G. Saint-Laurent, J. C. Steckmeyer, C. Stodel, J. Tillier, R. de Turreil, A. C. C. Villari, J. P. Wieleczko, A. Wieloch, *Jour. Nucl. Rad. Sci.* 3 (1) (2002) 9.
- [41] C. Stodel, N. Alamanos, N. Amar, J. C. Angélique, R. Anne, G. Auger, J. M. Casandjian, R. Dayras, A. Drouart, J. M. Fontbonne, A. Gillibert, S. Grévy, D. Guerreau, F. Hanappe, R. Hue, A. S. Lalleman, N. Lecesne, T. Legou, M. Lewitowicz, R. Lichtenthaler, E. Lienard, L. Maunoury, W. Mittig, N. Orr, J. Péter, E. Plagnol, G. Politi, M. G. Saint-Laurent, J. C. Steckmeyer, J. Tillier, R. de Turreil, A. C. C. Villari, J. P. Wieleczko, A. Wieloch, in: *American Institute of Physics Conference Proceedings*, Vol. 561, 2001, p. 344.
- [42] F. Méot, S. Valéro, Simulation code zgouby., SATURNE Note LNS/GT93-12.
- [43] V. Ninov, K. E. Gregorich, W. Loveland, A. Ghiorso, D. C. Hoffman, D. M. Lee, H. Nitsche, W. J. Świątecki, U. W. Kirbach, C. A. Laue, J. L. Adams, J. B. Patin, D. A. Shaughnessy, D. A. Strellis, P. A. Wilk, *Phys. Rev. Lett.* 83 (1999) 1104.
- [44] S. Hofmann, in: B. Rubio, M. Lozano, W. Gelletly (Eds.), *Int. Conf. Experimental Nuclear Physics in Europe Facing the Next Millenium*, Vol. 495, AIP Conference Proceedings, Sevilla, Spain, 1999, pp. 137–144.
- [45] V. Ninov, K. E. Gregorich, W. Loveland, A. Ghiorso, D. C. Hoffman, D. M. Lee, H. Nitsche, W. J. Świątecki, U. W. Kirbach, C. A. Laue, J. L. Adams, J. B. Patin, D. A. Shaughnessy, D. A. Strellis, P. A. Wilk, *Phys. Rev. Lett.* 89 (2002) 039901.
- [46] C. Stodel, R. Anne, G. Auger, B. Bouriquet, J. M. Casandjian, R. Cee, G. D. France, F. D. Santos, R. D. Turreil, A. Khouaja, A. Péghaire, M. G. Saint-Laurent, A. C. C. Villari, J. P. Wieleczko, N. Amar, S. Grévy, J. Peter, R. Dayras, A. Drouart, A. Gillibert, C. Theisen, A. Chatillon, E. Clement, K. Łojek, Z. Sosin, A. Wieloch, K. Hauschild, F. Hannachi, A. Lopez-Martens, L. Stuttge, F. P. Hessberger, S. Hofmann, R. Lichtenthäler, F. Hanappe, in: Y. Penionzhkievich, E. Cherepanov (Eds.), *Proc. Int. Symp. on Exotic Nuclei, EXON2004,5-12 July, 2004*, World Scientific, EXON, Peterhof, Russia, <http://www.jinr.ru/exon2006/exon2004.pdf>, 2005, p. 180.
- [47] S. Hofmann et al., *Nucl. Phys.* A734 (2004) 93.
- [48] A. Wieloch, Z. Sosin, J. Péter, K. Łojek, N. Alamanos, N. Amar, R. Anne, J. C. Angélique, G. Auger, R. Dayras, A. Drouart, J. M. Fontbonne, A. Gillibert, S. Grévy, F. Hanappe, F. Hannachi, R. Hue, A. Khouaja, T. Legou, A. Lopez-Martens, E. Liénard, L. Manduci, F. de Oliveira Santos, N. Orr, G. Politi, M. G. Saint-Laurent, C. Stodel, L. Stuttg, J. Tillier, R. de Turreil, A. C. C. Villari, J. P. Wieleczko, *Nucl. Inst. Meth.* A517 (2004) 364, FULIS Collaboration.

- [49] W. Morawek et al., *Z. Phys.* A341 (1991) 75.
- [50] S. K. Patra et al., *Nucl. Phys.* A651 (1999) 117.
- [51] V. S. Nikolaev, I. S. Dimitriev, *Phys. Lett.* 28A (1968) 277.
- [52] K. Shima et al., *Phys. Rev.* A40 (1989) 3557.
- [53] K. Shima et al., *At. Data and Nucl. Data Tables* 51.
- [54] R. N. Sagaiduk, A. V. Yeremin, *Nucl. Ins. Meth.* B93 (1994) 103.
- [55] J. Péter, N. Alamanos, N. Amar, J. C. Angelique, R. Anne, G. Auger, F. Becker, R. Dayras, A. Drouart, J. M. Fontbonne, A. Gillibert, S. Grevy, D. Guerreau, F. Hanappe, R. Hue, R. Lalleman, N. Lecesne, T. Legou, M. Lewitowicz, R. Lichtenthaler, E. Lienard, W. Mittig, F. D. Oliveira, N. Orr, G. Politi, Z. Sosin, M. G. Saint-Laurent, J. C. Steckmeyer, C. Stodel, J. Tillier, R. D. Tournail, A. C. C. Villari, J. P. Wieleczo, A. Wieloch, in: G. Fazio, G. Giardina, F. Hanappe, G. Imme, N. Rowley (Eds.), *Nuclear Physics et Border Lines*, World Scientific, Lipari (Italy), 2002, pp. 257–266.
- [56] Z. Sosin, A. Wieloch, J. Peter et al., Gas-Scintillation counter for detection of SHE elements. in preparation.
- [57] K. H. Schmidt, *Eur. Phys. J.* A8 (2000) 141.
- [58] K. H. Schmidt, C. C. Sahm, K. Pielenz, H. G. Clerc, *Z. Phys.* A316 (1984) 19.
- [59] Y. Oganessian et al., *Phys. Rev.* C69 (2004) 021601.
- [60] T. Materna, S. Kowalski, K. Hagel, J. B. Natowitz, G. A. Souliotis, R. Wada, J. Wang, A. S. Botvina, S. Moretto, D. Fabris, M. Lunardon, S. Pesente, V. Rizzi, G. Viesti, M. Barbui, M. Cinausero, G. Prete, F. Becchetti, H. Griffin, H. Jiang, T. O'Donnell, Z. Majka, in: *Progress in Research April 1, 2003-March 31, 2004*, Cyclotron Institute Staff, Texas A&M University, College Station, TX 77843-3366, 2004, pp. II–17, <http://cyclotron.tamu.edu/publications.html>.
- [61] G. A. Souliotis, G. J. Derrig, G. J. Kim, F. P. Abegglen, G. Chubarian, K. Hagel, R. Wada, J. Natowitz, G. Prete, G. Viesti, A. Kekis, D. Schetty, M. Veselsky, S. J. Yennello, in: *Progress Reports April 1, 2001-March 31, 2002*, Cyclotron Institute Staff, Texas A&M University, College Station, TX 77843-3366, 2002, pp. V–19, <http://cyclotron.tamu.edu/publications.html>.
- [62] M. Barbui, M. Cinausero, G. Prete, V. Rizzi, D. Fabris, M. Lunardon, S. Moretto, G. Nebbia, S. Pesente, G. Viesti, J. B. Natowitz, K. Hagel, G. S. B. Stein, T. Materna, S. Kowalski, L. Qin, R. Wada, J. Wang, G. Chubaryan, in: *Annual Report, LNL-INFN (REP)-202/2004*, ISBN 88-7337-004-7, 2003, pp. 32, http://www.lnl.infn.it/~annrep/read_an/2003/contrib_2003/pdfs/A076S.pdf.
- [63] M. Moszyński et al., *Methods Phys. Res.* A404 (1998) 159.
- [64] J. Colin, D. Cussol, J. Normand et al., Dynamical effects in multifragmentation at intermediate energies., *nucl-ex/0304012*, INDRA collaboration.

- [65] J. F. Ziegler, J. P. Biersack, U. Littmark, *The Stopping and Range of Ions in Solids.*, Vol. 1, Pergamon Press, 1985.
- [66] J. F. Ziegler, *Particle Interactions with Matter*, <http://www.srim.org>.
- [67] F. Hubert et al., *Nucl. Inst. Meth. B36* (1989) 357.
- [68] P. Sahu, J. B. Natowitz, Private communication .
- [69] G. T. Seaborg, R. A. James, L. O. Morgan, U. S. Department of Energy Report no. AECD-2185, 1948.
- [70] G. T. Seaborg, R. A. James, A. Ghiorso, U. S. Department of Energy Report no. AECD-2182, 1948.
- [71] S. G. Thompson, A. Ghiorso, G. T. Seaborg, *Phys. Rev.* 77 (1950) 838.
- [72] S. G. Thompson, A. Ghiorso, G. T. Seaborg, *Phys. Rev.* 80 (1950) 781.
- [73] S. G. Thompson, J. Street, A. Ghiorso, G. T. Seaborg, *Phys. Rev.* 78 (1950) 298.
- [74] S. G. Thompson, J. Street, A. Ghiorso, G. T. Seaborg, *Phys. Rev.* 78 (1950) 790.
- [75] A. Ghiorso, B. G. Harvey, G. R. Choppin, S. G. Thompson, G. T. Seaborg, *Phys. Rev.* 99 (1955) 1048.
- [76] A. Ghiorso, B. G. Harvey, G. R. Choppin, S. G. Thompson, G. T. Seaborg, *Phys. Rev.* 98 (1955) 1548.
- [77] A. Ghiorso, T. Sikkeland, J. R. Walton, G. T. Seaborg, *Phys. Rev. Lett.* 1 (1958) 18.
- [78] P. R. Fields et al., *Phys. Rev.* 107 (1957) 1460.
- [79] A. Ghiorso, T. Sikkeland, A. E. Larsh, R. M. Latimer, *Phys. Rev. Lett.* 6 (1961) 473.
- [80] G. N. Flerov et al., *Phys. Lett.* 13 (1964) 73.
- [81] A. Ghiorso, M. Nurmiä, J. A. Harris, K. A. Eskola, P. L. Eskola, *Phys. Rev. Lett.* 22 (1969) 1317.
- [82] A. Ghiorso, M. Nurmiä, K. A. Eskola, J. A. Harris, P. L. Eskola, *Phys. Rev. Lett.* 24 (1970) 1498.
- [83] G. N. Flerov, Y. T. Oganessian, Y. V. Lobanov, , Y. A. Lazarev, S. P. Tretyakova, I. V. Kolesov, V. M. Plotko, *Atomnaya Energiya* 29 (1970) 243.
- [84] V. A. Drulin, A. G. Demin, Y. P. Kharitonov, G. N. Akap'ev, V. I. Rud, G. Y. Sung-Chin-Yang, L. P. Chelnokov, K. A. Gavrilov, *Yad. Fiz.* 13 (1971) 251.
- [85] A. Ghiorso, J. M. Nitschke, J. R. Alonso, C. T. Alonso, M. Nurmiä, G. T. Seaborg, E. K. Hulet, R. W. Longhead, *Phys. Rev. Lett.* 33 (1974) 1490.

- [86] Y. T. Oganessian, Y. P. Tretyakov, A. S. Il'inov, A. G. Demin, A. A. Pleve, S. P. Tretyakova, V. M. Plofko, M. P. Ivanov, N. A. Danilov, Y. S. Korotkin, G. N. Flerov, *Pism. Zh. Eksp. Teor. Fiz.* 20 (1974) 580.
- [87] G. Münzenberg, S. Hofmann, F. P. Heßberger, W. Reisdorf, K. H. Schmidt, J. H. R. Schneider, P. Armbruster, C. C. Sahm, B. Thuma, *Z. Phys.* A300 (1981) 107.
- [88] Y. T. Oganessian, A. G. Demin, N. A. Danilov, G. N. Flerov, M. P. Ivanov, A. S. Iljinov, N. N. Kolesnikov, B. N. Markov, V. M. Plotko, S. P. Tretyakova, *Nucl. Phys.* A273 (1976) 505.
- [89] G. Münzenberg, P. Armbruster, H. Folger, F. P. Heßberger, S. Hofmann, J. Keller, K. Poppensieker, W. Reisdorf, K. H. Schmidt, H. J. Schott, M. Leino, R. Hingman, *Z. Phys.* 317 (1984) 235.
- [90] Y. T. Oganessian, A. G. Demin, M. Husonnois, S. P. Tretyakova, Y. P. Kharitonov, V. K. Utyonkov, I. V. Shirokovsky, O. Constantinescu, H. Bruchertseifer, Y. S. Korotkin, *Z. Phys.* A319 (1984) 215.
- [91] G. Münzenberg, W. Reisdorf, S. Hofmann, Y. K. Agarwal, F. P. Heßberger, K. Poppensieker, J. R. H. Schneider, W. F. W. Schneider, K. H. Schmidt, H. J. Schott, P. Armbruster, C. C. Sahm, D. Vermeulen, *Z. Phys.* 315 (1984) 145.
- [92] S. Hofmann, V. Ninov, F. P. Heßberger, P. Armbruster, H. Fogler, G. Münzenberg, H.-J. Schött, A. G. Popeko, A. V. Yeremin, A. N. Andreev, S. Saro, R. Janik, M. E. Leino, *Z. Phys.* A350 (1995) 277.
- [93] K. Morita, K. Morimoto, D. Kaji, H. Haba, E. Ideguchi, J. Peter, R. Kanungo, K. Katori, H. Koura, H. Kudo, T. Ohnishi, T. S. A. Ozawa, K. Sueki, I. Tanihata, H. Xu, A. V. Yeremin, A. Yoneda, A. Yoshida, Y. L. Zhao, T. Zheng, S. Goto, F. Tokanai, *Jour. Phys. Soc. of Japan* 73 (2004) 1738.
- [94] Y. Oganessian et al., *Nature* 400 (1999) 242.

A. Appendix

A. Appendix

Table A.1.: Table presents discoveries, starting from 1940, in the artificial SHE elements production from $Z=93$ to $Z=118$. Continued in table A.2.

Z	S.	Discoverer	Laboratory	Date	Reaction	ref.	Comment
93	<i>Np</i>	M. McMillan et al.	Berkeley, USA	1940	$^{238}\text{U}(\text{n},\beta)^{239}\text{Np}$	[1]	
94	<i>Pu</i>	G. Seaborg et al.	Berkeley, USA	1941	$^{238}\text{U}+^2\text{H}\rightarrow^{238}\text{Np}+$ $2\text{n}\rightarrow^{238}\text{Pu}$	[2]	
95	<i>Am</i>	G. Seaborg et al.	Chicago, USA	1944	$^{239}\text{Pu}+2\text{n}\rightarrow$ $^{241}\text{Pu}\rightarrow^{241}\text{Am}$	[69]	
96	<i>Cm</i>	G. Seaborg et al.	Berkeley, USA	1944	$^{239}\text{Pu}+^4\text{He}\rightarrow$ $^{242}\text{Cm}+\text{n}$	[70]	
97	<i>Bk</i>	S. Thompson et al.	Berkeley, USA	1949	$^{241}\text{Am}+^4\text{He}\rightarrow$ $^{243}\text{Bk}+2\text{n}$	[71, 72]	
98	<i>Cf</i>	S. Thompson et al.	Berkeley, USA	1950	$^{242}\text{Cm}+^4\text{He}\rightarrow$ $^{245}\text{Cf}+1\text{n}$	[73, 74]	
99	<i>Es</i>	A. Ghiorso et al.	Argonne, Los Alamos, Berkeley, USA	1952	many neutron capture by ^{238}U and beta decay	[75]	debris of the "Mike" hydrogen bomb test.
100	<i>Fm</i>	-/-	-/-	1952	-/-	[75]	-/-
101	<i>Md</i>	A. Ghiorso et al.	Berkeley, USA	1955	$^{253}\text{Es}+^4\text{He}\rightarrow$ $^{246}\text{Md}+1\text{n}$	[76]	identification one-atom-at-a-time basis.
102	<i>No</i>	A. Ghiorso et al.	Berkeley, USA	1958	$^{246}\text{Cm}+^{12}\text{C}\rightarrow$ $^{254}\text{No}+4\text{n}$	[77]	more complete identification than Dubna
102	<i>No</i>	P. Fields et al.	Nobel Inst., Sweden	1957	$^{246}\text{Cm}+^{13}\text{C}\rightarrow$ $^{255}\text{No}+4\text{n}$	[78]	
103	<i>Lr</i>	A. Ghiorso et al.	Berkeley, USA	1961	$^{249,250,251,252}\text{Cf}+$ $^{10,11}\text{B}\rightarrow$ $^{258}\text{Lr}+\text{xn}$	[79]	
104	<i>Rf</i>	G. Flerov et al.	JINR, Soviet Union	1964	$^{242}\text{Pu}+^{22}\text{Ne}\rightarrow$ $^{260}\text{Rf}+4\text{n}$	[80]	
104	<i>Rf</i>	A. Ghiorso et al.	Berkeley, USA	1969	$^{249}\text{Cf}+^{12,13}\text{C}\rightarrow$ $^{257,259}\text{Rf}+4,3\text{n}$	[81]	more complete identification
105	<i>Db</i>	A. Ghiorso et al.	Berkeley, USA	1970	$^{249}\text{Cf}+^{15}\text{N}\rightarrow$ $^{260}\text{Db}+4\text{n}$	[82]	shared with Dubna
105	<i>Db</i>	G. Flerov et al.	JINR, Soviet Union	1967	$^{243}\text{Am}+^{22}\text{Ne}\rightarrow$ $^{260,261}\text{Db}+4,3\text{n}$	[83, 84]	shared with Berkeley

Table A.2.: Continuation of table A.1.

Z	S.	Discoverer	Laboratory	Date	Reaction	ref.	Comment
106	<i>Sg</i>	A. Ghiorso et al.	Berkeley, USA	1974	$^{249}\text{Cf}+^{18}\text{O}\rightarrow$ $^{263}\text{Sg}+4\text{n}$	[85]	priority for Berkeley
106	<i>Sg</i>	Yu. Oganessian et al.	JINR, Soviet Union	1974	$^{208}\text{Pb}+^{54}\text{Cr}\rightarrow$ $^{260}\text{Sg}+2\text{n}$	[86]	
107	<i>Bh</i>	G. Munzenberg et al.	GSI, Ger- many	1981	$^{209}\text{Bi}+^{54}\text{Cr}\rightarrow$ $^{262}\text{Bh}+\text{n}$	[87]	priority for Darmstadt
107	<i>Bh</i>	Yu. Oganessian et al.	JINR, Soviet Union	1976	$^{209}\text{Bi}+^{54}\text{Cr}\rightarrow$ $^{261}\text{Bh}+2\text{n}$	[88]	not convincing
108	<i>Hs</i>	G. Munzenberg et al.	GSI, Ger- many	1984	$^{208}\text{Pb}+^{58}\text{Fe}\rightarrow$ $^{265}\text{Hs}+\text{n}$	[89]	Gsi gets priority
108	<i>Hs</i>	Yu. Oganessian et al.	JINR, Soviet Union	1984	$^{208}\text{Pb}+^{58}\text{Fe}\rightarrow$ $^{264}\text{Hs}+2\text{n}$	[90]	
109	<i>Mt</i>	G. Munzenberg et al.	GSI, Ger- many	1982	$^{209}\text{Bi}+^{58}\text{Fe}\rightarrow$ $^{266}\text{Mt}+\text{n}$	[91]	
110	<i>Ds</i>	S. Hofmann et al.	Gsi, Ger- many	1994	$^{208}\text{Pb}+^{62}\text{Ni}\rightarrow$ $^{269}\text{Ds}+\text{n}$	[92]	
111	<i>Rg</i>	S. Hofmann et al.	Gsi, Ger- many	1994	$^{209}\text{Bi}+^{64}\text{Ni}\rightarrow$ $^{272}\text{Rg}+\text{n}$	[8]	confirmed K. Morita et al. [93]
112		S. Hofmann et al.	Gsi, Ger- many	1996	$^{208}\text{Pb}+^{70}\text{Zn}\rightarrow$ $^{277}\text{112}+\text{n}$	[9]	
113		Yu. Oganessian et al.	JINR, Rus- sia	2004	$^{243}\text{Am}+^{48}\text{Ca}\rightarrow$ $^{288}\text{115}+3\text{n},$ $^{288}\text{115}(\alpha)^{284}\text{113}$	[59]	
114		Yu. Oganessian et al.	JINR, Rus- sia	1998	$^{244}\text{Pu}+^{48}\text{Ca}\rightarrow$ $^{289}\text{114}+3\text{n}$	[94]	
115		Yu. Oganessian et al.	JINR, Rus- sia	2004	$^{243}\text{Am}+^{48}\text{Ca}\rightarrow$ $^{288}\text{115}+3\text{n}$	[59]	
116		Yu. Oganessian et al.	JINR, Rus- sia	2000	$^{248}\text{Cm}+^{48}\text{Ca}\rightarrow$ $^{292}\text{116}+4\text{n}$	[14]	
117			not discov- ered yet.				
118		Yu. Oganessian et al.	JINR, Rus- sia	2002	$^{249}\text{Cf}+^{48}\text{Ca}\rightarrow$ $^{294}\text{118}+3\text{n}$	[11, 12, 13]	

A. Appendix

Table A.3.: Detected residues and corresponding alpha decay chains. The α_2 from the energy range [6.50, 6.67] MeV of fig. 3.7 (upper left part) was taken to find the rest of the chain. Identified α -radioactive emitter is ^{212}Ac . Reaction $\text{Cr} + \text{Ho}$.

No.	E_{ion} (MeV)	$E_{\alpha 1}$ (MeV)	$E_{\alpha 2}$ (MeV)	$t_{ion} - t_{\alpha 1}$ (s)	$t_{\alpha 1} - t_{\alpha 2}$ (s)
1	16.03	7.38	6.52	1.7573	83.1806
2	8.85	7.32	6.55	1.7015	4.6917
3	17.34	7.30	6.57	1.1796	70.2909
4	16.59	7.36	6.57	0.3049	190.440
5	17.95	7.35	6.56	.5405	91.2881
6	10.23	7.26	6.56	4.1223	44.2426
7	13.85	7.33	6.56	2.233.4	65.6706
8	23.06	7.31	6.57	1.720	13.1648
9	23.24	7.20	6.58	1.1833	3.0274
10	17.14	7.34	6.59	1.0476	25.1718
11	20.16	7.26	6.59	0.0339	133.735
12	16.43	7.25	6.60	0.8509	48.6674
13	14.68	7.33	6.61	0.6775	74.9668
14	12.42	7.36	6.61	0.3059	109.532
15	16.44	7.33	6.61	3.4301	2.6304
16	12.46	7.33	6.61	.1552	11.3768
17	17.49	7.32	6.61	1.1734	71.5498
18	14.06	7.38	6.61	2.3177	124.244
...
28	11.62	7.34	6.62	.4757	33.549
29	22.37	7.40	6.62	.582	72.5978
30	15.29	7.32	6.63	.6439	184.861
31	21.92	7.32	6.63	.3308	47.2775
32	14.58	7.31	6.63	1.6887	6.5916
33	15.34	7.30	6.65	.1917	161.580
34	14.16	7.33	6.66	3.0437	5.0194
35	19.37	7.31	6.66	.6941	62.5434
36	12.96	7.35	6.66	1.9697	12.1622
37	14.51	7.34	6.66	.3188	62.098
38	9.81	7.37	6.67	.492	9.3568
39	13.28	7.33	6.67	.313	31.70

Table A.4.: Detected residues and the corresponding alpha decay chains. The α_2 from the energy range [6.68, 6.80] *MeV* of fig. 3.7 (upper left part) was taken to find the rest of the chain. Identified α -radioactive emitter is ^{211}Ac . Reaction *Cr + Ho*.

No.	E_{ion} (<i>MeV</i>)	$E_{\alpha 1}$ (<i>MeV</i>)	$E_{\alpha 2}$ (<i>MeV</i>)	$t_{ion} - t_{\alpha 1}$ (s)	$t_{\alpha 1} - t_{\alpha 2}$ (s)
1	16.51	7.47	6.68	1.3002	47.10
2	14.18	7.41	6.69	1.390	47.04
3	13.45	7.41	6.71	0.1431	15.35
4	17.41	7.32	6.71	0.0000	23.46
5	14.68	7.43	6.71	0.0291	6.52
6	15.14	7.45	6.74	1.1537	5.03
7	13.92	7.42	6.74	0.1882	0.02
8	22.33	7.43	6.77	0.4152	15.12
9	16.83	7.54	6.78	0.5713	15.44

Table A.5.: Detected residues and the corresponding alpha decay chains. The α_2 from the energy range [6.81, 6.94] *MeV* of fig. 3.7 (upper left part) was taken to find the rest of the chain. Identified α -radioactive emitter is ^{215}Th . Reaction *Cr + Ho*.

No.	E_{ion} (<i>MeV</i>)	$E_{\alpha 1}$ (<i>MeV</i>)	$E_{\alpha 2}$ (<i>MeV</i>)	$t_{ion} - t_{\alpha 1}$ (s)	$t_{\alpha 1} - t_{\alpha 2}$ (s)
1	11.91	7.43	6.81	0.9076	0.06
2	14.52	7.48	6.85	2.4493	2.79
3	12.28	7.36	6.86	1.8834	104.20
4	16.16	7.31	6.87	2.5213	50.43
5	18.46	7.45	6.87	2.6287	0.82
6	12.08	7.47	6.87	1.7759	18.78
7	13.43	7.44	6.90	1.0257	20.90
8	15.31	7.46	6.94	0.9604	13.49

Table A.6.: Detected residues and the corresponding alpha chains. The α_2 from the energy range [6.81, 6.94] *MeV* of fig. 3.7 (upper left part) was taken to find the rest of the chain. Identified α -radioactive emitter is ^{216}Th . Reaction *Cr + Ho*.

No.	E_{ion} (<i>MeV</i>)	$E_{\alpha 1}$ (<i>MeV</i>)	$E_{\alpha 2}$ (<i>MeV</i>)	$t_{ion} - t_{\alpha 1}$ (s)	$t_{\alpha 1} - t_{\alpha 2}$ (s)
1	16.21	7.86	6.83	0.0034	17.43
2	15.94	7.94	6.85	0.1458	4.29
3	17.85	7.92	6.86	0.016	48.73

A. Appendix

Table A.7.: Detected residue and its alpha decay chain. The α_2 from the energy range [7.30, 7.50] *MeV* of fig. 3.7 (upper left part) was taken to find the rest of the chain. Identified α -radioactive emitter is ^{216}Pa . Reaction *Cr + Ho*.

No.	E_{ion} (<i>MeV</i>)	$E_{\alpha 1}$ (<i>MeV</i>)	$E_{\alpha 2}$ (<i>MeV</i>)	$t_{ion} - t_{\alpha 1}$ (s)	$t_{\alpha 1} - t_{\alpha 2}$ (s)
1	17.27	7.81	7.37	0.2283	0.35

Table A.8.: Detected residues and corresponding alpha decay chains. The α_2 from the energy range [7.30, 7.50] *MeV* of fig. 3.7 (upper left part) was taken to find the rest of the chain. Identified α -radioactive emitter is $^{214}\text{Pa}/^{215}\text{Pa}$. Reaction *Cr + Ho*.

No.	E_{ion} (<i>MeV</i>)	$E_{\alpha 1}$ (<i>MeV</i>)	$E_{\alpha 2}$ (<i>MeV</i>)	$t_{ion} - t_{\alpha 1}$ (s)	$t_{\alpha 1} - t_{\alpha 2}$ (s)
1	13.85	8.03	7.40	0.0002	0.26
2	14.15	8.12	7.46	0.0068	0.24

Table A.9.: To find this chain an α_2 was taken in the energy range [6.0, 6.15] *MeV* (fig. 3.7, upper right part). The chain is identified as a result of α -radioactive decay of ^{203}Rn nuclei. Reaction *Cr + Gd*.

No.	E_{ion} (<i>MeV</i>)	$E_{\alpha 1}$ (<i>MeV</i>)	$E_{\alpha 2}$ (<i>MeV</i>)	$t_{ion} - t_{\alpha 1}$ (s)	$t_{\alpha 1} - t_{\alpha 2}$ (s)
1	12.31	6.57	6.13	50.47	1374.07

Table A.10.: To find this chain an α_2 was taken in the energy range [6.20, 6.33] *MeV* (fig. 3.7, upper right part). The chain is identified as a result of α -radioactive decay of $^{205}\text{Fr}/^{206}\text{Fr}$ nuclei. Reaction *Cr + Gd*.

No.	E_{ion} (<i>MeV</i>)	$E_{\alpha 1}$ (<i>MeV</i>)	$E_{\alpha 2}$ (<i>MeV</i>)	$t_{ion} - t_{\alpha 1}$ (s)	$t_{\alpha 1} - t_{\alpha 2}$ (s)
1	10.71	6.83	6.27	3.35	65.55

Table A.11.: To find this chain an α_2 was taken in the energy range [6.35, 6.45] *MeV* (fig. 3.7, upper right part). The chain is identified as a result of α -radioactive decay of $^{208}\text{Ra}/^{204}\text{Fr}$ nuclei. Reaction *Cr + Gd*.

No.	E_{ion} (<i>MeV</i>)	$E_{\alpha 1}$ (<i>MeV</i>)	$E_{\alpha 2}$ (<i>MeV</i>)	$t_{ion} - t_{\alpha 1}$ (s)	$t_{\alpha 1} - t_{\alpha 2}$ (s)
1	13.65	7.04	6.36	0.06	112.30
2	15.13	6.99	6.37	20.52	106.74
3	16.08	7.07	6.39	4.04	0.64
4	14.76	7.10	6.40	2.65	128.73
5	16.40	7.13	6.41	0.85	90.20
6	12.75	7.05	6.41	1.31	75.31
7	14.54	7.10	6.47	1.26	2.85